

E asymmetry for single pion photo-production for G14 experiment

Peng Peng

September 9, 2015

Chapter 1

Event Selection

Three channels are studied in this thesis: $\gamma n \rightarrow p\pi^-$, $\gamma p \rightarrow p\pi^+\pi^-$ and $\gamma n \rightarrow n\pi^+\pi^-$. The charged particles are detected using the CLAS drift chambers, start counters and time-of-flight counters. The drift chambers measures the particle tracking, which is used to determine the particle momentum (p) and flight path, while the start counters and time-of-flight counters give the particle TOF, which combining with flight-path gives particle velocity (β). The momentum and velocity are combined to give the particle mass: $m = p/\beta\gamma$.

The neutrons are detected by the forward electromagnetic calorimeter. The run conditions and procedures for selecting events for the three channels are described in the following sections.

1.1 Run Conditions

According to different targets and photon beam conditions, the G14 data is divided into different run periods. Table 1.1 shows the run periods for circularly polarized photon beam, table 1.2 shows the run periods for linearly polarized photon beam.

1.2 CLAS Banks

The reconstructed particle information is stored in the CLAS banks [28]. For some history reasons, there are two systems of banks: the "PID" banks and "SEB" banks. These two systems use different algorithms to reconstruct events. The "PID" banks include HEAD, TGBI, GPID, TBID, ECHB, SCRC, STRE, TAGR, MVRT, VERT, TBER, EPIC. The "SEB" banks include HEVT, EVNT, DCPB, TRPB, ECPB, SCPB, STPB, TGPB. The banks used in this study are the "PID" banks. GPID is the main bank used in G14 analysis, it contains all the information for the charged particles, and the information for the tagger photons. The GPID bank is a combination of the PART and TBID banks. MVRT gives the vertex information for an event. The ECHB bank contains the information from the forward electromagnetic calorimeter, and gives the information for neutral particles. The HEAD bank contains the helicity information of the polarized beam. The TAGR bank stores the tagger information, which gives the energy, time, T counter ID, and E counter ID for the tagged photons. The TBER bank gives the

Period	Beam Energy	Beam Pol.	Events	Torus Curr.	Target	Target Pol.
Silver1	2280.96 MeV	$-81.7 \pm 1.4\%$	830 M	+1920 A	21a	+D(26.12%) +H(14.99%)
Silver2a	2280.96 MeV	$-81.7 \pm 1.4\%$	300 M	+1920 A	21a	+D(23.70%) -H(15.28%)
Silver2b	2280.96 MeV	$-76.2 \pm 1.4\%$	870 M	+1920 A	21a	+D(23.7%) -H(15.28%)
Silver3	2280.96 MeV	$-76.2 \pm 1.4\%$	250 M	-1500 A	21a	+D(22.00%) -H(0.3%)
Silver4	2280.96 MeV	$-76.2 \pm 1.4\%$	820 M	-1500 A	21a	-D(17.52.00%) -H(0.3%)
Silver5	2257.75 MeV	$88.8 \pm 1.5\%$	5210 M	-1500 A	21a	-D(15.79%) -H(0.8%)
Gold2a	2541.31 MeV	$88.2 \pm 1.4\%$	440 M	-1500 A	19b	+D(27.33%) +H(27.42%)
Gold2b	2541.31 MeV	$-83.4 \pm 1.5\%$	1660 M	-1500 A	19b	+D(27.33%) +H(27.42%)

Table 1.1: Run periods for runs with circularly polarized photon beam. The first column is the name of the period, silver runs use "21a" target, gold runs use "19b" target. The second column is the energy of the electron beam. The third column is the electron beam polarization. The fourth column is the number of events. The fifth column is the Torus Current, which determines the direction of the torus magnetic field. The sixth column is the target used. The seventh column is the degree of polarization for the HD target, where " \pm " indicate the direction of deuterons polarization along "z" direction in lab coordinate.

Period	Coherent Edge	Perp Events	Para Events	Amo. Events	Target	Target Pol.
Last tgt3	1800 MeV	506.6 M	483.0 M	86.0 M	22b	+D(24.51%), +H(23.02%)
Last tgt4	1800 MeV	307.6 M	304.2 M	52.4 M	22b	-D(16.77%), +H(18.09%)
Last tgt2a Last tgt2b	2000 MeV	461.3 M	464.9 M	106.7 M	22b	+D(26.29%), +H(25.96%) +D(24.51%), +H(23.02%)
Last tgt5	2000 MeV	184.7 M	208.8 M	40.8 M	22b	-D(16.77%), +H(18.09%)
gold1	2200 MeV	220.5 M	181.1 M	109.3 M	19b	+D(26.49%), +H(27.77%)
gold4	2200 MeV	20 M	20 M	0 M	19b	+D(16.07%), +H(18.88%)
last tgt1	2200 MeV	110.2 M	93.6 M	54.7 M	22b	+D(26.29%), +H(25.96%)
last tgt6	2200 MeV	93.6 M	148.3 M	10.2 M	22b	-D(16.77%), +H(18.09%)

Table 1.2: Run periods for runs with linearly polarized photon beam, a 30 μm diamond is used as the radiator, the electron beam energy for all these runs is 5551.77 MeV, the Torus field setting is -1500 A. The first column is the name of the period. The second column is the coherent edge energy. The third column is the number of events with E-plane of the linearly polarized photon beam perpendicular to the lab floor. The fourth column is the number of events with E-plane of the linearly polarized photon beam parallel to the lab floor. The fifth column is the number of events for runs with an amorphous radiator. The sixth column is the target name. The seventh column is the target polarization.

covariance matrix for the CLAS detectors. SCRC bank contains information from the TOF counters.

1.3 Channel selection

The G14 experiments are designed to study several pseudo-scalar meson channels as listed in Table 1.3. To select the channel of interest, several particle ID filters, geometric cuts, and kinematic cuts are applied to the data.

Reaction	Observables
$\gamma + n \rightarrow \pi^- p$	σ_0, Σ, E, G
$\gamma + n \rightarrow \pi^+ \pi^- n$	$\sigma_0, I^c(\Sigma), I^s, I^o, P_z, P_z^o(E), P_z^s(G), P_z^c$
$\gamma + p \rightarrow \pi^+ \pi^- p$	$\sigma_0, I^c(\Sigma), I^s, I^o, P_z, P_z^o(E), P_z^s(G), P_z^c$
$\gamma + n \rightarrow K^0 \Lambda$	σ_0, Σ, E, G $O_{x'}, O_{z'}, C_{x'}, C_{z'}, P, T(-O_{y'})$ $L_{x'}, L_{z'}, T_{x'}, T_{z'}$
$\gamma + n \rightarrow K^0 \Sigma^0$	$\sigma_0, \Sigma, P, E, G$
$\gamma + n \rightarrow K^+ \Sigma^-$	σ_0, Σ, E, G

Table 1.3: Pseudoscalar meson reactions and observables measured in G14 experiment.

1.3.1 Particle ID Filters

The first filter requires the event has the right number of final state particles. In GPID bank, each event has a list for the final state particles, which contains the each particle's PID number: proton(14), neutron(no PID in GPID bank, need ECPB bank for neutron identification), π^+ (8), π^- (9), the numbers in the parenthesis are the PID number in the GPID bank. For the reaction $\gamma n \rightarrow p\pi^-$, the first filter requires the final state having one proton and one π^- .

The second filter requires the proton and π^- having the same "targid", which indicates that proton and π^- are from the event caused by the same tagged photon.

The third filter is "ngrf==1", which requires the number of photons in the same RF bucket is one, this remove the ambiguity for events that relate to several tagged photons.

The fourth filter is the " $\Delta\beta$ " filter. This filter compare the β value of the particle from two methods to remove misidentified particles. The first β value is calculated from the timing information(δt) from the start counter and the TOF counter, and the distance(δl) from the start counter to the TOF counter, $\beta_1 = \frac{v}{c} = \frac{\delta l}{c\delta t}$. The second β value comes from the momentum of the particle, which is calculated from the track information measured by the drift chamber. Using the definition for relativistic momentum $p = m_0 v / \sqrt{1 - v^2/c^2} = m_0 \beta c / \sqrt{1 - \beta^2}$, we get $\beta_2 = \frac{p}{\sqrt{p^2 + m_0^2 c^2}}$, where m_0 is the PDG mass for the particle. The definition for this filter is $\Delta\beta = \beta_1 - \beta_2$. A filter with $\text{abs}(\Delta\beta) < 0.06$ for proton and $\text{abs}(\Delta\beta) < 0.03$ for pion is used, as shown in Figure 1.1. Figure 1.2 shows the effect of this filter on the event selection.

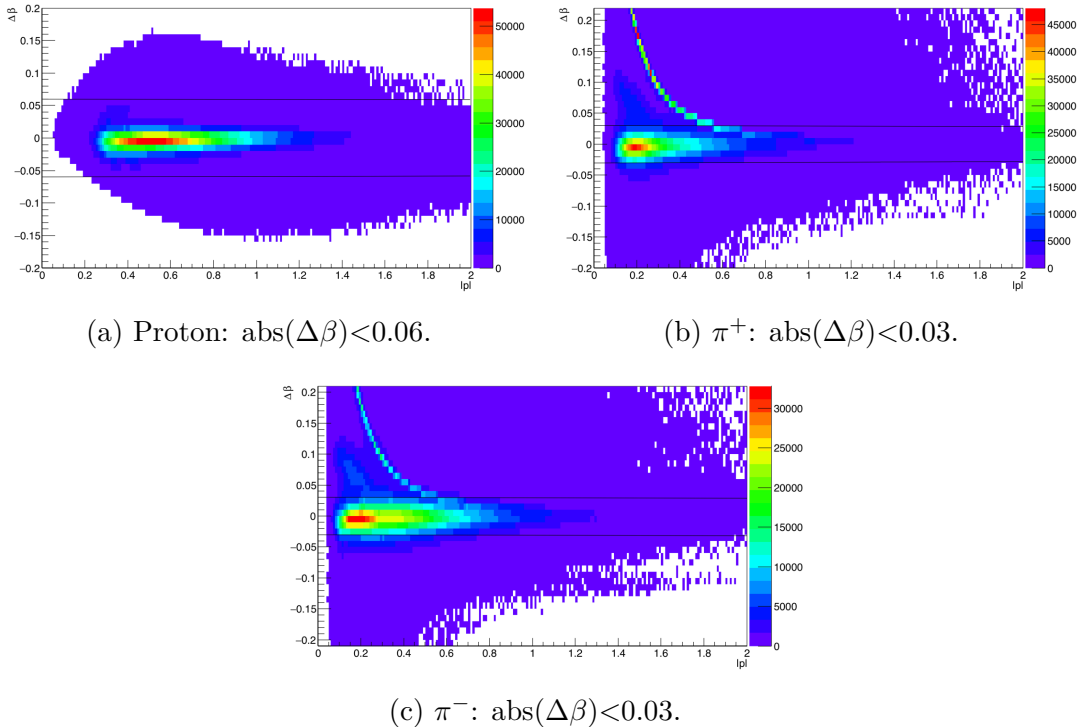


Figure 1.1: $\Delta\beta$ filter for proton, π^+ and π^- , the x-axis is $|p|$ (particle momentum).

After the four filters, the selected channel is ready for next step analysis.

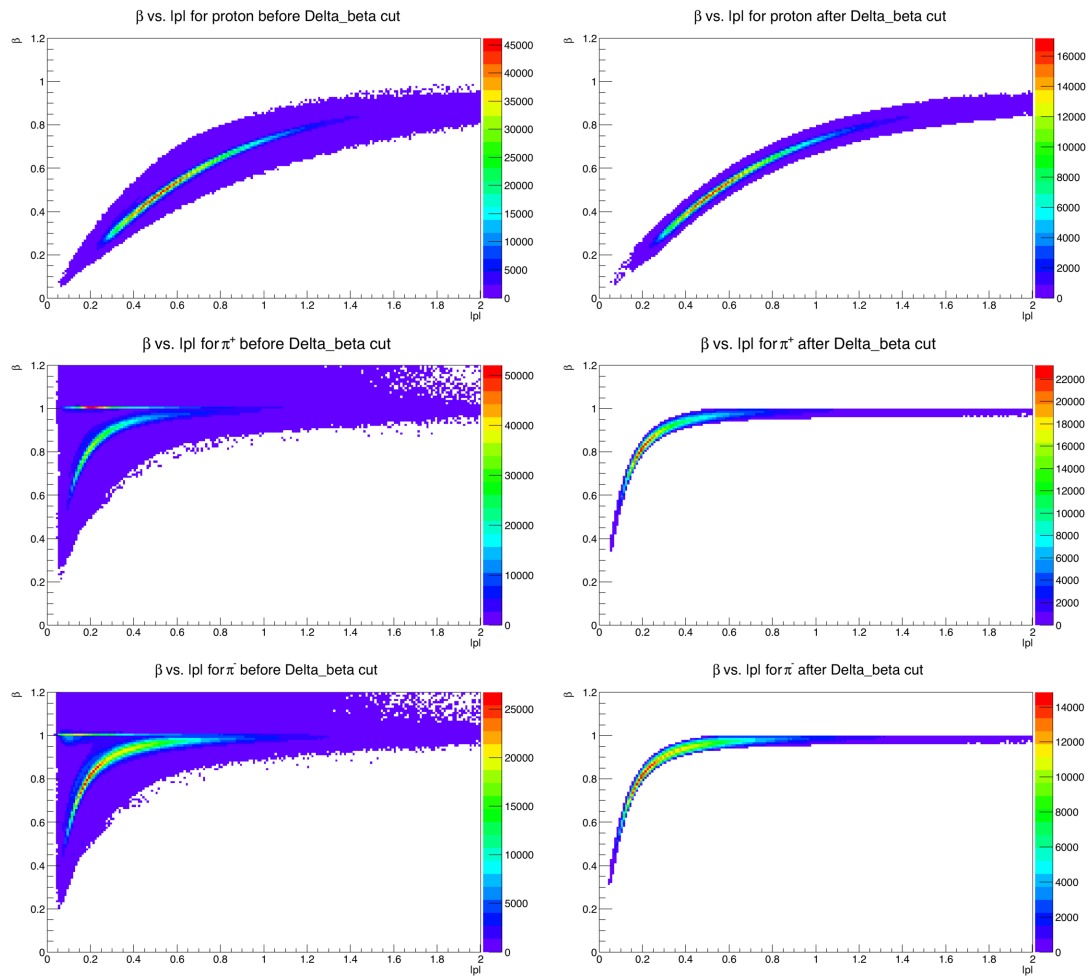


Figure 1.2: The β vs momentum plots for proton, π^+ and π^- before(left plots) and after(right plots) $\Delta\beta$ cut. Most misidentified particles are removed with this filter.

1.3.2 Geometric Cuts

There are two geometric cuts used in this study: the fiducial cut and the vertex cut. The fiducial cut takes into account the acceptance of the CLAS detectors, and the vertex cut removes events from regions, where there is no HD.

Fiducial Cut

Fiducial cut remove the angular region where there are known obstructions to the acceptance of the detectors and near the torus coils where the torus field is not well known for good track reconstruction. The fiducial cut can be defined by a relation between the polar angle θ and azimuthal angle ϕ as in Equation 1.1.

$$\theta > 4.0 + \frac{510.58}{(30 - \phi)^{1.5518}} \quad (1.1)$$

The resulting plot of θ vs. ϕ is shown in Figure 1.3.

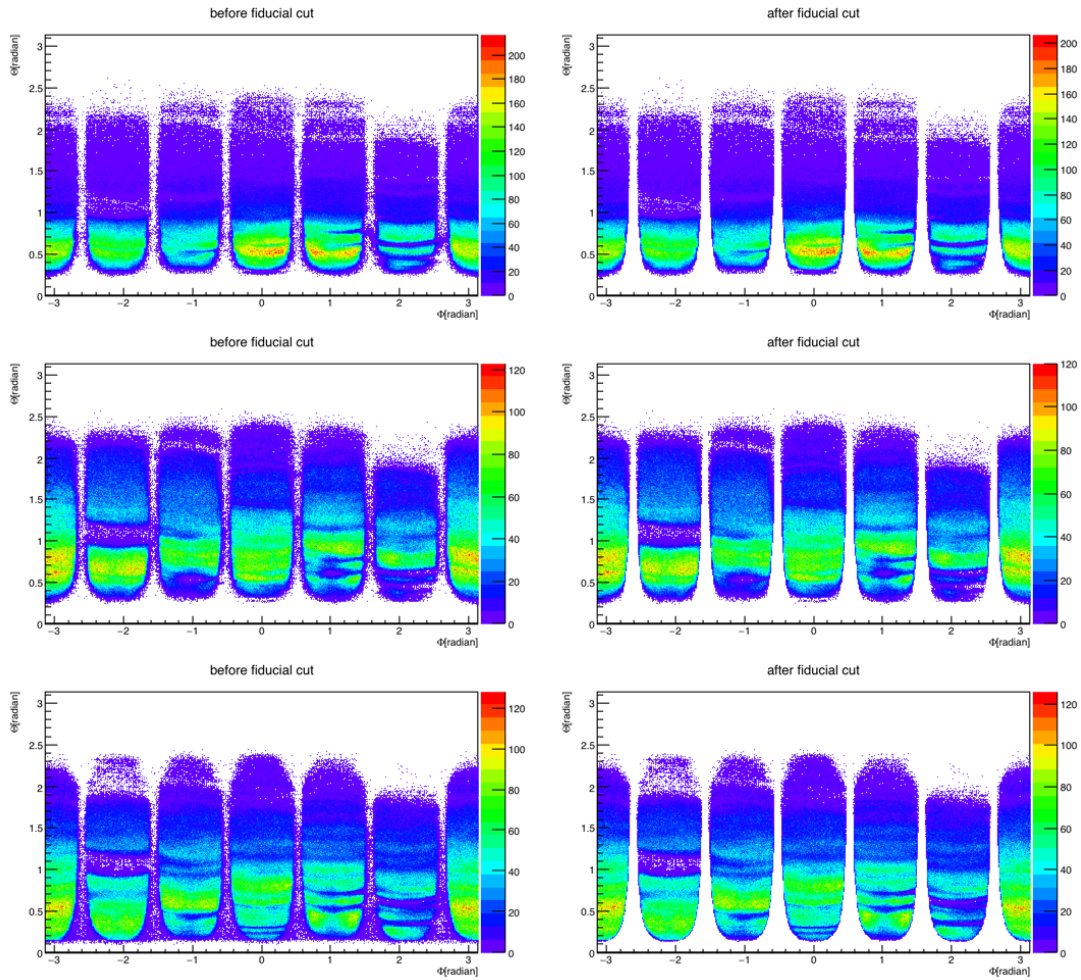


Figure 1.3: Fiducial cuts for proton, π^+ and π^- .

Vertex Cut

The HD target has a cylinder shape with the dimension 5 cm in length and 1.5 cm in diameter. The reconstruction code can determine where the event happens in the target region (the vertex information: x , y , z), this information can be used to remove the events that do not come from the HD. Two cuts are applied to the data, one is along the z direction: $-10\text{cm} < z < -5\text{ cm}$ (Figure ??), the other is along the radial direction: $r = \sqrt{x^2 + y^2} < 1\text{ cm}$ (Figure 1.5).

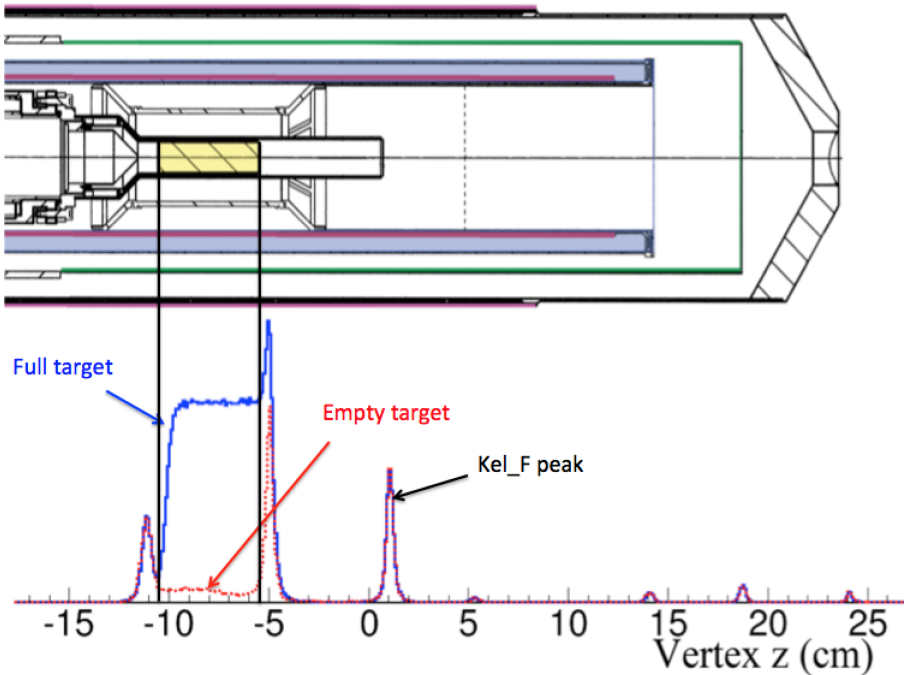


Figure 1.4: Vertex z cut: $-10.5\text{ cm} < z < -5.5\text{ cm}$. The top plot is a schematic diagram for the HD target in the IBC (In-Beam-Cryostat). The bottom plot is the vertex plot using z coordinate from the MVRT bank, the blue line is for a HD target run, the red line is for an empty cell target run, the red curve is scaled to match the downstream Kel-F peak.

1.3.3 Kinematic Cuts

Kinematic Cuts use the conservation of 4 momentum in the reaction to make cuts on the missing mass, missing momentum, and reaction angles to select the channel of interest. For example, the reaction of a photon scattering on a neutron target resulting a recoiled proton and a recoiled π^- can be written in this form: $\gamma + (n) \rightarrow p + \pi^-$. The neutron (n) is in a parenthesis, because the neutron is in the deuteron with unknown initial momentum, and we view neutron as a missing particle in this reaction. The missing mass and missing momentum for the neutron target can be calculated using the 4 momentum of the detected proton, π^- , and incoming photon energy. Three kinematic cuts are used to remove the background events: missing mass cut, missing momentum cut, and coplanarity cut (Figure 1.6). The coplanarity cut uses the fact that there is only two final

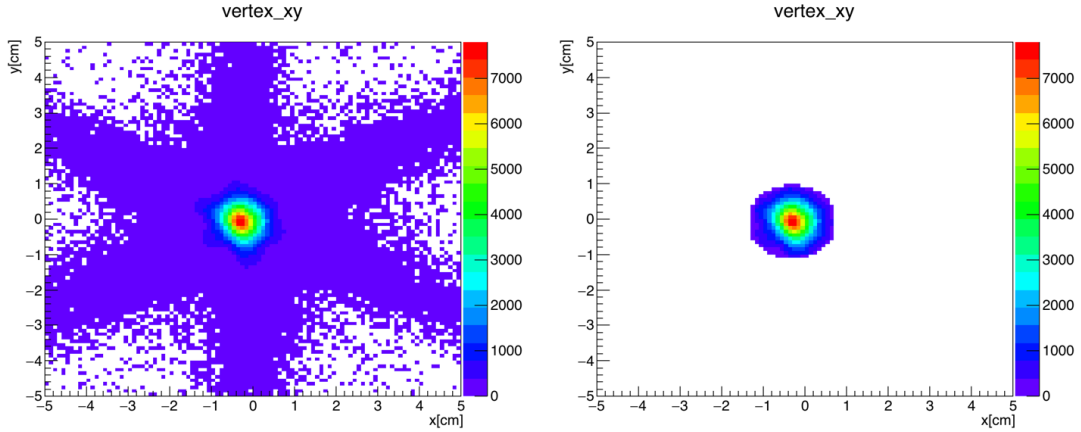


Figure 1.5: Vertex xy cut: $r < 1$ cm. The left plot is vertex xy before the cut, the six bands correspond to the gaps in CLAS detector. The right plot is vertex xy after the cut.

state particles proton and π^- , in the center of momentum frame, the difference of the ϕ angles for these two particles should be 180° .

A problem with the cuts in Figure 1.6 is that some background events under the main peak cannot be removed.

A new procedure is developed in this study to solve this problem. This method uses the kinematic fitting, and the results for the same reaction $\gamma + (n) \rightarrow p + \pi^-$ are shown in Figure 1.7. From the plots we can see that the blue curves, which represent the events passing the cut, are restricted automatically to the kinematic cuts used in Figure 1.6, and the background events are mostly removed. In the next section, this kinematic fitting procedure will be introduced in detail.

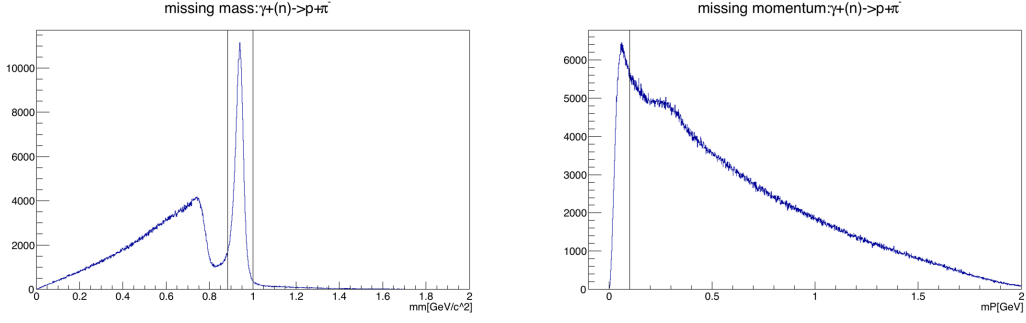
After all the filters and cuts being applied to the data, the desired channel is selected, and are ready for the study of the cross section and polarization observables for this channel.

1.4 Kinematic Fitting

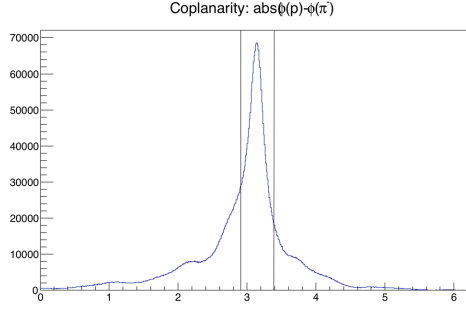
Kinematic Fitting is a technique that uses the least squares fit with physical constraints to improve measured quantities and to estimate unmeasured quantities.[29]. Take the reaction $\gamma + (n) \rightarrow p + \pi^-$ as an example, the kinematic fitting procedure can improve the measured photon tagged energy and the 4 momentum for the recoiled proton and π^- , and can estimate the 4 momentum for the bound neutron target. The constraints used in this procedure are the conservation of the 4 momentum before and after the reaction.

A iteration procedure is used to minimize $\chi^2 = (\mathbf{y} - \hat{\boldsymbol{\eta}})^T \mathbf{V}_y^{-1} (\mathbf{y} - \hat{\boldsymbol{\eta}}) + 2\lambda^T \mathbf{f}(\hat{\boldsymbol{\eta}}, \hat{\boldsymbol{\xi}})$, where y are measured quantities, η are the fitted value for the measured quantities, ξ are the unmeasured values, \mathbf{V}_y^{-1} is the covariance matrix. The minimized χ_{min}^2 follows a chi-square distribution with (K-J) degree of freedom, where K is the number of constraint functions, J is the number of unmeasured variables. Based on this chi-square distribution, the confidence level and pull distributions will be calculated to measure the goodness-of-fit and to evaluate the error estimation.

Previous studies[30, 31] have shown that the correct error estimation is crucial for



(a) Missing mass cut: 940 ± 60 MeV. (b) Missing momentum cut: < 100 MeV.



(c) Coplanarity cut: 3.1415926 ± 0.24 .

Figure 1.6: Kinematic Cuts for missing neutron in the reaction: $\gamma + (n) \rightarrow p + \pi^-$.

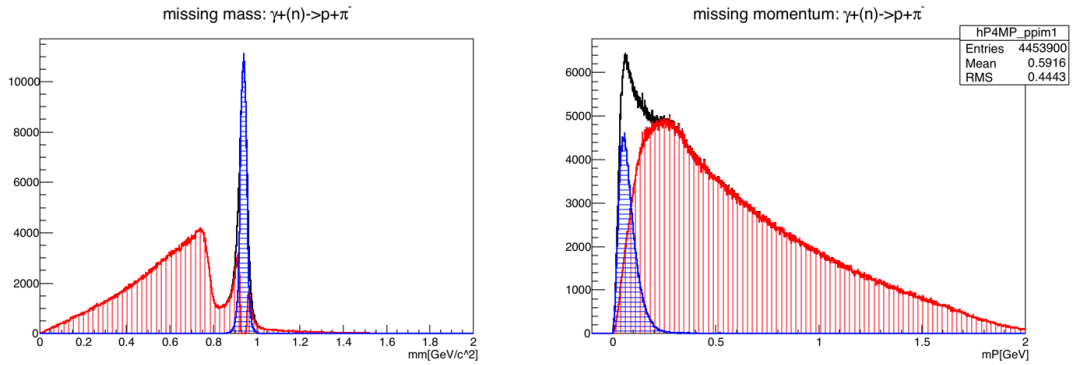
kinematic fitting. In CLAS, the covariance matrix is stored in TBER bank, in which the diagonal and off-diagonal elements give the resolution errors and correlation coefficients of the tracking parameters for each track respectively. Before the kinematic fitting, the covariance matrix need to be corrected for energy loss, multiple scattering effects and different experiment settings. The confidence level and pull distributions can also help to fine tune the covariance matrix.

The results of the kinematic fitting can be used in two ways, one is to use the confidence level to remove the background events, the other is to use the fitted values to construct the new four momentum for the particles.

1.4.1 Least Squares Fitting

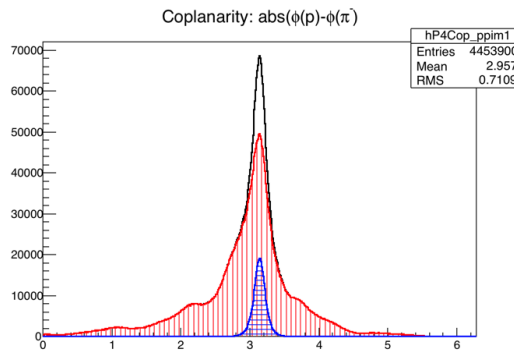
Suppose we have N independent experimental values y_1, y_2, \dots, y_N at the points x_1, x_2, \dots, x_N . The true values of y_i are unknown, but we assume there are some theoretical functions that will predicts the true value at each x_i , $f_i = f_i(\theta_1, \theta_2, \dots, \theta_L; x_i)$, where $\theta_1, \theta_2, \dots, \theta_L$ is a set of parameters, $L \leq N$.

Since each y_i has measurement error σ_i , the equations $f_i = f_i(\theta_1, \theta_2, \dots, \theta_L; x_i)$ cannot all be satisfied if $L < N$. For example, if we have three points not in a same line, a linear fitting function with only two parameters cannot go though all three points. But, we can require that the equation be satisfied "as closely as possible" if we define a statistic $X^2 = \sum_{i=1}^N ((y_i - f_i)/\sigma_i)^2$, and demand that the values of θ_i be chosen so as to minimize X^2 . Here we have assumed the measurement y_i is independent, X^2 can be written in



(a) Missing mass.

(b) Missing momentum.



(c) Coplanarity relation.

Figure 1.7: Kinematic fitting procedure for selecting the channel: $\gamma + (n) \rightarrow p + \pi^-$. In each subplot, the black line is for all the events before using kinematic fitting, the blue line is for the good events that pass the cut, and the red line is for the background events that don't pass the cut.

matrix form:

$$X^2 = (\mathbf{y} - \mathbf{f})^T \mathbf{V}_y^{-1} (\mathbf{y} - \mathbf{f}), \quad (1.2)$$

$$\text{where } \mathbf{y} = \begin{pmatrix} y_1 \\ y_2 \\ \vdots \\ \vdots \\ y_N \end{pmatrix}, \mathbf{f} = \begin{pmatrix} f_1 \\ f_2 \\ \vdots \\ \vdots \\ f_N \end{pmatrix}, \mathbf{V}_y = \begin{pmatrix} \sigma_1^2 & 0 & \cdot & \cdot & \cdot & 0 \\ 0 & \sigma_2^2 & \cdot & \cdot & \cdot & 0 \\ \cdot & \cdot & \cdot & \cdot & \cdot & \cdot \\ \cdot & \cdot & \cdot & \cdot & \cdot & \cdot \\ \cdot & \cdot & \cdot & \cdot & \cdot & \cdot \\ 0 & 0 & \cdot & \cdot & \cdot & \sigma_N^2 \end{pmatrix}.$$

The Linear Least Squares Model

If the functions f_i are linear functions of the parameters θ_i , then an exact solution for the parameters can be solved.

$$f_i = f_i(\theta_1, \theta_2, \dots, \theta_L; x_i) = \sum_{l=1}^L a_{il} \theta_l, \quad i = 1, 2, \dots, N; \quad L < N \quad (1.3)$$

$$\text{In matrix notation } \mathbf{f} = \mathbf{A}\theta, \quad \mathbf{A} = \begin{pmatrix} a_{11} & a_{12} & \cdot & \cdot & \cdot & a_{1L} \\ a_{21} & a_{22} & \cdot & \cdot & \cdot & a_{2L} \\ \cdot & \cdot & \cdot & \cdot & \cdot & \cdot \\ \cdot & \cdot & \cdot & \cdot & \cdot & \cdot \\ \cdot & \cdot & \cdot & \cdot & \cdot & \cdot \\ a_{N1} & a_{N2} & \cdot & \cdot & \cdot & a_{NL} \end{pmatrix}, \quad \theta = \begin{pmatrix} \theta_1 \\ \theta_2 \\ \cdot \\ \cdot \\ \theta_L \end{pmatrix}.$$

$$X^2 = (\mathbf{y} - \mathbf{A}\theta)^T \mathbf{V}_y^{-1} (\mathbf{y} - \mathbf{A}\theta) \quad (1.4)$$

Minimizing X^2 by taking the derivatives of X^2 with respect to θ , we have,

$$\nabla_{\theta} X^2 = -2(\mathbf{A}^T \mathbf{V}_y^{-1} \mathbf{y} - \mathbf{A}^T \mathbf{V}_y^{-1} \mathbf{A} \theta) = 0 \quad (1.5)$$

If the matrix $(\mathbf{A}^T \mathbf{V}_y^{-1} \mathbf{A})$ is non-singular and can be inverted, the solution for θ is:

$$\hat{\theta} = (\mathbf{A}^T \mathbf{V}_y^{-1} \mathbf{A})^{-1} \mathbf{A}^T \mathbf{V}_y^{-1} \mathbf{y}. \quad (1.6)$$

Substitute $\hat{\theta}$ back to Eq. (1.4), we get the minimized X_{min}^2 :

$$X_{min}^2 = (\mathbf{y} - \mathbf{A}\hat{\theta})^T \mathbf{V}_y^{-1} (\mathbf{y} - \mathbf{A}\hat{\theta}) \quad (1.7)$$

The uncertainties for θ can also be solved by using the formula for error propagation,

$$\begin{aligned} \mathbf{V}(\hat{\theta}) &= \left((\mathbf{A}^T \mathbf{V}_y^{-1} \mathbf{A})^{-1} \mathbf{A}^T \mathbf{V}_y^{-1} \right) \mathbf{y} \left((\mathbf{A}^T \mathbf{V}_y^{-1} \mathbf{A})^{-1} \mathbf{A}^T \mathbf{V}_y^{-1} \right)^T \\ &= (\mathbf{A}^T \mathbf{V}_y^{-1} \mathbf{A})^{-1} \end{aligned} \quad (1.8)$$

From some algebra calculations we have:

$$X^2 = X_{min}^2 + (\theta - \hat{\theta})^T \mathbf{A}^T \mathbf{V}_y^{-1} \mathbf{A} (\theta - \hat{\theta}) = X_{min}^2 + (\theta - \hat{\theta})^T \mathbf{V}^{-1}(\hat{\theta}) (\theta - \hat{\theta}) \quad (1.9)$$

If the N measurements y_i are normally distributed, by definition X^2 would be a chi-square distribution with N degree of freedom. Since $\hat{\theta}$ is linearly related to y_i , it is also normally distributed. All the three terms in Eq.(1.9) will be chi-square distributed, in which X^2 has N degree of freedom, X_{min}^2 has $(N-L)$ degree of freedom, $(\theta - \hat{\theta})^T \mathbf{V}^{-1}(\hat{\theta})(\theta - \hat{\theta})$ has L degree of freedom.

Eq.(1.6) and (1.8) give the solution to the linear LS problem for unknown parameters θ . This result also hold when V_y is a matrix with non-zero covariance terms, in this case, the N measurements y_i are not independent.

The Nonlinear Least Squares Model

If f_i are nonlinear functions of the parameters θ_i , there are no exact solutions for θ_i as in the linear case. We need to use iterative procedure to perform the minimization.

As discussed earlier, we want to minimize the quantity $X^2 = (\mathbf{y} - \mathbf{f})^T \mathbf{V}_y^{-1}(\mathbf{y} - \mathbf{f})$, where \mathbf{y} is the vector of measurements with covariance matrix \mathbf{V}_y , and $\mathbf{f} = \mathbf{f}(\theta; \mathbf{x})$ is the vector of predicted values, which is nonlinear function of θ . Suppose we have found of a set of approximate parameters $\theta^\nu = \{\theta_1^\nu, \theta_2^\nu, \dots, \theta_L^\nu\}$ in the ν -th iteration. To make the calculation simple, we assume independent measurements, $V_{y_{ii}} = \sigma_i^2$, the derivative of X^2 with respect to θ at $\theta = \theta^\nu$ is,

$$g_l(\theta^\nu) = g_l^\nu = \frac{\partial X^2}{\partial \theta_l} = \sum_{i=1}^N \left(-\frac{2}{\sigma_i^2} \right) (y_i - f_i^\nu) \left[\frac{\partial f_i}{\partial \theta_l} \right]_{\theta^\nu}, \quad l = 1, 2, \dots, L \quad (1.10)$$

We want to find an increment $\Delta\theta^\nu$ to θ^ν which make $g(\theta^\nu + \Delta\theta^\nu) = 0$. To find $\Delta\theta^\nu$, we expand g_l around θ^ν to first order,

$$g_l^\nu + \frac{\partial g_l^\nu}{\partial \theta_1} \Delta\theta_1^\nu + \frac{\partial g_l^\nu}{\partial \theta_2} \Delta\theta_2^\nu + \dots + \frac{\partial g_l^\nu}{\partial \theta_L} \Delta\theta_L^\nu = 0, \quad l = 1, 2, \dots, L \quad (1.11)$$

Write

$$G_{kl}^\nu = \frac{\partial g_l^\nu}{\partial \theta_k} = \frac{\partial^2 X^2}{\partial \theta_k \partial \theta_l} = \sum_{i=1}^N \left(-\frac{2}{\sigma_i^2} \right) \left[-\frac{\partial f_i}{\partial \theta_k} \frac{\partial f_i}{\partial \theta_l} + (y_i - f_i^\nu) \frac{\partial^2 f_i^2}{\partial \theta_k \partial \theta_l} \right] \quad (1.12)$$

Eq.(1.11) can be written in matrix form $\mathbf{g}^\nu + \mathbf{G}^\nu \Delta\theta^\nu = 0$,

$$\text{where } \mathbf{g}^\nu = \begin{pmatrix} g_1^\nu \\ g_2^\nu \\ \vdots \\ g_L^\nu \end{pmatrix}, \quad \Delta\theta^\nu = \begin{pmatrix} \Delta\theta_1^\nu \\ \Delta\theta_2^\nu \\ \vdots \\ \Delta\theta_L^\nu \end{pmatrix}, \quad \mathbf{G}^\nu = \begin{pmatrix} \frac{\partial g_1}{\partial \theta_1} & \frac{\partial g_1}{\partial \theta_2} & \cdots & \cdots & \frac{\partial g_1}{\partial \theta_L} \\ \frac{\partial g_2}{\partial \theta_1} & \frac{\partial g_2}{\partial \theta_2} & \cdots & \cdots & \frac{\partial g_2}{\partial \theta_L} \\ \vdots & \vdots & \ddots & \ddots & \vdots \\ \vdots & \vdots & \vdots & \vdots & \vdots \\ \frac{\partial g_L}{\partial \theta_1} & \frac{\partial g_L}{\partial \theta_2} & \cdots & \cdots & \frac{\partial g_L}{\partial \theta_L} \end{pmatrix}_{\theta=\theta^\nu}. \quad \text{Then}$$

$\Delta\theta^\nu = -(\mathbf{G}^\nu)^{-1} \mathbf{g}^\nu$. The new parameters $\theta^{\nu+1} = \theta^\nu + \Delta\theta^\nu$ are used to find $(X^2)^{\nu+1}$, if $(X^2)^{\nu+1} < (X^2)^\nu$, the new parameters are better estimation, and the procedure is repeated until the improvement between two consecutive iterations is smaller than the preset value. If it is found that one iteration gives $(X^2)^{\nu+1} > (X^2)^\nu$, one can redefine the ν -th step by taking a smaller value, such as $\Delta\theta^\nu = \frac{1}{2} \Delta\theta^\nu$ to do the procedure.

Improved Measurements

In the previous sections, the least squares method is used to find the best values for the unknown parameters θ , which are used in some theoretical functions $f(\theta; x)$ to predict the true observable η . However, in many situations, the unknowns are the observables η themselves, such as in the kinematic fitting. In this case, we will use the observations \mathbf{y} and the covariance matrix \mathbf{V}_y as the initial estimates and use the principle of least squares to find the best estimates of η which will minimize the quantity $X^2 = \epsilon^T \mathbf{V}_y^{-1} \epsilon$, where $\epsilon = \mathbf{y} - \eta$. The final estimates $\hat{\eta}$ of the true value η are called the "improved measurements".

Least Squares Model with Constraints

As before, we first consider the linear LS problem with linear constraint functions:

$$\begin{aligned} X^2 &= (\mathbf{y} - \mathbf{A}\theta)^T \mathbf{V}_y^{-1} (\mathbf{y} - \mathbf{A}\theta), \\ \mathbf{B}\theta - \mathbf{b} &= 0, \end{aligned} \quad (1.13)$$

where the L parameters θ are related through K constraint functions, \mathbf{B} is a matrix with dimension $K \times L$, \mathbf{b} is a component vector. We introduce a K-component Lagrangian multipliers λ and rewrite the problem in the unconstrained form with L+K unknowns.

$$X^2 = (\mathbf{y} - \mathbf{A}\theta)^T \mathbf{V}_y^{-1} (\mathbf{y} - \mathbf{A}\theta) + 2\lambda^T (\mathbf{B}\theta - \mathbf{b}). \quad (1.14)$$

Eq.(1.14) can be solved exactly if we equate to zero the derivatives of X^2 with respect to θ_l and λ_k [29]. In the most general situation, both the f_i and the constraint functions are nonlinear of θ , the iterative procedure using the method of Lagrangian multipliers will be used to minimize X^2 . In the following, we give an example to show how to use least squares estimation with constraints to "improve measurements" and estimate unmeasured quantities.

Suppose we have a process $\gamma + p \rightarrow p + \pi^+ + \pi^-$, where the momenta and angles of the two pions are measured, but the recoiled proton is not measured, the momentum and energy conservation give four constraint functions. For convenience, we use a vector $\eta = \{\eta_1, \eta_2, \dots, \eta_N\}$ to represent the true values for the N measured quantities $\mathbf{y} = \{y_1, y_2, \dots, y_N\}$, the vector $\xi = \{\xi_1, \xi_2, \dots, \xi_J\}$ to represent the true values for the J unmeasured quantities. The total unknowns are N+J for η and ξ , there are K constraint equations relate the unknowns:

$$f_k(\eta_1, \eta_2, \dots, \eta_N, \xi_1, \xi_2, \dots, \xi_J) = 0, \quad k = 1, 2, \dots, K. \quad (1.15)$$

The Least Squares Principle requires that the best estimates of the unknowns η and ξ are the values making the following equations true:

$$\begin{aligned} X^2 &= (\mathbf{y} - \hat{\eta})^T \mathbf{V}_y^{-1} (\mathbf{y} - \hat{\eta}) = \text{minimum}, \\ \mathbf{f}(\hat{\eta}, \hat{\xi}) &= 0, \end{aligned} \quad (1.16)$$

As before, we introduce K additional unknowns $\lambda = \{\lambda_1, \lambda_2, \dots, \lambda_K\}$, and rewrite the problem by requiring:

$$X^2 = (\mathbf{y} - \hat{\eta})^T \mathbf{V}_y^{-1} (\mathbf{y} - \hat{\eta}) + 2\lambda^T \mathbf{f}(\hat{\eta}, \hat{\xi}) = \text{minimum}, \quad (1.17)$$

Equating the derivatives of X^2 with respect to all N+J+K unknowns to zero gives N+J+K equations:

$$\begin{aligned}\nabla_{\eta}X^2 &= -2\mathbf{V}_{\mathbf{y}}^{-1}(\mathbf{y} - \eta) + 2F_{\eta}^T\lambda = 0, \\ \nabla_{\xi}X^2 &= 2F_{\xi}^T\lambda = 0, \\ \nabla_{\lambda}X^2 &= 2\mathbf{f}(\eta, \xi) = 0,\end{aligned}\tag{1.18}$$

where the matrices F_{η} (*dimension* : $K \times N$) and F_{ξ} (*dimension* : $K \times J$) are:

$$(F_{\eta})_{ki} = \frac{\partial f_k}{\partial \eta_i}, \quad (F_{\xi})_{kj} = \frac{\partial f_k}{\partial \xi_j}.\tag{1.19}$$

Since $f(\eta, \xi)$ are nonlinear functions of η, ξ , the N+J+K functions cannot solve the N+J+K unknowns exactly, the solution must be found by iteration.

Let us suppose that solution $\eta^{\nu}, \xi^{\nu}, \lambda^{\nu}$ are found in the ν -th iteration, which gives $(X^2)^{\nu}$. We want to find the next $\eta^{\nu+1}, \xi^{\nu+1}, \lambda^{\nu+1}$, which gives $(X^2)^{\nu+1}$ smaller than $(X^2)^{\nu}$. Equations in (1.18) are used to relate the values in two iteration steps. First, we make Taylor expansion of the third equation in (1.18) around η^{ν}, ξ^{ν} and neglect the second and higher orders,

$$f_k^{\nu} + \sum_{i=1}^N (F_{\eta}^{\nu})_{ki}(\eta_i^{\nu+1} - \eta_i^{\nu}) + \sum_{j=1}^J (F_{\xi}^{\nu})_{kj}(\xi_j^{\nu+1} - \xi_j^{\nu}) = 0.\tag{1.20}$$

Then we write the other two equations in (1.18) at the $(\nu + 1)$ -th iteration values:

$$\begin{aligned}\eta^{\nu+1} &= \mathbf{y} - \mathbf{V}_{\mathbf{y}}(F_{\eta}^T)^{\nu}\lambda^{\nu+1}, \\ (F_{\xi}^T)^{\nu}\lambda^{\nu+1} &= 0,\end{aligned}\tag{1.21}$$

Substitute $\eta^{\nu+1}$ in Eq.(1.21) to Eq.(1.20), and introduce $\mathbf{r} = \mathbf{f}^{\nu} + \mathbf{F}_{\eta}^{\nu}(\mathbf{y} - \eta^{\nu})$, $\mathbf{S} = \mathbf{F}_{\eta}^{\nu}\mathbf{V}_{\mathbf{y}}(\mathbf{F}_{\eta}^T)^{\nu}$, we have:

$$\begin{aligned}\mathbf{f}^{\nu} + \mathbf{F}_{\eta}^{\nu} \left[(\mathbf{y} - \mathbf{V}_{\mathbf{y}}(\mathbf{F}_{\eta}^T)^{\nu}\lambda^{\nu+1}) - \eta^{\nu} \right] + (\mathbf{F}_{\xi}^{\nu})(\xi^{\nu+1} - \xi^{\nu}) &= \mathbf{0} \\ \Rightarrow \mathbf{r} + (\mathbf{F}_{\xi}^{\nu})(\xi^{\nu+1} - \xi^{\nu}) &= \mathbf{S}\lambda^{\nu+1} \\ \Rightarrow \lambda^{\nu+1} &= \mathbf{S}^{-1} \left[\mathbf{r} + (\mathbf{F}_{\xi}^{\nu})(\xi^{\nu+1} - \xi^{\nu}) \right].\end{aligned}\tag{1.22}$$

Use $\lambda^{\nu+1}$ from Eq.(1.22) in the second equation in Eq.(1.21), we can solve $\xi^{\nu+1}, \lambda^{\nu+1}, \eta^{\nu+1}$:

$$\begin{aligned}\xi^{\nu+1} &= \xi^{\nu} - \left[(\mathbf{F}_{\xi}^T)^{\nu}\mathbf{S}^{-1}\mathbf{F}_{\xi}^{\nu} \right]^{-1} (\mathbf{F}_{\xi}^T)^{\nu}\mathbf{S}^{-1}\mathbf{r} \\ \lambda^{\nu+1} &= \mathbf{S}^{-1} \left[\mathbf{r} + (\mathbf{F}_{\xi}^{\nu})(\xi^{\nu+1} - \xi^{\nu}) \right] \\ \eta^{\nu+1} &= \mathbf{y} - \mathbf{V}_{\mathbf{y}}(F_{\eta}^T)^{\nu}\lambda^{\nu+1}.\end{aligned}\tag{1.23}$$

By keeping the Taylor expansion of $\mathbf{f}(\eta, \xi)$ to first order, we linearize the equation set, and the completely unknown $\xi^{\nu+1}$ are solved at first, next the Lagrangian multipliers $\lambda^{\nu+1}$ and lastly the improved measurements $\eta^{\nu+1}$ are solved. These new values will be used to calculate the new $(X^2)^{\nu+1}$, which will be compared with $(X^2)^{\nu}$ to decide when to stop the iteration process. The convergence of $\Delta\eta, \Delta\xi$ may also need to be checked. For the starting values, we can choose $\eta^0 = \mathbf{y}$, the measured value, and ξ^0 can be calculated from the constraint equations by inserting η^0 . The covariance matrix for η, ξ can also be calculated[29].

Confidence Level and Pull Distributions

From section 2.1, we know that the residuals X_{min}^2 , which is obtained from the minimization process, has a chi-square distribution. This distribution can be used to define a measure for the goodness-of-fit, which is,

$$P_{\chi^2} = \int_{\chi_{min}^2}^{\infty} f(\chi^2; \nu) d\chi^2 = 1 - F(\chi_{min}^2; \nu), \quad (1.24)$$

where $f(\chi^2; \nu)$ is the PDF (probability distribution function), and $F(\chi_{min}^2; \nu)$ is the CDF (cumulative distribution function) for the chi-square distribution with ν degrees of freedom. In Root, P_{χ^2} is calculated using the function `TMath::Prob(chisq,ndf)`, which denotes the probability that an observed chi-square exceeds the value "chisq". Since CDF is uniformly distributed within $[0,1]$ (see Figure 1.8), P_{χ^2} (often called p-value) is also uniformly distributed. If the minimization process gives P_{χ^2} non-uniform, this means either the hypothesis is not satisfied or the measurements are bad. An example is that P_{χ^2} is strongly peaked near zero, this indicates a contamination of the data from the background events, since background events gives bigger χ^2 , which means fatter tail in the PDF $f(\chi^2; \nu)$, and a peak in P_{χ^2} at low probabilities. By cutting the small P_{χ^2} , we can remove the background events, as shown in Figure 1.9.

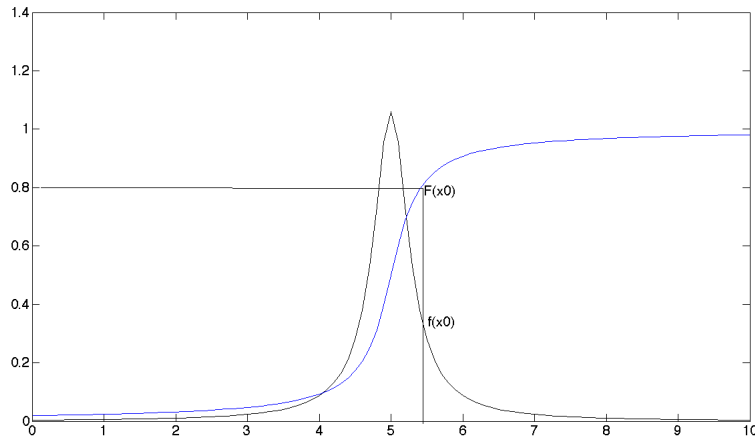
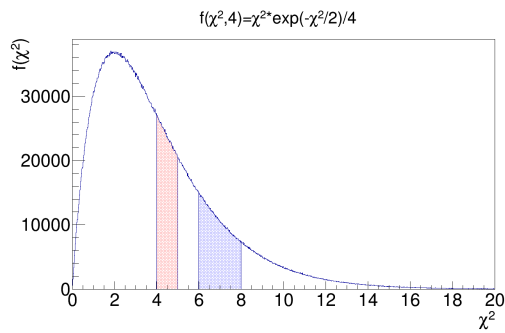


Figure 1.8: $f(x)$ is PDF, $F(x)$ is CDF for a Lorentz distribution, the probability for $x < x_0$ is $P(f(x) < F(x_0)) = P(F(x) < F(x_0)) = F(x_0)$. The distribution which has the property $P(r < r_0) = r_0$ is the uniform distribution over the region $[0,1]$.

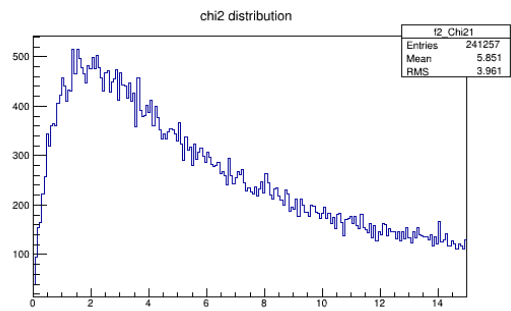
Quite often, a big χ_{min}^2 is not due to the wrong hypothesis or background events, but because either the measured values are altered by Energy loss or multi-scattering, or a wrong error estimate is used. It is helpful to define the Pull Distribution to look at each measured value,

$$z_i = \frac{\epsilon_i}{\sigma(\epsilon_i)} = \frac{y_i - \hat{\eta}_i}{\sqrt{\sigma^2(y_i) - \sigma^2(\hat{\eta}_i)}}, \quad i = 1, 2, \dots, N, \quad (1.25)$$

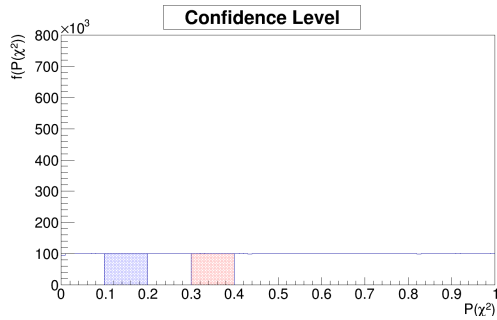
where $\epsilon_i = y_i - \hat{\eta}_i$ measure the deviations between the observations and the fitted values, ϵ_i is normalized relative to its uncertainty $\sigma(\epsilon_i)$ to allow for comparison of different



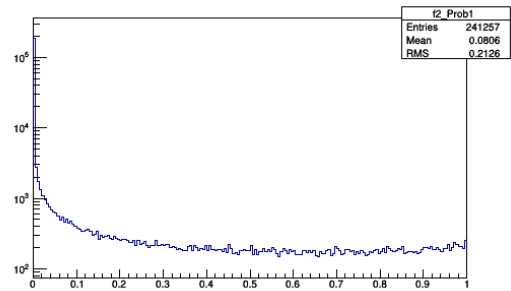
(a) monte carlo $\chi^2(4)$



(b) real data $\chi^2(4)$



(c) monte carlo cofident level



(d) real data cofident level

Figure 1.9: χ^2 distribution with degrees of freedom $n = 4$ and its confidence level from monte carlo and real data. Right two plots are those from real data, background events gives fatter tail for $f(\chi^2; \nu)$ at large χ^2 and sharp peak for P_{χ^2} around 0.

measurements. The minus sign in the calculation for $\sigma(\epsilon_i)$ comes from the fact that $y_i, \hat{\eta}_i$ are completely correlated,

$$\sigma^2(\epsilon_i) = V_{ii}(y - \hat{\eta}) = V_{ii}(y) - 2cov(y, \hat{\eta})_{ii} + V_{ii}(\hat{\eta}) = V_{ii}(y) - V_{ii}(\hat{\eta}). \quad (1.26)$$

The pull should be normally distributed about zero with $\sigma = 1$. If z_i is shifted away from zero, this indicates a systematic error in the i-th observation. If the observed z_i is too broader(narrower) than the normal distribution $N(0,1)$, the error in the i-th observation is consistently too small(large). Before the kinematic fitting, the effect of Energy loss, multi-scattering and other factors should be corrected for the observations and the covariance matrix, and the pull distribution provide a way to test how well the corrections work.

Degrees of Freedom

The function `TMATH::Prob(chisq,ndf)` for the calculation of the confidence level requires the degree of freedom for the distribution χ^2_{min} . From Eq.(1.9) in section 2.1, we know that if we have N measured values and L unknown fitted values, χ^2_{min} has (N-L) degree of freedom. If there are K constraint functions relate the L unknowns, only (L-K) of them are independent, giving (N-(L-K)) independent terms in χ^2_{min} , so χ^2_{min} is distributed as $\chi^2(N - L + K)$.

For the process $\gamma + (p) \rightarrow p + \pi^+ + \pi^-$, with recoiled proton not measured. N = 7, in which 1 is for incoming photon energy, 6 is for 2 sets of pion tracking variables. L = N+J =10, where J=3 is for the fitting values for the missing proton. K =4 from the 4 constraint equations of the conservation of energy and momentum, this is (N-L+M)=1C fit. If all the initial and final state are known, then it is a 4C fit.

1.4.2 Covariance Matrix in CLAS

From section 2.4.1, we know that an accurate covariance matrix is important for a good kinematic fitting. Instead of using the 4-vector momentum to describe the status of a particle, CLAS uses the tracking parameters $q/p, \lambda, \phi$. This section will introduce how the tracking parameters are defined, the covariance matrix for these parameters, and corrections to the covariance matrix to make it accurate.

Track Reconstruction

The track reconstruction for charged particles in the drift chambers in CLAS is done in a sector dependent system. As shown in Figure 1.10, the x_{track} -axis is along the z_{lab} direction, the y_{track} -axis goes through the center of the sector, and the z_{axis} is along the average magnetic field in the given sector. The relations between the tracking coordinates and lab coordinates are:

$$\begin{pmatrix} x_{track} \\ y_{track} \\ z_{track} \end{pmatrix} = \begin{pmatrix} z_{lab} \\ \cos(\alpha)x_{lab} + \sin(\alpha)y_{lab} \\ -\sin(\alpha)x_{lab} + \cos(\alpha)y_{lab} \end{pmatrix} \quad (1.27)$$

where $\alpha = \frac{\pi}{3}(N_{sector} - 1)$ is sector dependent.

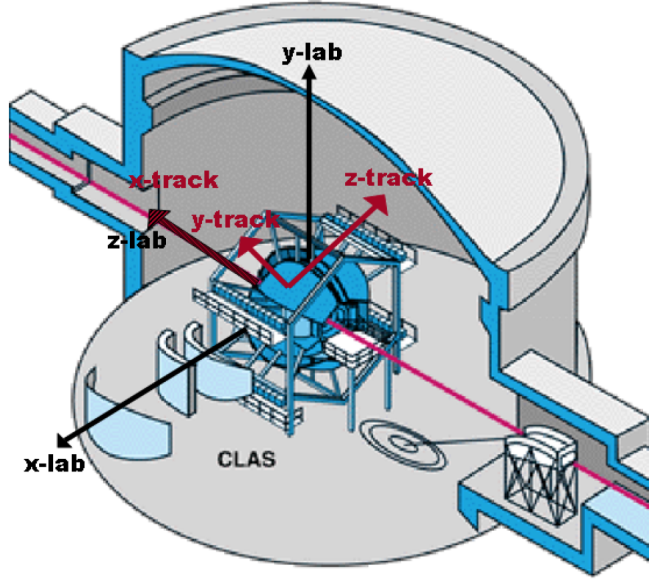


Figure 1.10: Scheme for tracking coordinates and lab coordinates

The tracking parameters for the particles in TBER bank include: $q/p, \lambda, \phi, d_0, z_0$, in which d_0 and z_0 are used in vertex reconstruction not kinematic fitting, we only discuss the first three parameters here. q is the charge of the particle, p is its momentum in the lab frame, $\lambda \in (-\pi/6, \pi/6)$ is the angle between the track and the (x_{track}, y_{track}) plane, ϕ is the angle in the (x_{track}, y_{track}) plane relative to x_{track} -axis. Using the tracking parameters, we can write the momentum of the particles in the lab frame,

$$\begin{pmatrix} p_{x_{lab}} \\ p_{y_{lab}} \\ p_{z_{lab}} \end{pmatrix} = \begin{pmatrix} p(\cos(\lambda) \sin(\phi) \cos(\alpha) - \sin(\lambda) \sin(\alpha)) \\ p(\cos(\lambda) \sin(\phi) \sin(\alpha) + \sin(\lambda) \cos(\alpha)) \\ p \cos(\lambda) \cos(\phi) \end{pmatrix}, \quad (1.28)$$

The covariance matrix for the tracking parameters are also given in the TBER bank:

$$\begin{pmatrix} cov(\frac{q}{p}, \frac{q}{p}) = c_{11} & cov(\frac{q}{p}, \lambda) = c_{12} & cov(\frac{q}{p}, \phi) = c_{13} \\ cov(\lambda, \frac{q}{p}) = c_{12} & cov(\lambda, \lambda) = c_{22} & cov(\lambda, \phi) = c_{23} \\ cov(\phi, \frac{q}{p}) = c_{13} & cov(\phi, \lambda) = c_{23} & cov(\phi, \phi) = c_{33} \end{pmatrix}. \quad (1.29)$$

These covariance matrix elements are determined from the tracking information only without any corrections. The resolution error for ϕ is approximately $\sigma_{\phi_{res}} \approx \sigma_s/R$, where $\sigma_s \approx 200\mu m$ is the resolution of detector in the plane of ϕ . $R \approx 75cm$ is the distance from the vertex to the drift chamber, so $\sigma_{\phi_{res}}$ is about 0.27 mrad. The resolution of detector in the plane of λ is one order of magnitude worse than that for ϕ , $\sigma_{\lambda_{res}}$ is about 2.7 mrad. These two errors can be calculated from the TBER bank, $\sigma_{\phi_{res}} = \sqrt{c_{33}}$ and $\sigma_{\lambda_{res}} = \sqrt{c_{22}}$. Figure 1.11 gives the errors for two tracking angle for proton, π^+ and π^- respectively. The correlation coefficients between the tracking parameters are defined as $\rho_{ij} = c_{ij}/\sqrt{c_{ii}c_{jj}}$. From Figure 1.12, we see a strong correlation between q/p and ϕ . This is because $q/p = 1/(Br \sin \theta)$, where B is the magnetic field, r is the radius of curvature of the track; on the other hand the CLAS toroidal filed B has a strong ϕ (which is the polar angle θ in lab coordinate) dependence, B is smaller for bigger ϕ as shown in Fig.5 in [10], so the two tracking parameters q/p and ϕ are strongly correlated.

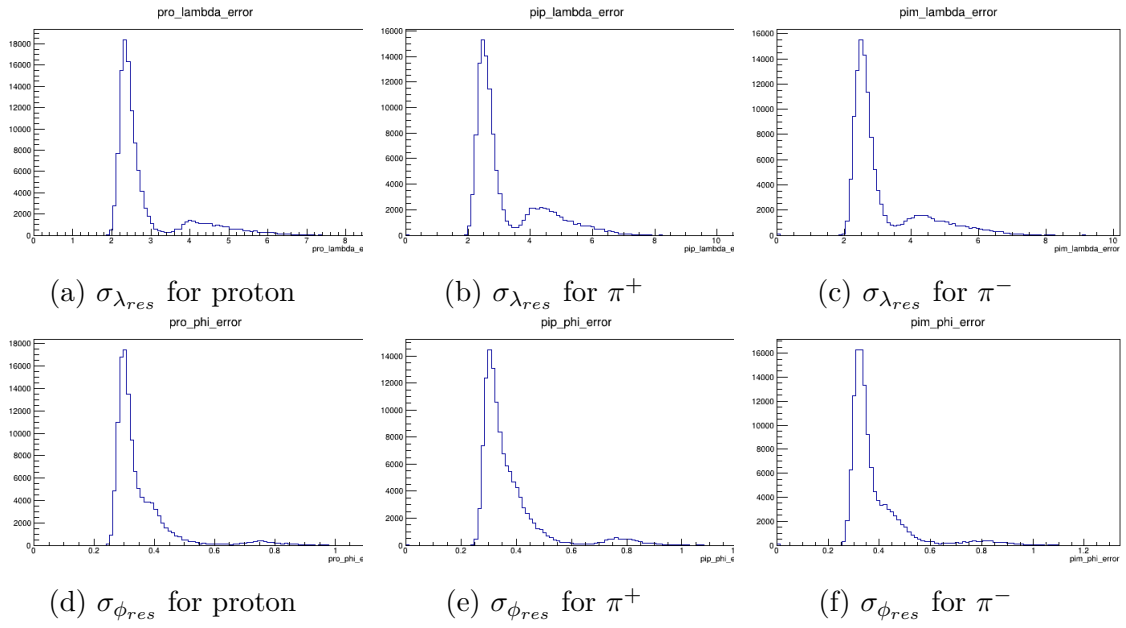


Figure 1.11: $\sigma_{\lambda_{res}}$ and $\sigma_{\phi_{res}}$ for proton, π^+ and π^-

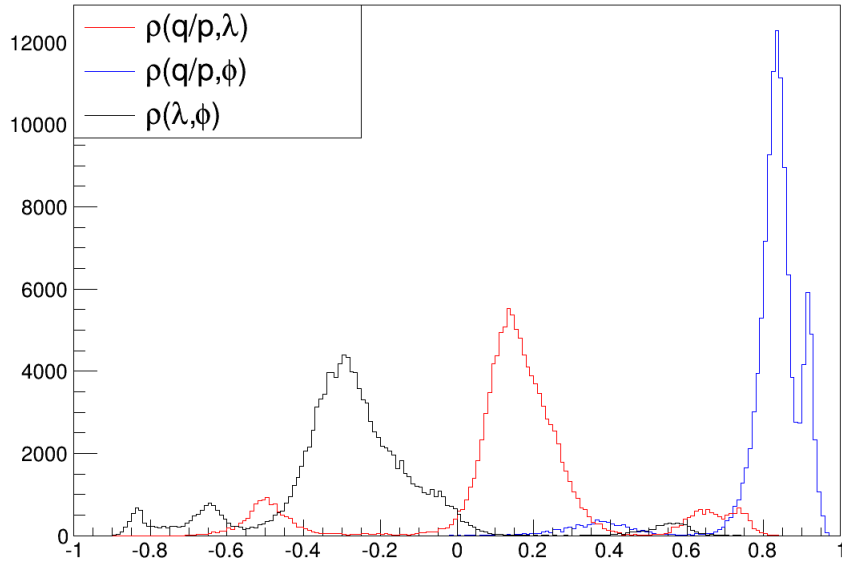


Figure 1.12: Correlation coefficients between tracking parameters. $\rho(q/p, \phi) \approx 0.85$, $\rho(q/p, \lambda) \approx 0.15$, $\rho(\lambda, \phi) \approx -0.27$.

Effect of Energy Loss and Multiple Scattering on Covariance Matrix

It's easier to study the energy loss effect using the parameter p instead of q/p , we write the new covariance matrix in terms of p as:

$$\begin{aligned} C^{pp} &= \left(\frac{\partial p}{\partial(q/p)} \right)^2 C_{\frac{q}{p}\frac{q}{p}}^{\frac{q}{p}\frac{q}{p}} = \frac{p^4}{q^2} C_{\frac{q}{p}\frac{q}{p}}^{\frac{q}{p}\frac{q}{p}}, \\ C^{p\phi} &= \left(\frac{\partial p}{\partial(q/p)} \right) \left(\frac{\partial \phi}{\partial \phi} \right) C_{\frac{q}{p}\phi}^{\frac{q}{p}\phi} = -\frac{p^2}{q} C_{\frac{q}{p}\phi}^{\frac{q}{p}\phi}, \\ C^{p\lambda} &= \left(\frac{\partial p}{\partial(q/p)} \right) \left(\frac{\partial \lambda}{\partial \lambda} \right) C_{\frac{q}{p}\lambda}^{\frac{q}{p}\lambda} = -\frac{p^2}{q} C_{\frac{q}{p}\lambda}^{\frac{q}{p}\lambda}, \end{aligned} \quad (1.30)$$

It was found in previous studies that some corrections for the covariance matrix need to be done before the energy loss and multiple scattering corrections. For the two angle parameters, the values were found to be off by a factor of 1.5:

$$\begin{aligned} \sigma_{\phi_{res}} &= 1.5\sigma_{\phi_{TBER}}, \\ \sigma_{\lambda_{res}} &= 1.5\sigma_{\lambda_{TBER}}. \end{aligned} \quad (1.31)$$

For the momentum, the TBER bank does not account for the torus current, which makes the value off by a factor of I_{max}/I :

$$\sigma_{p_{res}} = \frac{I_{max}}{I} \sigma_p = \frac{I_{max}}{I} \frac{p^2}{q} \sigma_{(q/p)_{TBER}}, \quad (1.32)$$

During the experiment, before reaching the detectors, the final state particles need to pass through some materials first, such as the target, the in-beam cryostat and the start counter. These materials will change both the value of the tracking parameters and its covariance matrix. These corrections are not included in the TBER bank, and need to be added separately.

The corrections of energy loss and multiple scattering to the tracking errors as following:

$$\begin{aligned} \sigma_p^2 &= \sigma_{p_{res}}^2 + \sigma_{el}^2, \\ \sigma_\phi^2 &= \sigma_{\phi_{res}}^2 + \sigma_{ms}^2, \\ \sigma_\lambda^2 &= \sigma_{\lambda_{res}}^2 + \sigma_{ms}^2. \end{aligned} \quad (1.33)$$

where $\sigma_{p_{res}}$, $\sigma_{\phi_{res}}$ and $\sigma_{\lambda_{res}}$ are resolution errors before the correction, σ_{el} is the energy loss correction to the momentum error, σ_{ms} is the multiple scattering correction to the tracking angle errors. The method to calculate σ_{el} and σ_{ms} can be found in section 3.1 of [31].

The Corrected Covariance Matrix

We can now write down the corrected covariance matrix for the kinematic fitting taking into account all the corrections in the previous section. Consider a reaction with L charged

particle in the final state, there are $(3L+1)$ fit parameters,

$$C_\eta = \begin{pmatrix} \sigma_{E_\gamma}^2 \\ p_1 \\ \lambda_1 \\ \phi_1 \\ \vdots \\ \vdots \\ p_L \\ \lambda_L \\ \phi_L \end{pmatrix}, \quad (1.34)$$

where E_γ is the incident photon energy and p_i, λ_i, ϕ_i are the tracking parameters for the i^{th} charged particle.

Since the measurement of different particles are uncorrelated, the covariance between different particles are zero. The covariance matrix is,

$$\eta = \begin{pmatrix} \sigma_{E_\gamma}^2 & 0 & 0 & 0 & \cdots & 0 & 0 & 0 \\ 0 & C_1^{pp} & C_1^{p\lambda} & C_1^{p\phi} & \cdots & 0 & 0 & 0 \\ 0 & C_1^{\lambda p} & C_1^{\lambda\lambda} & C_1^{\lambda\phi} & \cdots & 0 & 0 & 0 \\ 0 & C_1^{\phi p} & C_1^{\phi\lambda} & C_1^{\phi\phi} & \cdots & 0 & 0 & 0 \\ \vdots & \vdots & \vdots & \vdots & \ddots & \vdots & \vdots & \vdots \\ 0 & 0 & 0 & 0 & \cdots & C_L^{pp} & C_L^{p\lambda} & C_L^{p\phi} \\ 0 & 0 & 0 & 0 & \cdots & C_L^{\lambda p} & C_L^{\lambda\lambda} & C_L^{\lambda\phi} \\ 0 & 0 & 0 & 0 & \cdots & C_L^{\phi p} & C_L^{\phi\lambda} & C_L^{\phi\phi} \end{pmatrix}, \quad (1.35)$$

where $\sigma_{E_\gamma}^2$ is the error of measuring the tagged photon. To calculate $\sigma_{E_\gamma}^2$, let's start with the energy resolution of E-plane paddles in the tagger, which in CLAS is $0.001E_0$, E_0 is the electron beam energy. So if we detect a photon with energy \bar{E} , the energy of the photon is uniformly distributed within $[\bar{E} - 0.001E_0, \bar{E} + 0.001E_0]$ because of the resolution of the detector. The error of \bar{E} is,

$$\sigma_{E_\gamma}^2 = \int_{\bar{E}-0.001E_0}^{\bar{E}+0.001E_0} \frac{(E - \bar{E})^2}{0.002E_0} dE = \int_{-0.001E_0}^{0.001E_0} \frac{E'^2}{0.002E_0} dE' = \frac{(0.001E_0)^2}{3}. \quad (1.36)$$

$$\begin{aligned} C_i^{pp} &= \left(\frac{I_{max} p_i^2}{I q_i} \right)^2 C_{TBER}^{\frac{q_i}{p_i} \frac{q_i}{p_i}} + \sigma_{p_{loss}}^2, \\ C_i^{\lambda\lambda} &= 2.25 C_{TBER}^{\lambda_i \lambda_i} + \sigma_{ms}^2, \\ C_i^{\phi\phi} &= 2.25 C_{TBER}^{\phi_i \phi_i} + \sigma_{ms}^2, \\ C_i^{p\lambda} &= - \left(\frac{1.5 I_{max} p_i^2}{I q_i} \right) C_{TBER}^{\frac{q_i}{p_i} \lambda}, \\ C_i^{p\phi} &= - \left(\frac{1.5 I_{max} p_i^2}{I q_i} \right) C_{TBER}^{\frac{q_i}{p_i} \phi}, \\ C_i^{\lambda\phi} &= 2.25 C_{TBER}^{\lambda\phi}. \end{aligned} \quad (1.37)$$

To check if the covariance matrix has been corrected, we can look at the pull distribution of the tracking parameters, an iteration process will help determine the best estimation of the fitting parameters in the error correction.

1.4.3 Preparation for Kinematic Fitting

Before the kinematic fitting, we should do the following three corrections to get the four momentum of the particles as accurate as possible: energy loss correction, momentum correction and tagger sag correction. The kinematic fitting can be used to test how good the correction is by looking at the pull distributions.

Energy Loss Correction

As the charged particles pass through the materials in the CLAS detector, they will lose some of their energy, thus a systematic adjustment to the particles' energy is required. Eugene's Eloss package [32] is used for the corrections, this package uses first principle method to calculate the energy loss by considering all the materials that the particles go through. The difference $\Delta E = E_{after} - E_{before}$ for proton, π^+ , π^- is shown in Figure ???. As seen in the plots, the high momentum protons have small energy loss around 15 MeV, and low momentum protons, the correction is about 50 MeV, this is reasonable from the relation $dE/dx \sim 1/\beta^2$. The lighter particles π^+ , π^- lost less energy than the heavier particles proton.

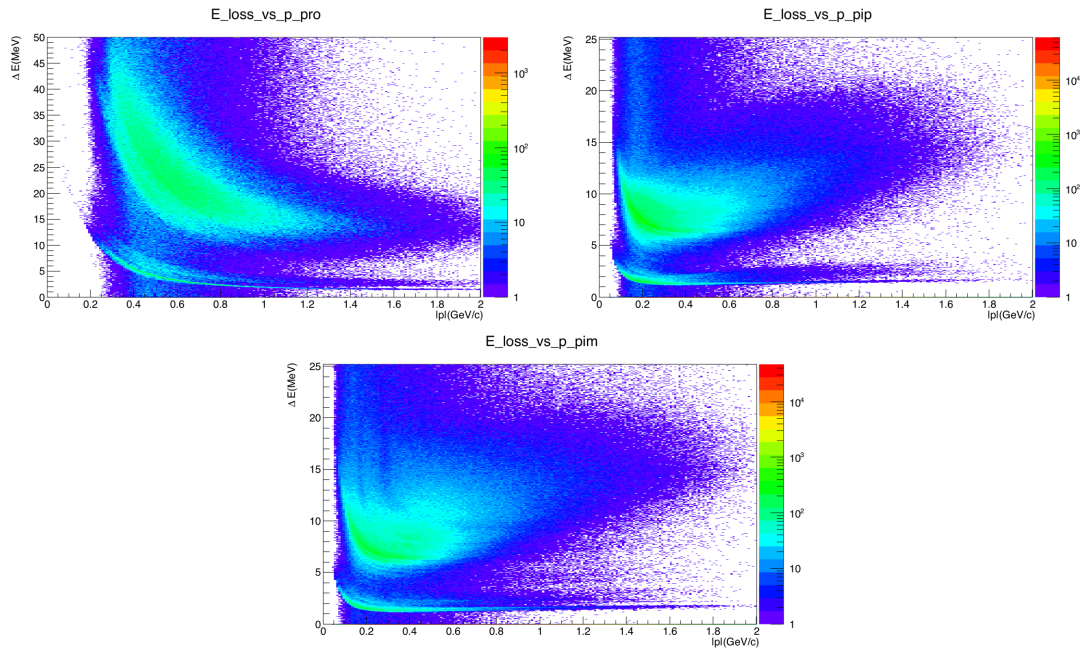


Figure 1.13: Eloss correction vs. momentum for proton (top left), π^+ (top right), π^- (bottom)

In order to check if the Eloss correction package works, we can plot the pull distributions before and after Eloss correction. Figure 1.20 gives this comparison for the pull distribution for P_{pro} (proton's momentum), We can see that after the Eloss correction,

the pull distribution becomes more like a standard normal distribution, except that the mean value is still not zero, the reason will be explained in the next section.

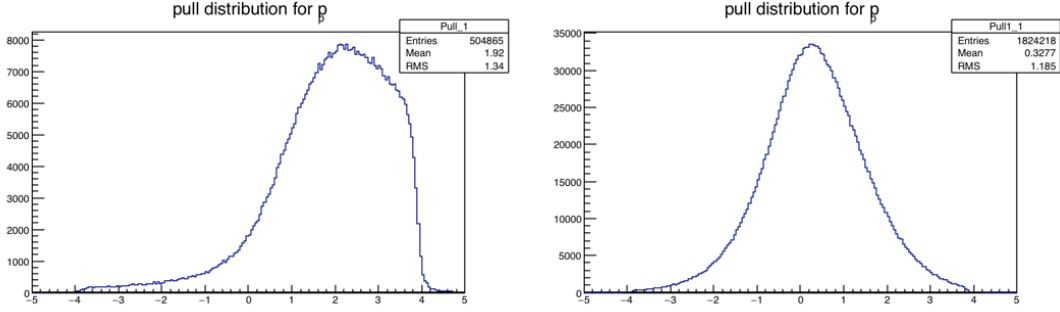


Figure 1.14: Pull distribution before(left plots) and after(right plots) Eloss correction for proton momentum.

Momentum Correction and Photon Energy Correction

After the energy loss correction, the pull distributions have improved a lot, but their means are still not close to zero. The reason for this problem can be seen in Figure 1.15. We can see that the missing mass for the missing particle depends on the ϕ angle of

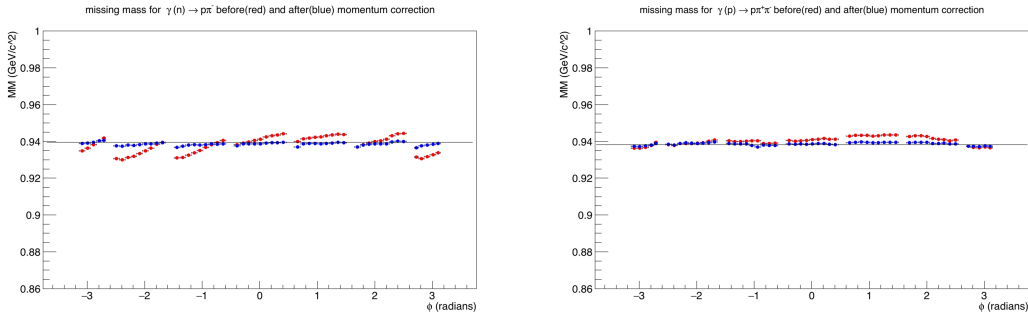


Figure 1.15: Missing Mass vs. ϕ_{pro} for the reaction $\gamma(n) \rightarrow p\pi^-$ (left plot) and $\gamma(p) \rightarrow p\pi^+\pi^-$ (right plot), the particle in the parenthesis is the missing particle. The red points are before momentum and photon energy correction, the blue points are after momentum and photon energy correction.

the recoiled proton. This is caused by the misalignment of the drift chamber with the magnetic field. Thus we need to correct the momentum of the final state particles for each θ and ϕ bin, and to correct the incoming photon energy in terms of the tagger's 767 energy bins. The way to do these two corrections is to use kinematic fitting to get the fitted value for the particles' momenta for each θ and ϕ bin and photon energy for each E-counter energy bin, then take the difference between the fitted values and the measured values to get the correction equations, $\Delta p = p^{fit} - p^{meas}$, $\Delta E_\gamma = E_\gamma^{fit} - E_\gamma^{meas}$.

Momentum correction is done for 9 (θ) \times 36 (ϕ) bins. θ and ϕ are for angles in the lab frame for recoiled protons. The nine θ bins are $0^\circ < \theta \leq 20^\circ$, $20^\circ < \theta \leq 30^\circ$, $30^\circ < \theta \leq 40^\circ$, $40^\circ < \theta \leq 50^\circ$, $50^\circ < \theta \leq 60^\circ$, $60^\circ < \theta \leq 70^\circ$, $70^\circ < \theta \leq 80^\circ$,

$80^\circ < \theta \leq 100^\circ$, $100^\circ < \theta \leq 180^\circ$. The 36 bins come from binning each of the six CLAS sectors into six bins. The schematic plots for θ and ϕ bins can be seen in Figure 1.16.

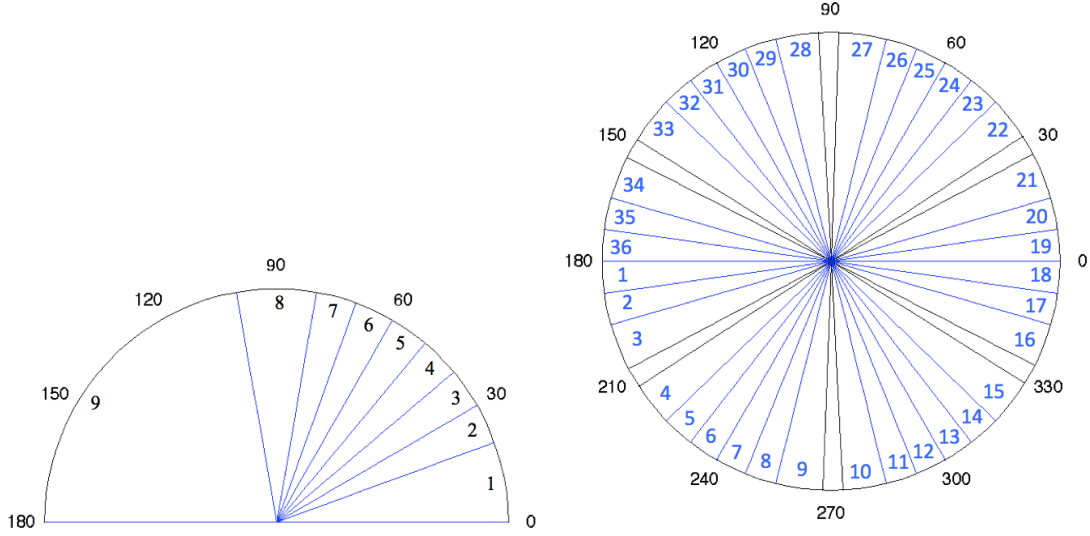


Figure 1.16: θ bins (left plot) and ϕ bins (right plot) for momentum correction. The different sizes of the θ bins are chosen by considering the CLAS acceptance is small in the forward angle and backward angle. In the plot for ϕ bins, the gaps enclosed by black lines correspond to the gaps between the six CLAS sectors. The bin size near the gap is bigger because of a smaller acceptance in this region.

Momentum correction is done for proton, π^+ , π^- respectively. The correction for the bin $20^\circ < \theta \leq 30^\circ$, $-164^\circ < \phi \leq -152^\circ$ for proton is shown in Figure 1.18. For proton and π^- , the correction combines the kinematic fitted values from both the two pion channel $\gamma(p) \rightarrow p\pi^+\pi^-$ and the one pion channel $\gamma(n) \rightarrow p\pi^-$. For π^+ , the correction only uses the two pion channel $\gamma(p) \rightarrow p\pi^+\pi^-$. The corrections for π^+ and π^- for the bin $20^\circ < \theta \leq 30^\circ$, $-164^\circ < \phi \leq -152^\circ$ are shown in Figure ??.

Photon energy correction $\Delta E_\gamma = E_\gamma^{kit} - E_\gamma^{meas}$ is calculated in terms of the 767 E-counter energy bins, and the result is also a combination of the correction from both the channel $\gamma(p) \rightarrow p\pi^+\pi^-$ and $\gamma(n) \rightarrow p\pi^-$. Figure 1.19 gives the result for the photon energy correction.

After the momentum and photon energy corrections, the same pull distribution as in Figure 1.20 is plotted again in Figure ??. From the figure, we can see that the mean of the pull distribution moves from 0.3079 to -0.01356, and the sigma moves from 1.043 to 1.007, this makes the pull distribution very close to the standard gaussian distribution.

It should be noted that since the G14 experiment uses different targets and different Torus currents. The data collected is divided to different periods as in Table 1.1. The momentum and photon energy corrections are done for 4 different run periods: Silver 1 and 2, Silver 3 and 4, Silver 5, Gold 2.

1.4.4 Kinematic Fitting for $\gamma n \rightarrow p\pi^-$

In order to select the channel of interest, the kinematic fitting is used again. The four momenta of the final state particles have been applied the energy loss correction, momentum

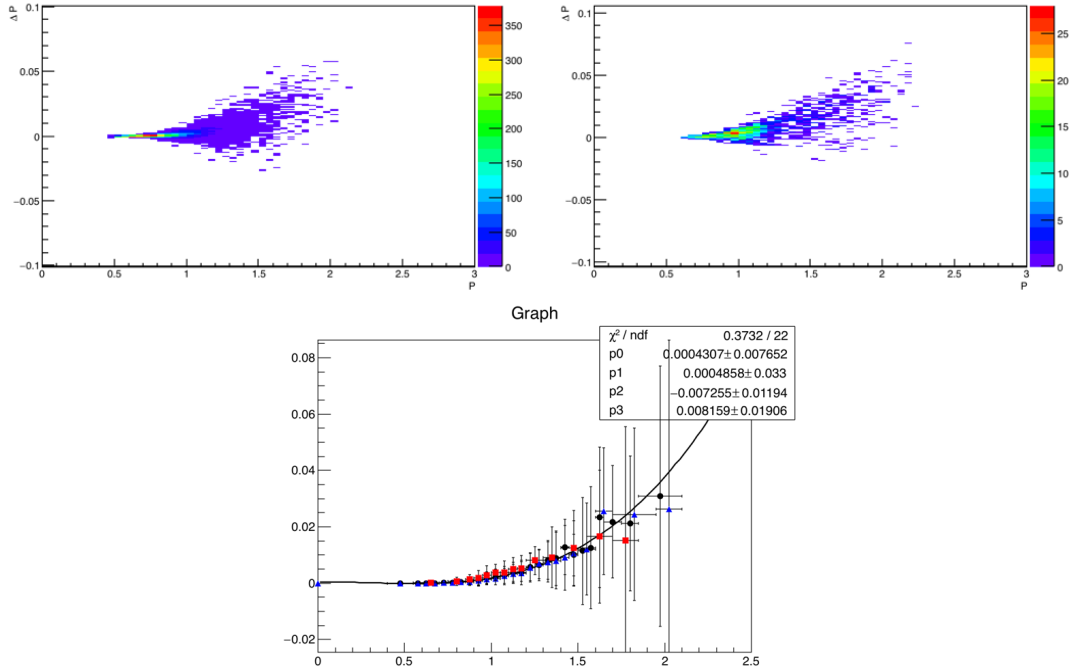


Figure 1.17: Momentum correction Δp vs p for proton for the bin $20^\circ < \theta \leq 30^\circ$, $-164^\circ < \phi \leq -152^\circ$. Top left: Δp vs p for the reaction $\gamma(p) \rightarrow p\pi^+\pi^-$. Top right: Δp vs p for the reaction $\gamma(n) \rightarrow p\pi^-$. Bottom: The Gaussian fit for Δp by binning p , blue triangle markers are for the two pion channel, red square markers are for the single pion channel, black circle markers are the combination of the two channel.

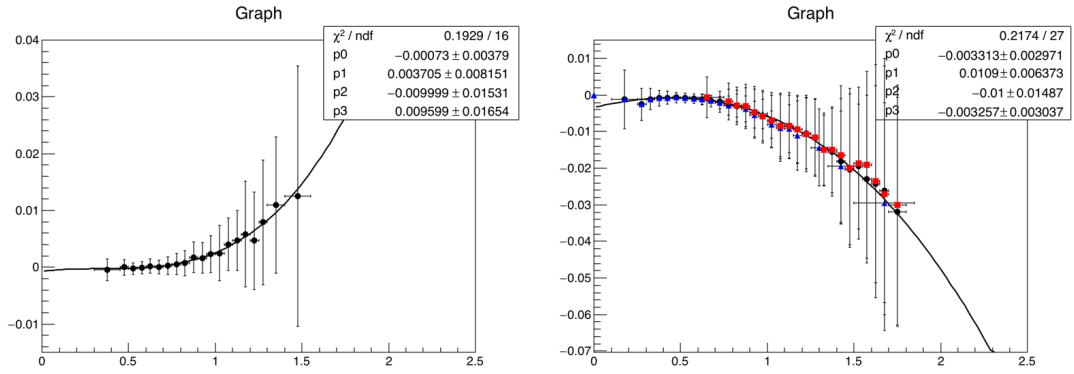


Figure 1.18: Momentum correction Δp vs p for π^+ and π^- for the bin $20^\circ < \theta \leq 30^\circ$, $-164^\circ < \phi \leq -152^\circ$. Left: correction for π^+ using the channel $\gamma(p) \rightarrow p\pi^+\pi^-$. Right: correction for π^- using both $\gamma(p) \rightarrow p\pi^+\pi^-$ and $\gamma(n) \rightarrow p\pi^-$, blue triangle markers are for the two pion channel, red square markers are for the single pion channel, black circle markers are the combination of the two channel.

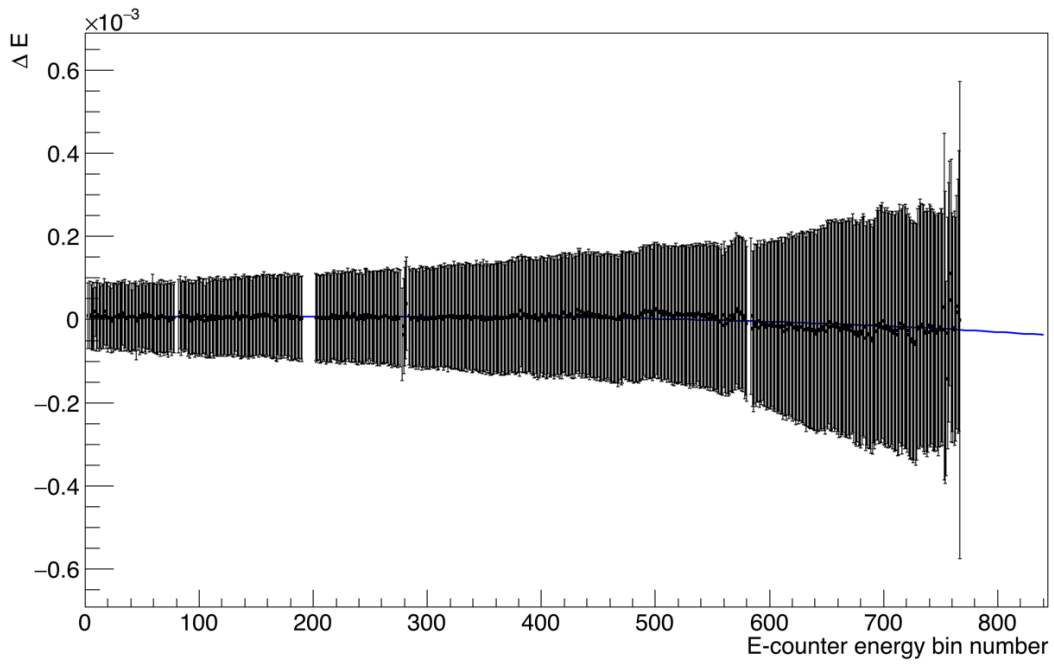


Figure 1.19: Photon energy correction $\Delta E_\gamma = E_\gamma^{kfit} - E_\gamma^{meas}$ vs. Tagger E-counter bins.

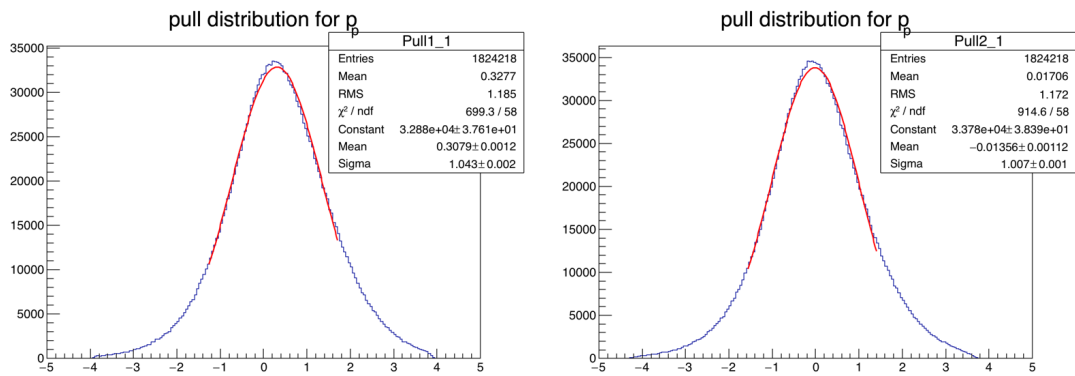


Figure 1.20: Pull distribution before(left plots) and after(right plots) Momentum and Photo Energy corrections for proton momentum. Then mean value has moved from 0.31 to -0.01

correction, and photon energy correction. For this channel, we could apply two equivalent hypotheses. One is $\gamma(n) \rightarrow p\pi^-$, which assumes an unknown moving neutron target, the other is $\gamma D \rightarrow p(p)\pi^-$, which assumes a deuteron target and a missing spectator proton in the final state. We choose the first hypothesis, since this method removes the events from the high momentum neutron in the deuteron target automatically, and the polarization observables in this study require a target with minimal initial momentum (ideally zero momentum). The confidence level cut is used to remove the background event, and the quality of the selected channel will be checked with missing mass plot, missing momentum plot, coplanarity plot, and the pull distributions for all the final state particles' tracking parameters. These results will be shown for the gold2a period at first (Figure 1.21 and Figure 1.22). Then the confidence level plots (Figure 1.23), missing mass vs. ϕ plots (Figure 1.24), and the mean and sigma values of the pull distributions (Table 1.4) will be shown for all the circularly run periods .

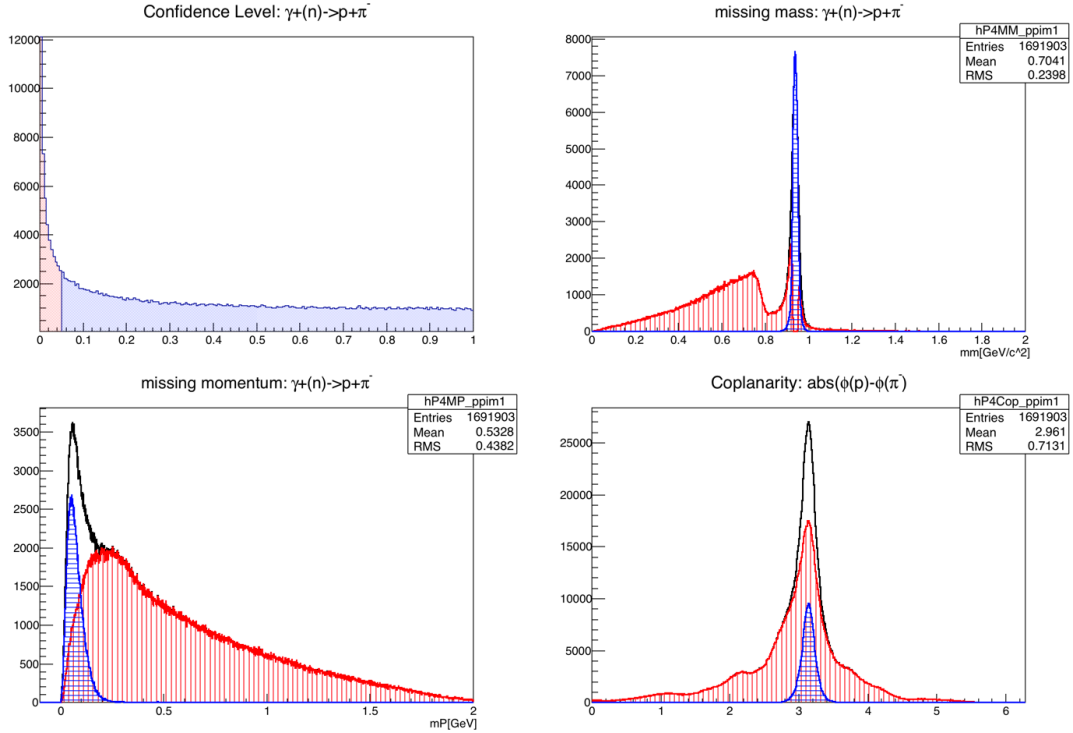


Figure 1.21: Effect of the kinematic fitting's confidence level cut on event selection for channel $\gamma(n) \rightarrow p\pi^-$ using the data from gold2a. Top left: confidence cut at 5%. top right: missing mass plot, bottom left: missing momentum, bottom right: coplanarity. For all the plots, the blue region is for good events that pass the cut, the red region is the background events that are removed by the cut.

Since the proton used in this channel is a quasi-free particle, in the kinematic fitting, an effective mass for proton is used in the procedure, and the value is estimated as following. For a free particle, the invariant mass of the particle relates to its energy and momentum as $E^2 - p^2 = m^2$. For a quasi-free particle, this relation becomes $(E - V)^2 = k^2 + m^2$, with an extra potential term V . If the potential term is much smaller than the mass of the particle, we can still view the particle as a free particle but with an off-shell effective mass m^* : $E^2 - k^2 = (m^*)^2 = m^2 + 2EV - V^2$. Since $V \ll m$, $m^* \approx m + V$. For deuteron,

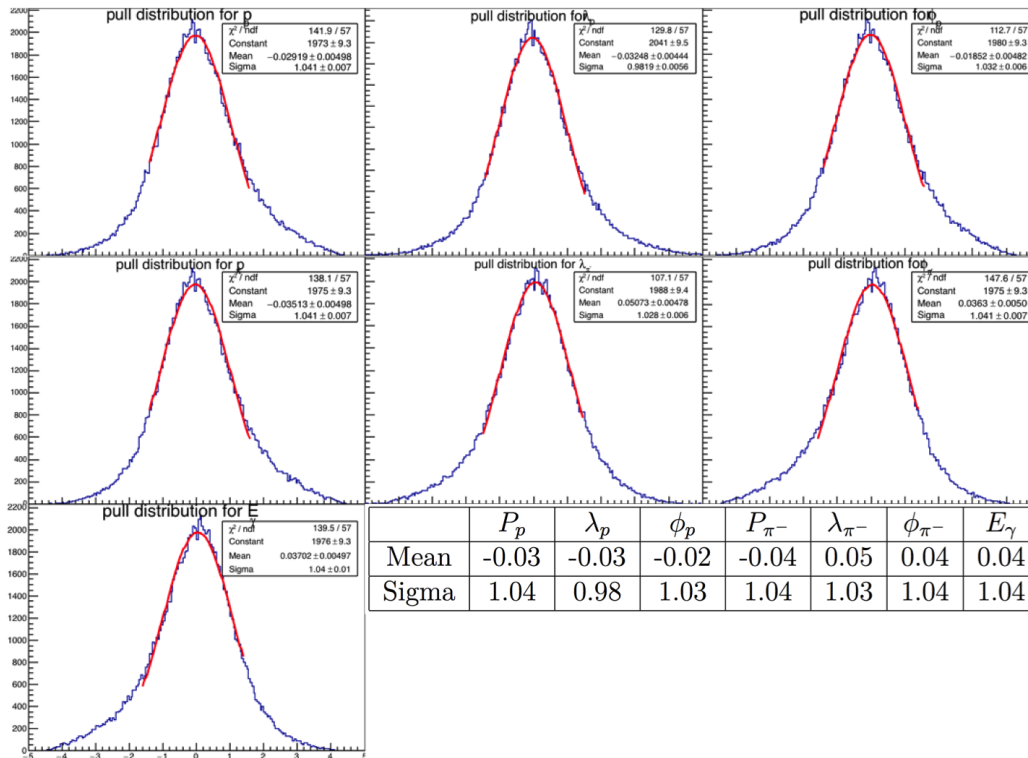


Figure 1.22: Pull distribution for gold2a for channel $\gamma(n) \rightarrow p\pi^-$. The mean and sigma values for the gaussian fit of the pull distribution are inserted at the bottom left corner, the values are very close to a standard gaussian distribution.

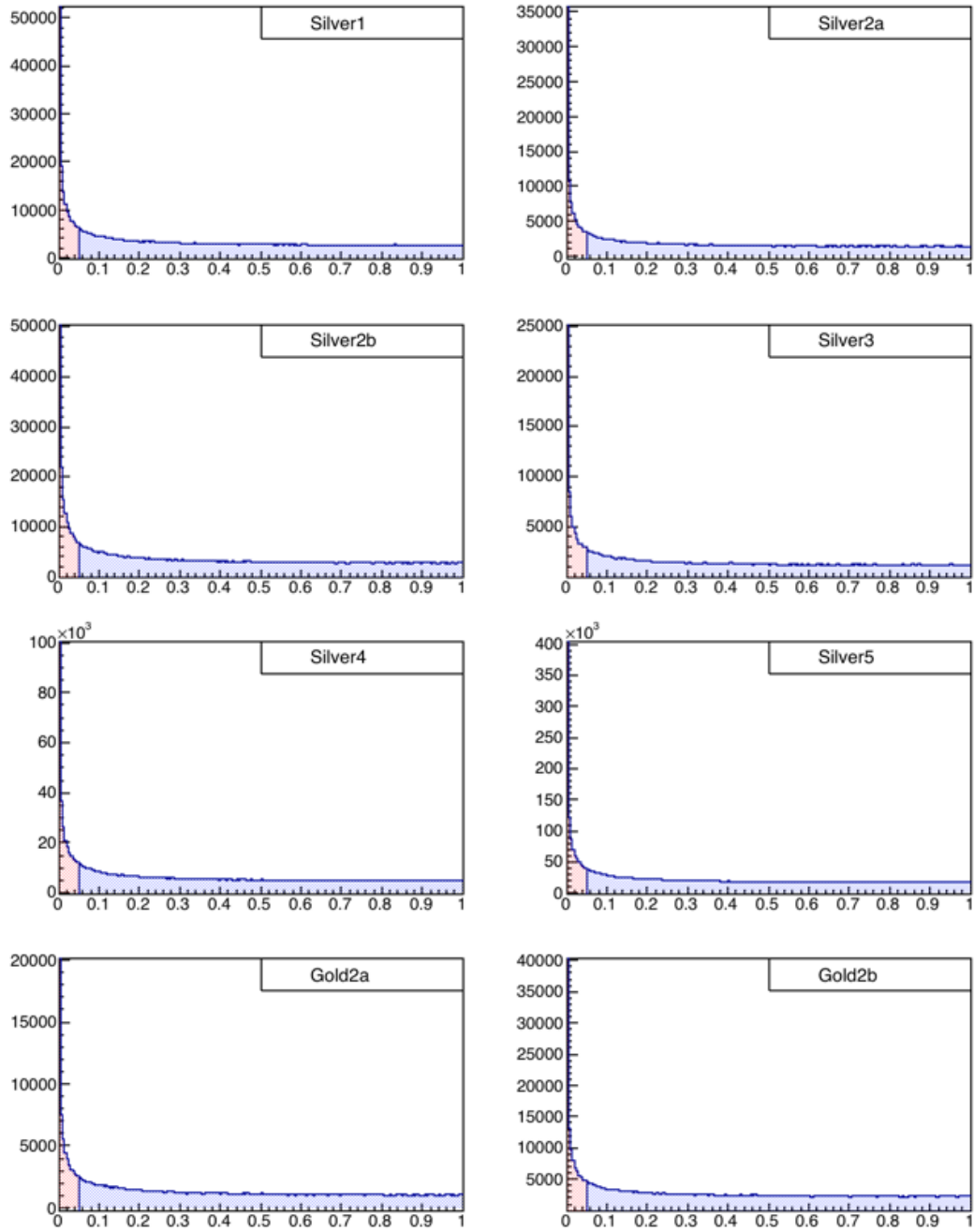


Figure 1.23: 5% confidence level cut for all circular runs for the reaction $\gamma(n) \rightarrow p\pi^-$.

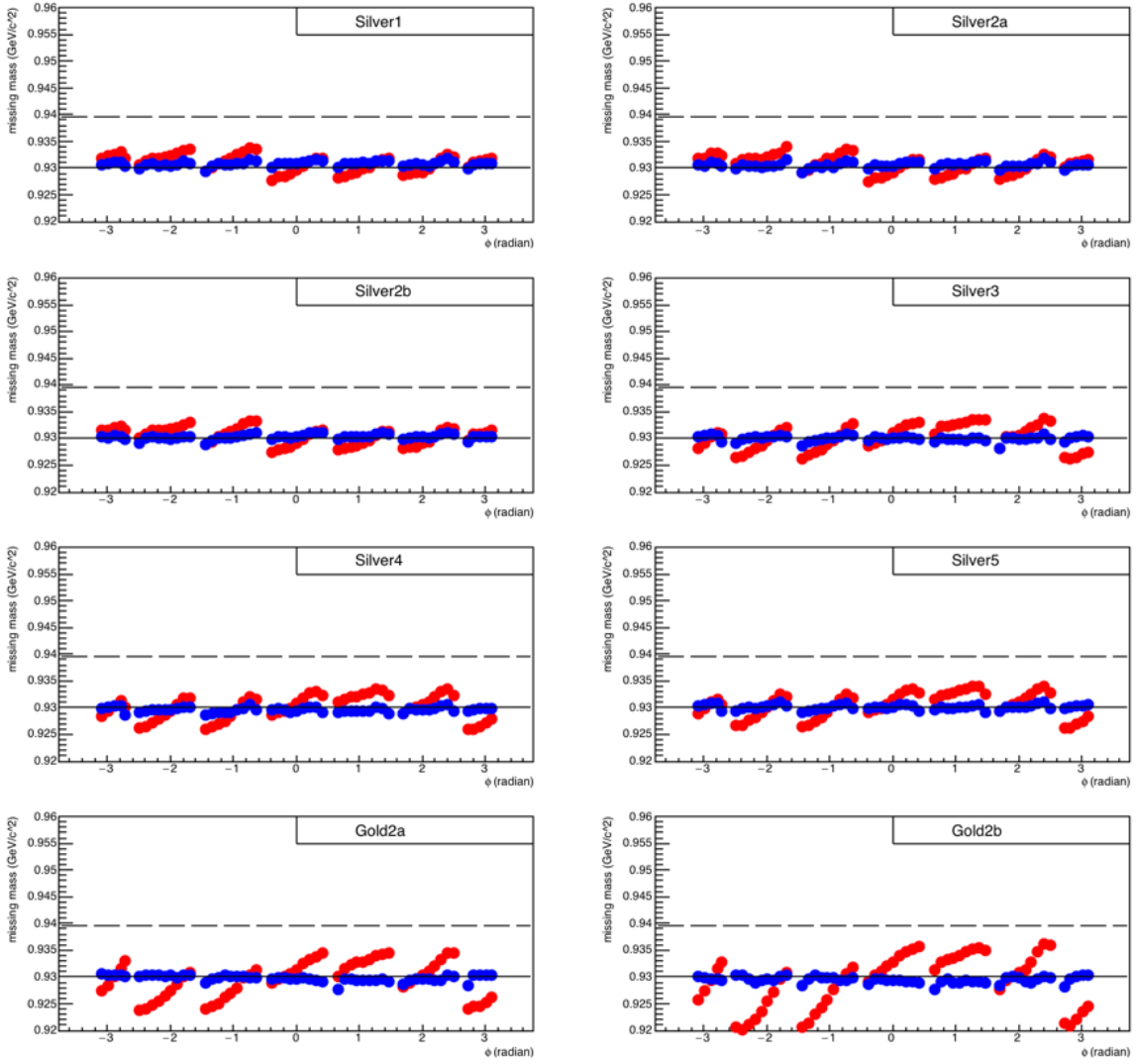


Figure 1.24: Missing Mass vs. ϕ_{pro} for the reaction $\gamma(n) \rightarrow p\pi^-$ for all circular periods.

the binding energy is 0.00223 GeV, $m^* \approx m - C \times 0.00223$, where C is a constant, which is estimated to be 4.3 as studied in Appendix. This gives $m^* \approx 0.930$ GeV.

Period	Pull Dist.	P_p	λ_p	ϕ_p	P_{π^-}	λ_{π^-}	ϕ_{π^-}	E_γ
Silver1	Mean	0.02	0.06	-0.01	0.01	-0.03	0.02	-0.01
	Sigma	1.11	1.04	1.11	1.12	1.07	1.11	1.11
Silver2a	Mean	0.02	0.06	-0.02	0.02	-0.04	0.03	-0.02
	Sigma	1.10	1.02	1.10	1.10	1.05	1.10	1.10
Silver2b	Mean	0.05	0.04	-0.05	0.05	-0.01	0.06	-0.04
	Sigma	1.12	1.03	1.11	1.12	1.07	1.12	1.12
Silver3	Mean	0.04	-0.03	0.06	0.03	0.02	-0.03	-0.03
	Sigma	1.03	0.94	1.02	1.04	1.00	1.04	1.04
Silver4	Mean	0.09	-0.02	0.10	0.09	-0.03	-0.08	-0.08
	Sigma	1.02	0.95	1.02	1.03	1.00	1.03	1.03
Silver5	Mean	0.01	-0.08	0.02	-0.00	0.02	0.00	0.00
	Sigma	0.97	0.91	0.97	0.98	0.95	0.98	0.98
Gold2a	Mean	-0.03	-0.03	-0.02	-0.04	0.05	0.04	0.04
	Sigma	1.04	0.98	1.03	1.04	1.03	1.04	1.04
Gold2b	Mean	-0.02	-0.03	-0.01	-0.03	0.04	0.03	0.03
	Sigma	1.05	0.98	1.04	1.04	1.03	1.05	1.04

Table 1.4: Mean and sigma values of the pull distributions for all the circularly run periods for channel $\gamma(n) \rightarrow p\pi^-$.

Chapter 2

E asymmetry for $\gamma n \rightarrow p\pi^-$

An accurate evaluation of the electromagnetic couplings in meson photo-production remains unknown due to the lack of experiment data on the neutron targets. Moreover, the existing data on neutron target are mainly differential cross section, only 15% are from polarization observable measurement [34]. E asymmetry for $\gamma n \rightarrow p\pi^-$ is the first measurement for this polarization observable on the neutron target.

2.1 Formalism

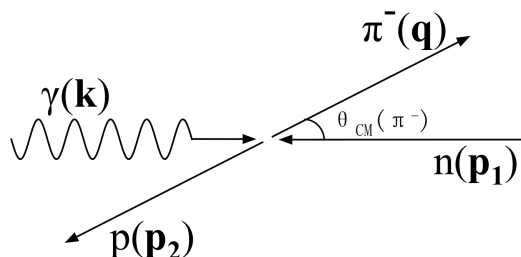


Figure 2.1: Kinematics diagram for π^- photoproduction off neutron target in the center of mass frame, \mathbf{k} , \mathbf{p}_1 , \mathbf{q} , \mathbf{p}_2 are the momenta for the incident photon, neutron target, and final state π^- and recoiled proton, $\theta_{CM}(\pi^-)$ is the polar angle of π^- in center of mass frame.

For a reaction of a photon scattering off a nucleon, the four-momenta of the incident photon, the outgoing pion, the initial nucleon and final nucleon are denoted by $k = (\mathbf{k}, k)$, $q = (\mathbf{q}, \omega)$, $p_1 = (\mathbf{p}_1, E_1)$, $p_2 = (\mathbf{p}_2, E_2)$. The photo-production amplitude A relates to the S matrix by the following equation:

$$S = 1 + (2\pi)^4 i \delta^4(P_f - P_i) (8\pi W N) A, \quad (2.1)$$

where $P_i = k + p_1$, $P_f = q + p_2$, $W^2 = s = (k + p_1)^2$, $N = (16k\omega E_1 E_2)^{1/2}$ is a normalization factor.

Since the electromagnetic interaction violates isospin conservation, the transition operator can be decomposed into an isoscalar part \hat{S} and an isovector part \hat{V} , the

pion(isovector meson) photo-production amplitude A has three independent matrix elements with the notation $\langle I_f, I_{f3} | \hat{A} | I_i, I_{i3} \rangle$ [35, 36]:

$$\begin{aligned} A^{IS} &= \langle \frac{1}{2}, \pm \frac{1}{2} | \hat{S} | \frac{1}{2}, \pm \frac{1}{2} \rangle, \\ \mp A^{IV} &= \langle \frac{1}{2}, \pm \frac{1}{2} | \hat{V} | \frac{1}{2}, \pm \frac{1}{2} \rangle, \\ A^{V3} &= \langle \frac{3}{2}, \pm \frac{1}{2} | \hat{V} | \frac{1}{2}, \pm \frac{1}{2} \rangle. \end{aligned} \quad (2.2)$$

The determination of the three isospin amplitudes can be obtained from the following four photoproduction reactions.

$$\begin{aligned} A(\gamma p \rightarrow \pi^+ n) &= -\sqrt{\frac{1}{3}} A^{V3} + \sqrt{\frac{2}{3}} (A^{IV} - A^{IS}), \\ A(\gamma p \rightarrow \pi^0 p) &= +\sqrt{\frac{2}{3}} A^{V3} + \sqrt{\frac{1}{3}} (A^{IV} - A^{IS}), \\ A(\gamma n \rightarrow \pi^- p) &= +\sqrt{\frac{1}{3}} A^{V3} - \sqrt{\frac{2}{3}} (A^{IV} + A^{IS}), \\ A(\gamma n \rightarrow \pi^0 n) &= +\sqrt{\frac{2}{3}} A^{V3} + \sqrt{\frac{1}{3}} (A^{IV} + A^{IS}), \end{aligned} \quad (2.3)$$

The way to get the above expressions can be found in [36], an example for $\gamma n \rightarrow \pi^- p$ is shown in the following. The isospin part of the wave function for nucleon and pion be written as:

$$\begin{aligned} |p\rangle &= |\frac{1}{2}, +\frac{1}{2}\rangle, |n\rangle = |\frac{1}{2}, -\frac{1}{2}\rangle, \\ |\pi^+\rangle &= -|1, +1\rangle, |\pi^0\rangle = |1, 0\rangle, |\pi^-\rangle = |1, -1\rangle \end{aligned} \quad (2.4)$$

For the reaction $\gamma n \rightarrow \pi^- p$, the initial state isospin wave function is $|\gamma n\rangle = |\frac{1}{2}, -\frac{1}{2}\rangle$. The final state isospin wave function is $|\pi^- p\rangle = |1, -1\rangle |\frac{1}{2}, +\frac{1}{2}\rangle = \sqrt{\frac{1}{3}} |\frac{3}{2}, -\frac{1}{2}\rangle - \sqrt{\frac{2}{3}} |\frac{1}{2}, -\frac{1}{2}\rangle$. The transition amplitude A for this reaction is:

$$\begin{aligned} A(\gamma n \rightarrow \pi^- p) &= \langle \pi^- p | \hat{A} | \gamma n \rangle \\ &= (\sqrt{\frac{1}{3}} \langle \frac{3}{2}, -\frac{1}{2} | - \sqrt{\frac{2}{3}} \langle \frac{1}{2}, -\frac{1}{2} |) \hat{S} + \hat{V} | \frac{1}{2}, -\frac{1}{2} \rangle \\ &= +\sqrt{\frac{1}{3}} A^{V3} - \sqrt{\frac{2}{3}} (A^{IV} + A^{IS}). \end{aligned} \quad (2.5)$$

Equation 2.3 shows that A^{V3} can be obtained from only the reaction using proton target, the other two component can only be separated using both the proton data and the neutron data. For each reaction in Equation 2.3, the amplitude can be decomposed into helicity amplitudes or CGLN amplitudes. Helicity is the projection of spin onto the direction of momentum: $\lambda_k = \pm 1$ for incident photon, $\lambda_1 = \pm 1/2$ for initial nucleon, $\lambda_2 = \pm 1/2$ for final nucleon, $\lambda_k = 0$ for pion. The initial and final state helicities

$\lambda = \lambda_k - \lambda_1 = \pm 1/2, \pm 3/2$ and $\mu = \lambda_q - \lambda_2 = \pm 1/2$ give eight helicity amplitudes $A_{\mu\lambda}$. The eight helicity amplitudes are not independent, parity conservation relates the four amplitudes with $\lambda_k = 1$ to $\lambda_k = -1$ by $A_{-\mu, -\lambda}(\theta, \phi) = -e^{i(\lambda-\mu)(\pi-2\phi)} A_{\mu, \lambda}(\theta, \phi)$ [37].

The four independent amplitudes are all complex number, and eight independent measurements are required to determine the production amplitude A without ambiguities.

There are 16 nonzero observables for single pseudo-scalar meson photo-production as below [38]:

$$\begin{aligned}
& \frac{d\sigma}{d\Omega}(\vec{P}^\gamma, \vec{P}^T, \vec{P}^R) \\
&= \frac{1}{2} \{ d\sigma_0 [1 - P_L^\gamma P_y^T P_{y'}^R \cos(2\phi_\gamma)] + \hat{\Sigma} [-P_L^\gamma \cos(2\phi_\gamma) + P_y^T P_{y'}^R] \\
&\quad + \hat{T} [P_y^T - P_L^\gamma P_{y'}^R \cos(2\phi_\gamma)] + \hat{P} [P_{y'}^R - P_L^\gamma P_y^T \cos(2\phi_\gamma)] \\
&\quad + \hat{E} [-P_c^\gamma P_z^T + P_L^\gamma P_x^T P_{y'}^R \sin(2\phi_\gamma)] + \hat{G} [P_L^\gamma P_z^T \sin(2\phi_\gamma) + P_c^\gamma P_x^T P_{y'}^R] \\
&\quad + \hat{F} [P_c^\gamma P_x^T + P_L^\gamma P_z^T P_{y'}^R \sin(2\phi_\gamma)] + \hat{H} [P_L^\gamma P_x^T \sin(2\phi_\gamma) - P_c^\gamma P_z^T P_{y'}^R] \\
&\quad + \hat{C}_{x'} [P_c^\gamma P_{x'}^R - P_L^\gamma P_y^T P_{z'}^R \sin(2\phi_\gamma)] + \hat{C}_{z'} [P_c^\gamma P_{z'}^R + P_L^\gamma P_y^T P_{x'}^R \sin(2\phi_\gamma)] \\
&\quad + \hat{O}_{x'} [P_L^\gamma P_{x'}^R \sin(2\phi_\gamma) + P_c^\gamma P_y^T P_{z'}^R] + \hat{O}_{z'} [P_L^\gamma P_{z'}^R \sin(2\phi_\gamma) - P_c^\gamma P_y^T P_{x'}^R] \\
&\quad + \hat{L}_{x'} [P_z^T P_{x'}^R + P_L^\gamma P_x^T P_{z'}^R \cos(2\phi_\gamma)] + \hat{L}_{z'} [P_z^T P_{z'}^R - P_L^\gamma P_x^T P_{x'}^R \cos(2\phi_\gamma)] \\
&\quad + \hat{T}_{x'} [P_x^T P_{x'}^R - P_L^\gamma P_z^T P_{z'}^R \cos(2\phi_\gamma)] + \hat{T}_{z'} [P_x^T P_{z'}^R + P_L^\gamma P_z^T P_{x'}^R \cos(2\phi_\gamma)] \}
\end{aligned} \tag{2.6}$$

In Eq. 2.6, P_L^γ and P_c^γ are the degree of polarization for circular and linear polarized photon beam. P_i^T and P_i^R are the degree of polarization of target and recoil nucleon. $d\sigma_0$ is the unpolarized differential cross section. Three asymmetries which to leading order scaled by a single polarization of either beam, target or recoil (Σ , T , P) are single polarization asymmetries. Three sets of four asymmetries whose leading polarization dependence involves two polarizations of either beam–target (E , F , G , H), beam–recoil ($C_{x'}$, $C_{z'}$, $O_{x'}$, $O_{z'}$), or target–recoil ($L_{x'}$, $L_{z'}$, $T_{x'}$, $T_{z'}$) are double polarization asymmetries. Each of the double polarization asymmetry has two way to be measured in experiment, take the beam-target asymmetry E as an example, $2\hat{E} = \sigma(+1, -z, 0) - \sigma(+1, +z, 0)$ (target polarization is flipped) or $2\hat{E} = \sigma(+1, -z, 0) - \sigma(-1, -z, 0)$ (beam polarization is flipped). The 16 observables are not independent, their are 37 relations between them as in appendix C of [38].

Figure 2.2 shows the list of observables that can be measured for single pseudo-scalar meson photo-production. The cross section σ_0 is un-polarization measurement, Σ, T, P are single-polarization asymmetries, and $E, F, G, H, Cx, Cz, Ox, Oz, Lx, Lz, Tx, Tz$ are double polarization asymmetries. The complete experiment that eliminates ambiguities requires a minimum of eight observables, which can be chosen to be σ_0, Σ, T, P and four double-polarization asymmetries with at least one involving recoil polarization. For the channel $\gamma n \rightarrow p\pi^-$, there are 1381 cross section points between 0.4 and 2.0 GeV, only 326 single-polarization (Σ, T, P) points, and none for the double polarization asymmetries. The G14 experiment has measured two more new asymmetries for this reaction: E with circular polarized beam, and G with linear polarized beam. This Chapter will show the result for the E asymmetry.

This reaction needs two independent variables to determine the kinematics, which can be chosen to be the total energy W and the polar angle of π^- $\theta_{CM}(\pi^-)$ in c.m frame. W

Photon beam		Target			Recoil			Target + Recoil								
					x'	y'	z'	x'	x'	x'	y'	y'	y'	z'	z'	z'
		x	y	z				x	y	z	x	y	z	x	y	z
Unpolarized	σ_0		T			P		$T_{x'}$		$L_{x'}$		Σ		$T_{z'}$		$L_{z'}$
$P_T \sin(2\phi_\gamma)$		H		G	$O_{x'}$		$O_{z'}$		$C_{z'}$		E		F		$-C_{x'}$	
$P_T \cos(2\phi_\gamma)$	$-\Sigma$		-P			-T		$-L_{z'}$		$T_{z'}$		$-\sigma_0$		$L_{x'}$		$-T_{x'}$
Circular P_c^y		F		-E	$C_{x'}$		$C_{z'}$		$-O_{z'}$		G		-H		$O_{x'}$	

Figure 2.2: Polarization observables in the reaction of pseudoscalar meson photo-production. Each observable can be measured in two different methods in the table. The observables in blue cells are measured in previous experiments, the ones in yellow cells are new observables that are measured in G14 experiment. Image source: [38]

is divided into 21 bins from 1500 MeV to 2300 MeV with the bin size of 40 MeV. $\theta_{CM}(\pi^-)$ is divided into 13 bins from $\cos(\theta_{CM}(\pi^-)) = -0.975$ to $\cos(\theta_{CM}(\pi^-)) = 0.975$ with the bin size of 0.15. The E asymmetry will be calculated for each 21×13 bins.

2.2 Extraction of E asymmetry

The E asymmetry is a beam target double polarization asymmetry as shown in Figure 2.2. The normalized E is defined as:

$$E = \frac{\sigma(+1, -z, 0) - \sigma(-1, -z, 0)}{\sigma(+1, -z, 0) + \sigma(-1, -z, 0)}, \quad (2.7)$$

where the first value in the parenthesis represents the helicity of the circular polarized photon beam, the second value represents the direction of polarization for the longitudinal polarized target, and the third value represents the recoil nucleon polarization. Taking into account of the degree of polarization for photon beam and target, and relating the cross section to the yields of events, we can write the beam target asymmetry E and its statistical error as:

$$E = \frac{1}{P_\gamma P_t} \frac{N_{1/2} - N_{3/2}}{N_{1/2} + N_{3/2}} \quad (2.8)$$

$$\sigma_E = \frac{1}{P_\gamma P_t} \frac{2(N_{1/2}N_{3/2})^{1/2}}{(N_{1/2} + N_{3/2})^{3/2}}$$

where P_γ, P_t are degrees of polarization for photon beam and target. $N_{1/2}$ is the total number of events for beam polarization and target polarization are anti parallel, $N_{3/2}$ is the total number of events for beam polarization and target polarization are parallel.

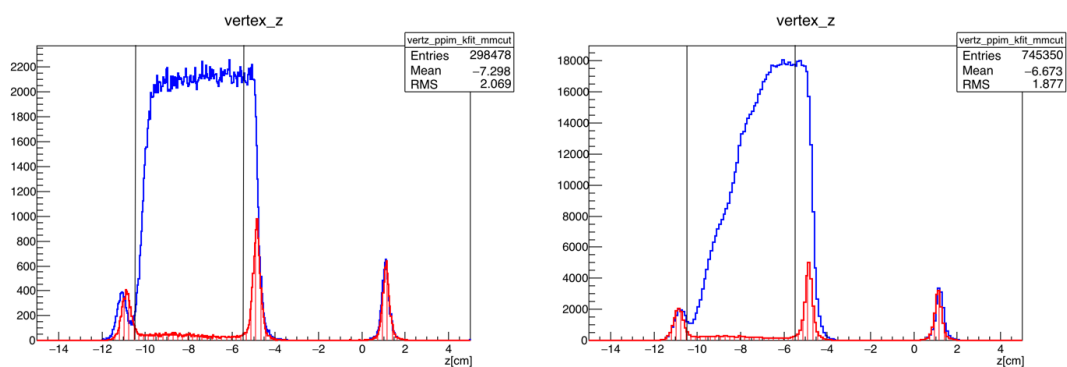
Since the HD target has aluminum wires and Kelf in the target region. We need to make corrections to the E asymmetry caused by the aluminum background.

$$E^{raw} = \frac{1}{P_\gamma P_t} \frac{N_{1/2} - N_{3/2}}{N_{1/2} + N_{3/2} + N_{empty}} = \frac{1}{P_\gamma P_t} \frac{N_{1/2} - N_{3/2}}{(N_{1/2} + N_{3/2})(1 + \frac{N_{empty}}{N_{1/2} + N_{3/2}})}, \quad (2.9)$$

$$E = \left(1 + \frac{N_{empty}}{N_{1/2} + N_{3/2}}\right) E^{raw}, \quad (2.10)$$

where N_{empty} is the scaled total number of events from empty target run, E^{raw} is E asymmetry before empty target correction, E is E asymmetry after empty target correction.

For the 8 data sets in circular runs, corrections for E asymmetry from background are done for each data set separately. Figure 2.3 shows two examples from Gold2b and Silver 1 for the comparison of z vertex between full target run and empty target run. Since the empty target run and full target run have different beam time, the empty run events have to be scaled with a constant number. This number is calculated by comparing the events from the KelF peak between $z = 0$ cm to $z = 2$ cm as in Figure 2.3, this scale constant is 0.83 for gold2a and 1.21 for silver1. Moreover, the empty run and all the silver runs use the same target cell (21a), the gold2 runs have used a different target cell (19b). The amount of aluminum wires is different in these two cells, the 19b target only has 70% of the aluminum wires used in 21a. Within the target region: -10.5 cm



(a) Comparison of z vertex between Gold2b(blue line) and Empty-a(red line) periods. (b) Comparison of z vertex between Silver1(blue line) and Empty-a(red line) periods.

Figure 2.3: Empty target correction for E asymmetry.

$< z < -5.5$ cm, the ratio of events between the empty target run and the full target run can be calculated using the above information. For gold 2a run period, the ratio is $(10978 \cdot 0.80 \cdot 0.70) / 251974 = 0.024$, where 0.80 is the scale factor for empty run, 0.70 is the ratio of aluminum wires between gold2a target cell and empty-a target cell. For silver 1 run period, the ratio is $(16796 \cdot 0.91) / 428213 = 0.036$.

The correction values of E asymmetry for these two periods are given as: $E = 1.024E^{raw}$ for gold2a period and $E = 1.036E^{raw}$ for silver1 period. It is found that the correction values depends on the c.m. energy W , a detailed study for this dependence is shown in appendix C.

The results of E asymmetry for each run periods (silver1, silver2a, silver2b, gold2a, gold2b), and the results combining all periods with the method of weighted mean are shown in the following figures. In each figure, the two blue lines are from Bonn-Gatchina 2011-2 predictions for E asymmetry [39], the two lines correspond to the upper and lower energy boundary for each energy bin. The two red lines are from SAID CM12 predictions [40].

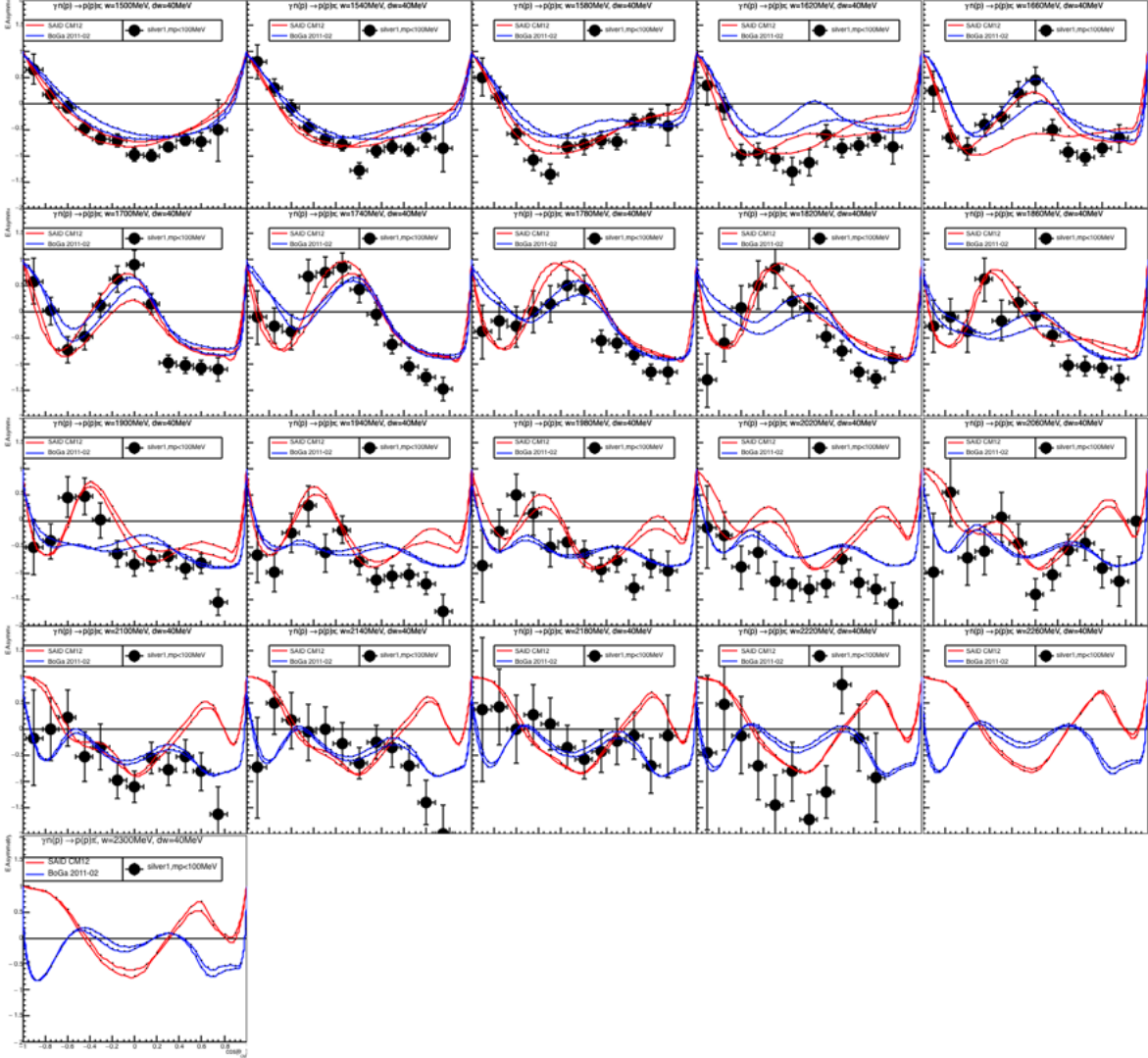


Figure 2.4: Silver 1 run period: E asymmetry vs $\cos(\theta_{CM})$ for different center of momentum energy W .

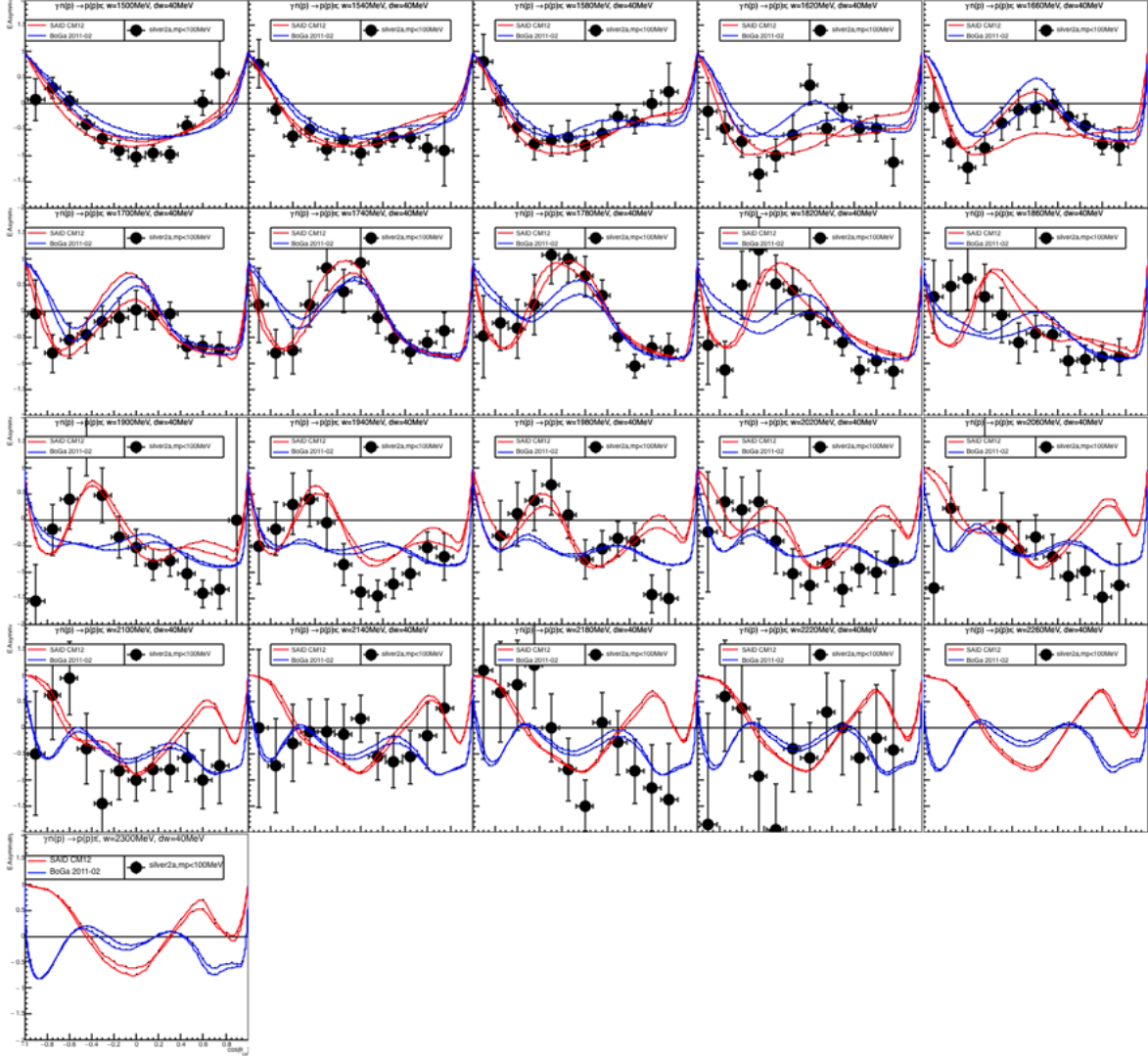


Figure 2.5: Silver 2a run period: E asymmetry vs $\cos(\theta_{CM})$ for different center of momentum energy W .

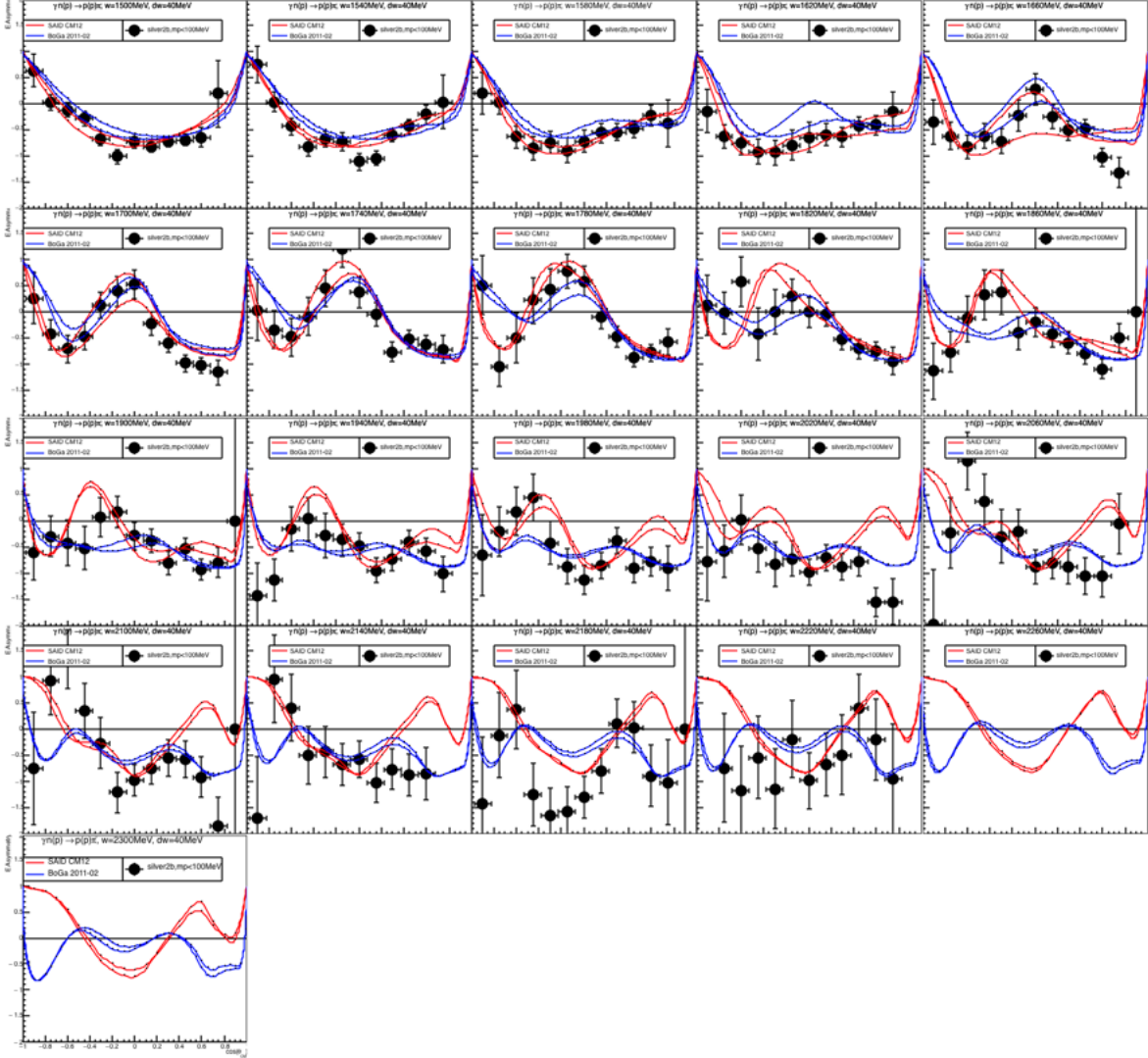


Figure 2.6: Silver 2b run period: E asymmetry vs $\cos(\theta_{CM})$ for different center of momentum energy W .

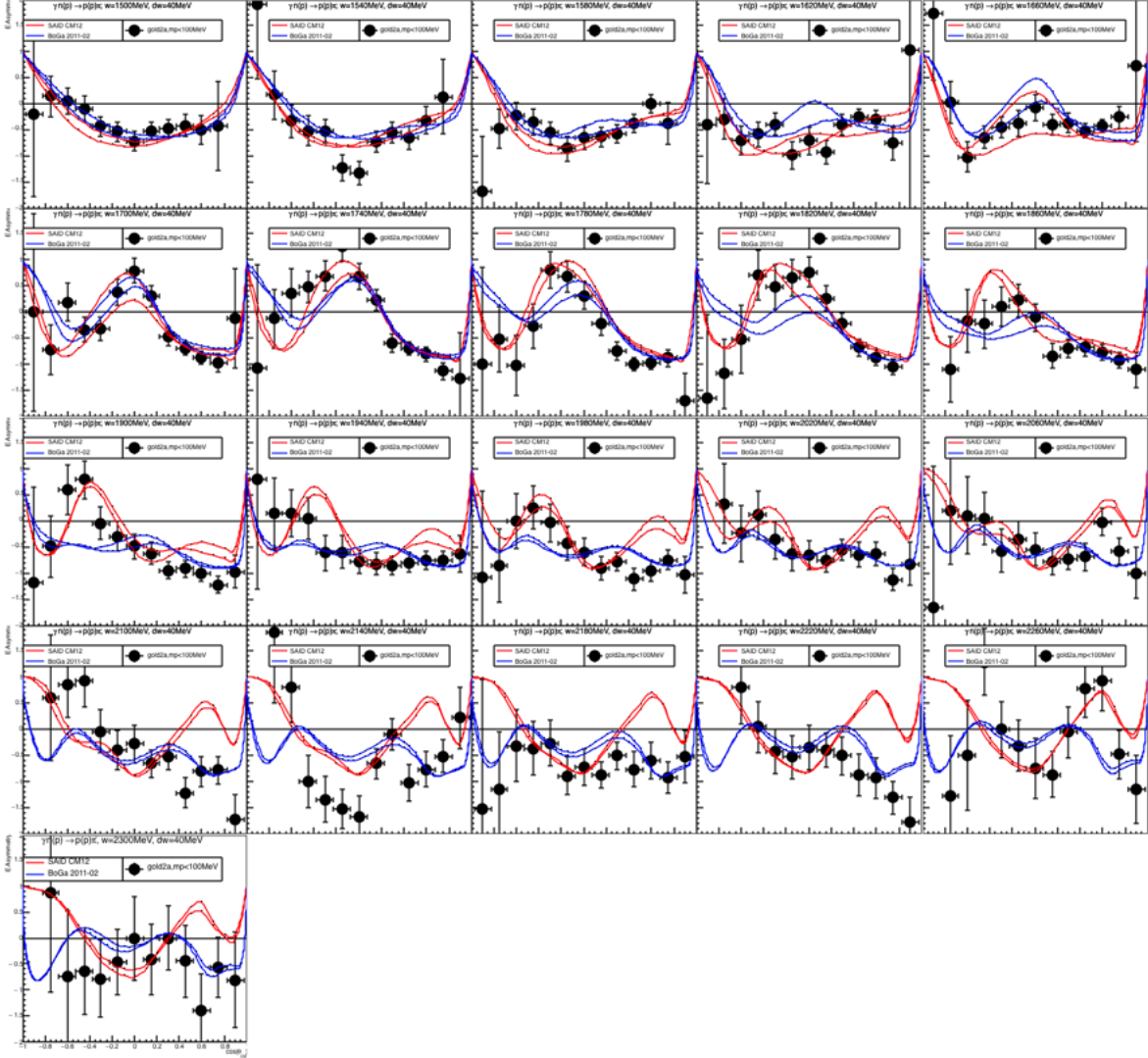


Figure 2.7: Gold 2a run period: E asymmetry vs $\cos(\theta_{CM})$ for different center of momentum energy W .

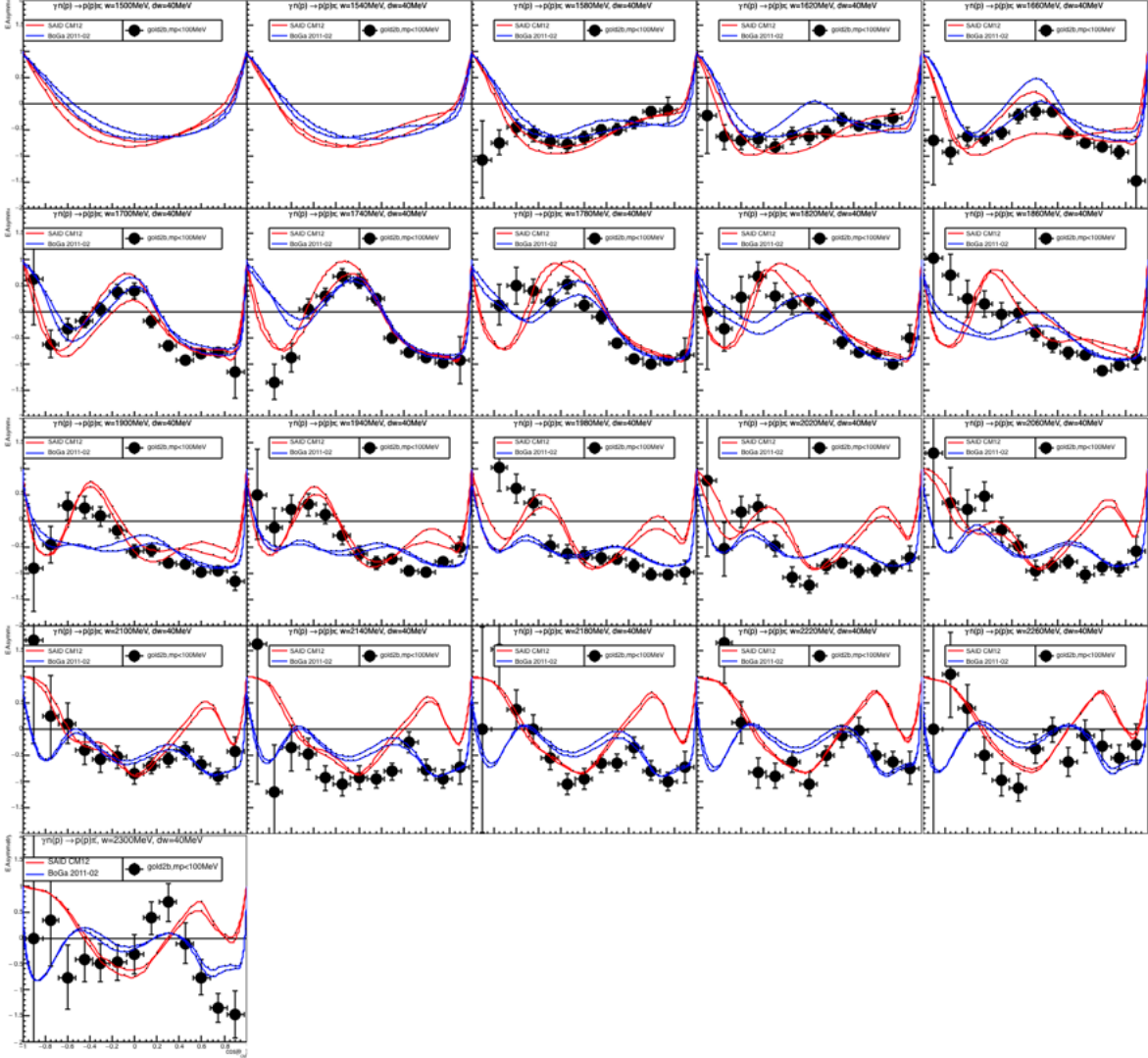


Figure 2.8: Gold 2b run period: E asymmetry vs $\cos(\theta_{CM})$ for different center of momentum energy W .

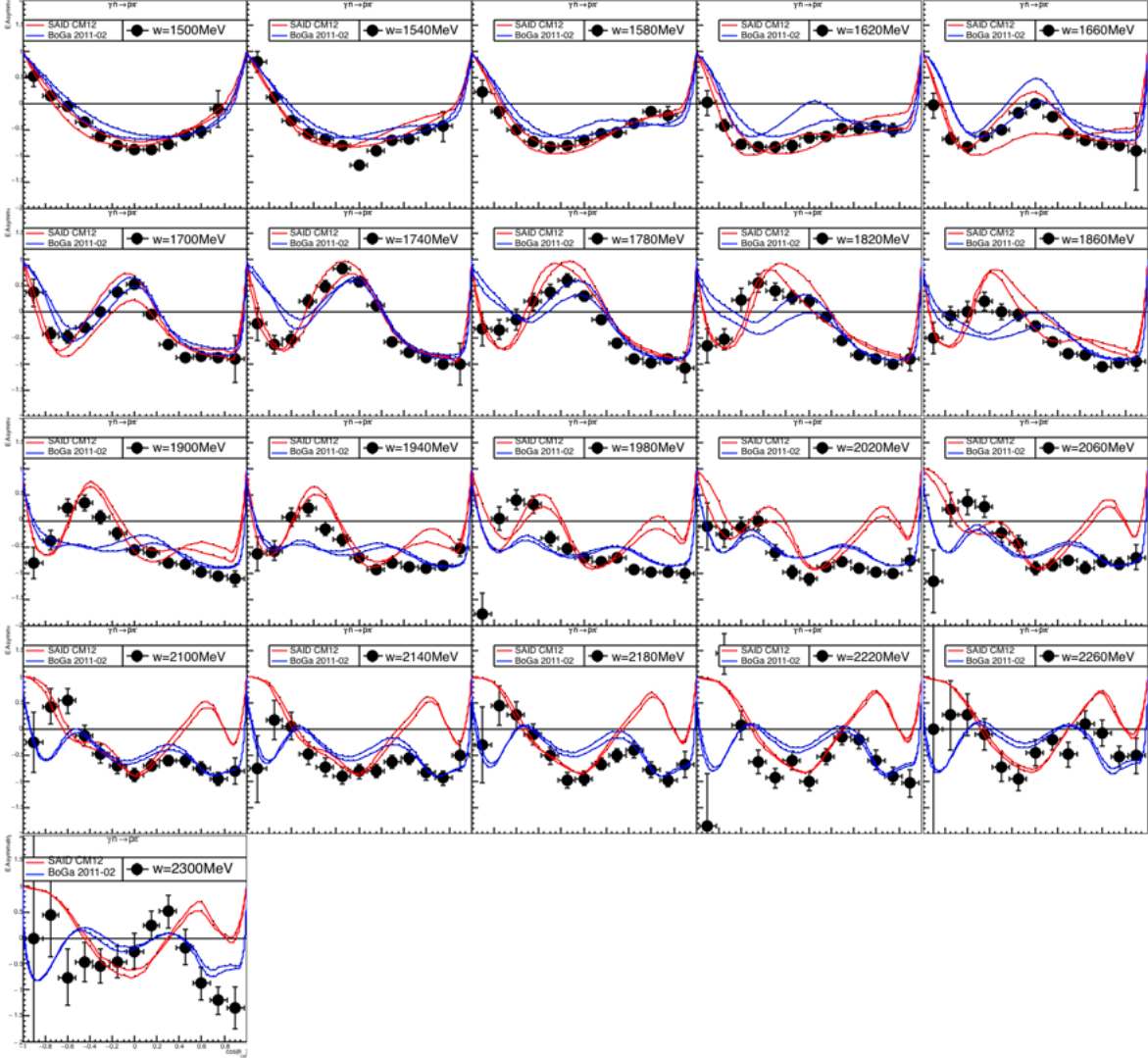


Figure 2.9: Combined result: E asymmetry vs $\cos(\theta_{CM})$ for different center of momentum energy W .

2.3 Systematic Studies

Different values on the cuts used in the channel selection procedure will affect the final results for the E asymmetry. This section studies the systematic errors induced by using different "vertex z" cuts, "confidence level" cuts, and "missing momentum" cuts. The systematic error is defined in the following way:

1. E asymmetry is calculated for each $\cos(\theta_{CM})$ and energy W bin for cut 1 and cut 2 respectively, there are 13 $\cos(\theta_{CM})$ bins and 21 W bins, which give a total of $13 \times 21 = 273$ bins.

2. The difference of the E asymmetry is calculated using the two different cuts: $\delta E = E_{cut1} - E_{cut2}$, and the results are used to fill a 1-D histogram, which will be fitted with a Gaussian distribution. The mean (μ_δ) of the Gaussian is systematic error caused by using these two different cuts.

3. Calculate the mean (μ_δ) and width (σ_δ) of the Gaussian distribution of $\delta E = E_{cut1} - E_{cut2}$ for all the circular beam run periods, and use weighted mean to obtain the overall systematic error.

$$\sigma_{systematic} = \frac{\sqrt{\frac{\mu_{Silver1}^2}{\sigma_{\mu Silver1}^2} + \frac{\mu_{Silver2a}^2}{\sigma_{\mu Silver2a}^2} + \frac{\mu_{Silver2b}^2}{\sigma_{\mu Silver2b}^2} + \frac{\mu_{Gold2a}^2}{\sigma_{\mu Gold2a}^2} + \frac{\mu_{Gold2b}^2}{\sigma_{\mu Gold2b}^2}}{\sqrt{\frac{1}{\sigma_{\mu Silver1}^2} + \frac{1}{\sigma_{\mu Silver2a}^2} + \frac{1}{\sigma_{\mu Silver2b}^2} + \frac{1}{\sigma_{\mu Gold2a}^2} + \frac{1}{\sigma_{\mu Gold2b}^2}}}, \quad (2.11)$$

where $\sigma_\mu = \sigma_\delta / \sqrt{N}$ is the standard error of the mean value, N is the size of the sample.

2.3.1 Systematic Study for Vertex Z cuts

As shown in Chapter 3, section 3.3.2, there is a cut along the z-axis of the target: $-10.5\text{cm} < z < -5.5\text{ cm}$. This cut removes most of the events from the KelF target cell that enclose HD target. A variation of $\pm 0.2\text{ cm}$ of the vertex z cut is used to study the systematic effect of vertex z cut on E asymmetry.

Tightening 0.2 cm of the vertex z cut: $-10.3\text{ cm} < z < -5.7\text{ cm}$, the 1-D histogram of the difference between the E asymmetry calculated from the new vertex cut and standard vertex cut ($-10.5\text{ cm} < z < -5.5\text{ cm}$) for circular runs silver1, silver 2, and gold2 are shown in Figure 2.10. The systematic error caused by the change of vertex z cut is calculated using Equation 2.11, and result is shown in Table 2.1. The results for loosening 0.2 cm of the vertex z cut: $-10.7\text{cm} < z < -5.3\text{ cm}$ are shown in Figure 2.11 and Table ???. The total systematic error caused by tightening and loosening the vertex z cut is the quadrature sum of the two errors, which is: $\sigma_{systematic}(\text{vertex } z) = \sqrt{0.010^2 + 0.006^2} = 0.012$

2.3.2 Systematic Study for Confidence level cuts

To separate the events from channel of interest from the background events, a confidence level cut of "CL > 5%" is used. The systematic effect of this cut can be studied by varying the value for the cut. The E asymmetry will be calculated with the confidence level cuts of 2% and 10%, and the results will be compared with the E asymmetry with the 5% confidence level cut. The difference between the two E asymmetry for all bins (21 energy bins \times 13 θ bins) will be used to fill a 1-D histogram, and the mean and error of the fitted Gaussian distribution will be used to estimate the systematic error.

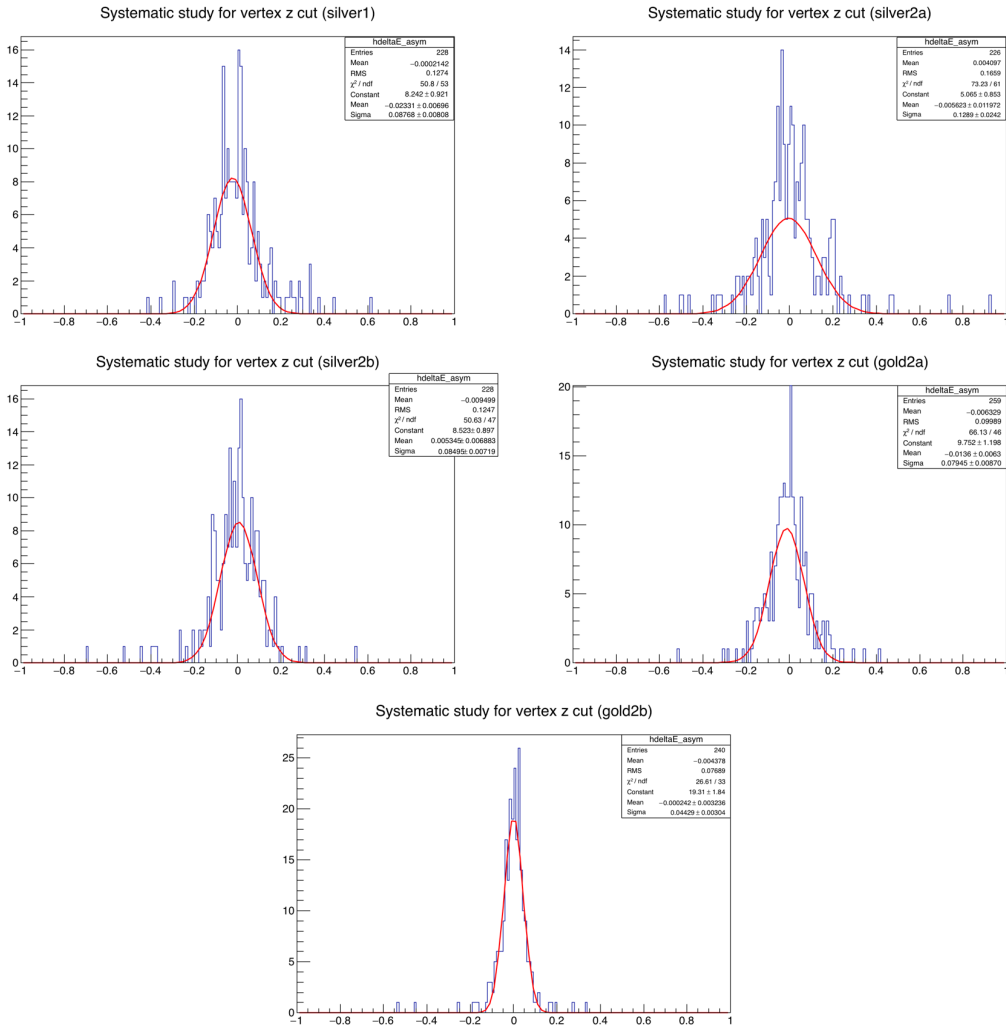


Figure 2.10: Difference between the E asymmetry calculated from the tight vertex cut ($-10.3 \text{ cm} < z < -5.7 \text{ cm}$) and standard vertex cut ($-10.5 \text{ cm} < z < -5.5 \text{ cm}$).

Period	μ_δ	σ_δ	N	σ_μ
Silver1	-0.023	0.088	228	0.006
Silver2a	-0.006	0.139	226	0.009
Silver2b	0.005	0.085	228	0.006
Gold2a	-0.014	0.079	259	0.005
Gold2b	0.000	0.044	240	0.003
$\sigma_{systematic}$	0.010			

Table 2.1: Mean and error for the Gaussian distribution in Figure 2.10. Equation 2.11 is used to calculate the systematic error between the vertex z cut: $-10.3 \text{ cm} < z < -5.7 \text{ cm}$ and $-10.5 \text{ cm} < z < -5.5 \text{ cm}$.

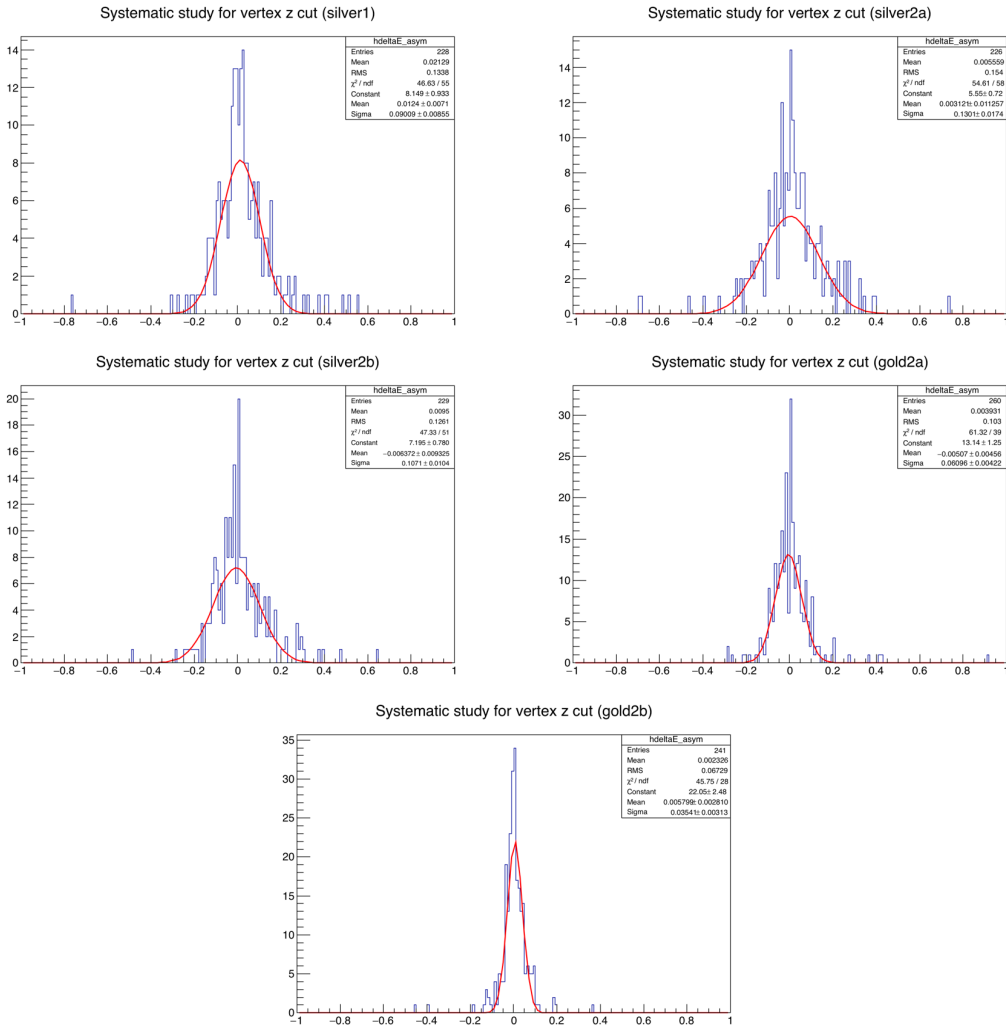


Figure 2.11: Difference between the E asymmetry calculated from the loose vertex cut ($-10.7 \text{ cm} < z < -5.3 \text{ cm}$) and standard vertex cut ($-10.5 \text{ cm} < z < -5.5 \text{ cm}$).

Period	μ_δ	σ_δ	N	σ_μ
Silver1	0.012	0.090	228	0.006
Silver2a	0.003	0.130	226	0.009
Silver2b	-0.006	0.107	229	0.007
Gold2a	-0.005	0.061	260	0.004
Gold2b	0.006	0.035	241	0.002
$\sigma_{systematic}$	0.006			

Table 2.2: Mean and error for the Gaussian distribution in Figure 2.11. Equation 2.11 is used to calculate the systematic error between the vertex z cut: $-10.7 \text{ cm} < z < -5.3 \text{ cm}$ and $-10.5 \text{ cm} < z < -5.5 \text{ cm}$.

The results of comparing the 2% and 5% confidence level cuts are shown in Figure 2.12 and Table 2.3.

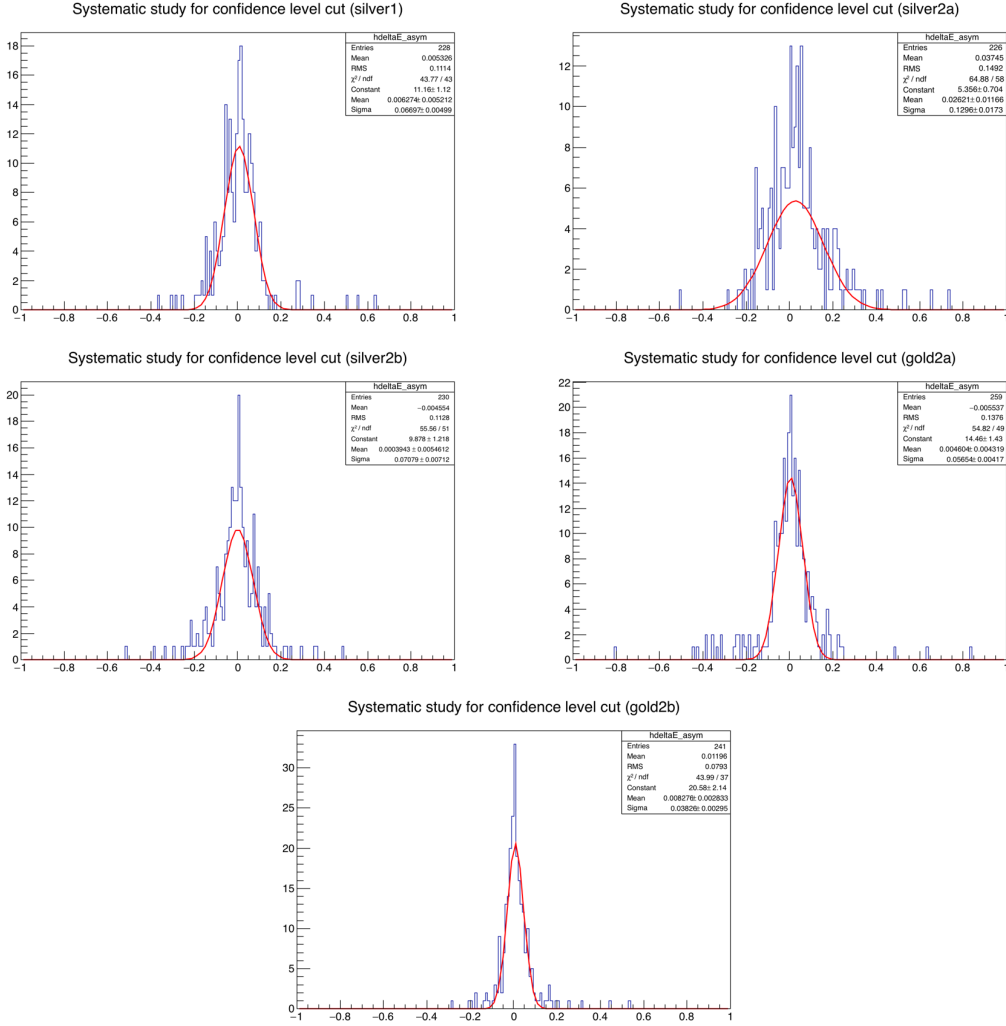


Figure 2.12: Difference between the E asymmetry calculated from confidence level cut (CL > 2%) and standard confidence level cut (CL > 5%).

The results of comparing the 10% and 5% confidence level cuts are shown in Figure 2.13 and Table 2.4. The total systematic error caused by tightening and loosening the confidence level cut is the quadrature sum of the two errors, which is: $\sigma_{systematic}(\text{confidence level}) = \sqrt{0.008^2 + 0.005^2} = 0.009$.

2.3.3 Systematic Study for Missing Momentum cuts

After the vertex z cut of $-10.5 < z < -5.5$ cm and confidence level cut of CL > 5%, most of the events are from the channel of interest: $\gamma + n \rightarrow p + \pi^-$, as shown in the missing momentum plot (Figure 2.14) for gold2a data set. The missing momentum of the target neutron can go up to 0.2 GeV, which shows the quasi free feature of the neutron target. Figure ?? shows that the E asymmetry depends on the missing momentum of the target neutron, the magnitude of E asymmetry decrease as missing momentum increase.

Period	μ_δ	σ_δ	N	σ_μ
Silver1	0.006	0.067	228	0.004
Silver2a	0.026	0.130	226	0.009
Silver2b	0.000	0.071	230	0.005
Gold2a	0.005	0.057	259	0.004
Gold2b	0.008	0.038	241	0.002
$\sigma_{systematic}$	0.008			

Table 2.3: Mean and error for the Gaussian distribution in Figure 2.12. Equation 2.11 is used to calculate the systematic error between the confidence level cut: $CL > 2\%$ and $CL > 5\%$.

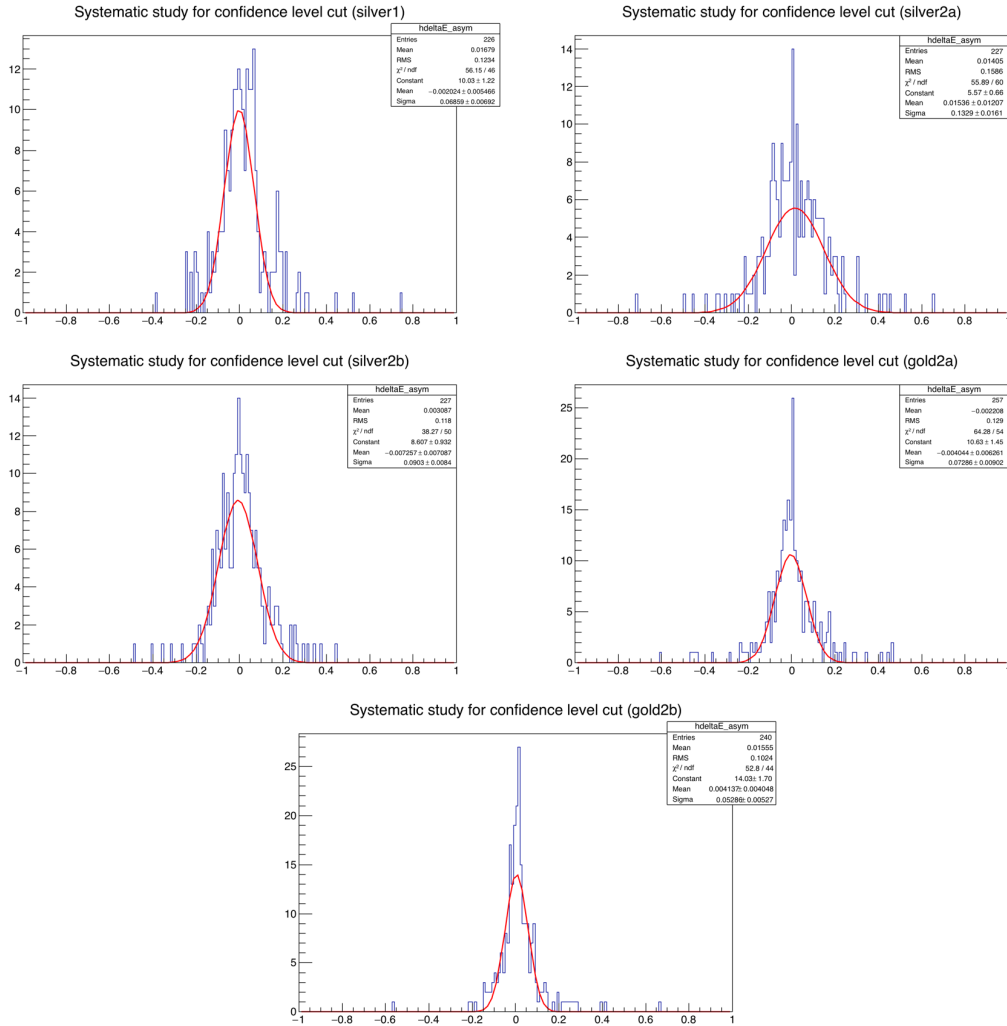


Figure 2.13: Difference between the E asymmetry calculated from confidence level cut ($CL > 10\%$) and standard confidence level cut ($CL > 5\%$).

Period	μ_δ	σ_δ	N	σ_μ
Silver1	-0.002	0.069	226	0.004
Silver2a	0.015	0.133	227	0.009
Silver2b	-0.007	0.090	227	0.005
Gold2a	-0.004	0.073	257	0.004
Gold2b	0.004	0.053	240	0.002
$\sigma_{systematic}$	0.005			

Table 2.4: Mean and error for the Gaussian distribution in Figure 2.13. Equation 2.11 is used to calculate the systematic error between the confidence level cut: $CL > 10\%$ and $CL > 5\%$.

A cut of missing momentum: $mP < 0.1$ GeV is choose for the standard cut, since the E asymmetry is relatively flat for the region: $0 < mP < 0.1$ GeV. Another two missing momentum cuts: $mP < 0.2$ GeV and $mP < 0.05$ GeV are used for calculating the E asymmetry, which will give the systematic error of the missing momentum cut.

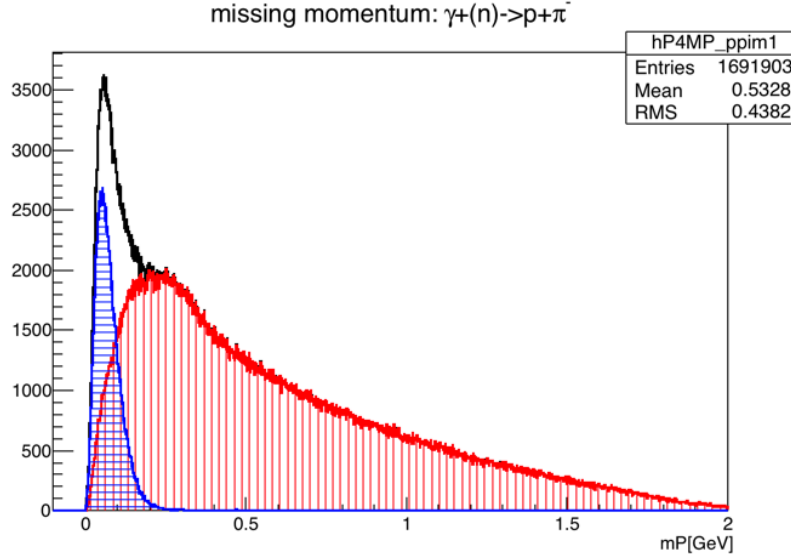


Figure 2.14: Missing momentum plot for channel $\gamma(n) \rightarrow p\pi^-$. The blue region is for good events that pass the cuts, the red region is the background events that are removed by the cuts.

The results of comparing the $mP < 0.2$ GeV and $mP < 0.1$ GeV missing momentum cuts are shown in Figure 2.16 and Table 2.5.

The results of comparing the $mP < 0.05$ GeV and $mP < 0.1$ GeV missing momentum cuts are shown in Figure 2.17 and Table 2.6. It is noticed that for $mP < 0.05$ GeV, only a few events pass this cut, the statistic is very low, and the systematic error from this comparison will not be used in the final result for the systematic error. The systematic error caused by using different missing momentum cuts is : $\sigma_{systematic}(\text{missing momentum}) = 0.027$.

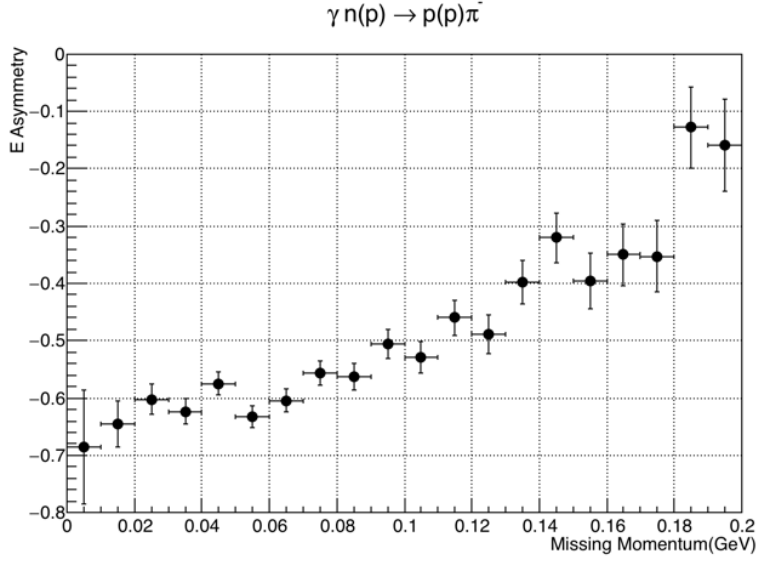


Figure 2.15: E asymmetry vs missing momentum of target neutron for the channel: $\gamma + (n) \rightarrow p + \pi^-$.

Period	μ_δ	σ_δ	N	σ_μ
Silver1	0.043	0.217	228	0.014
Silver2a	0.039	0.306	227	0.020
Silver2b	0.024	0.185	230	0.012
Gold2a	0.015	0.302	258	0.019
Gold2b	0.023	0.108	240	0.007
$\sigma_{systematic}$	0.027			

Table 2.5: Mean and error for the Gaussian distribution in Figure 2.16. Equation 2.11 is used to calculate the systematic error between the missing momentum cut: $mP < 0.2$ GeV and $mP < 0.1$ GeV.

Period	μ_δ	σ_δ	N	σ_μ
Silver1	-0.086	0.782	218	0.014
Silver2a	-0.162	0.927	213	0.020
Silver2b	-0.063	0.739	220	0.012
Gold2a	0.005	0.797	243	0.019
Gold2b	0.025	0.545	230	0.007
$\sigma_{systematic}$	0.072			

Table 2.6: Mean and error for the Gaussian distribution in Figure 2.16. Equation 2.11 is used to calculate the systematic error between the missing momentum cut: $mP < 0.05$ GeV and $mP < 0.1$ GeV.

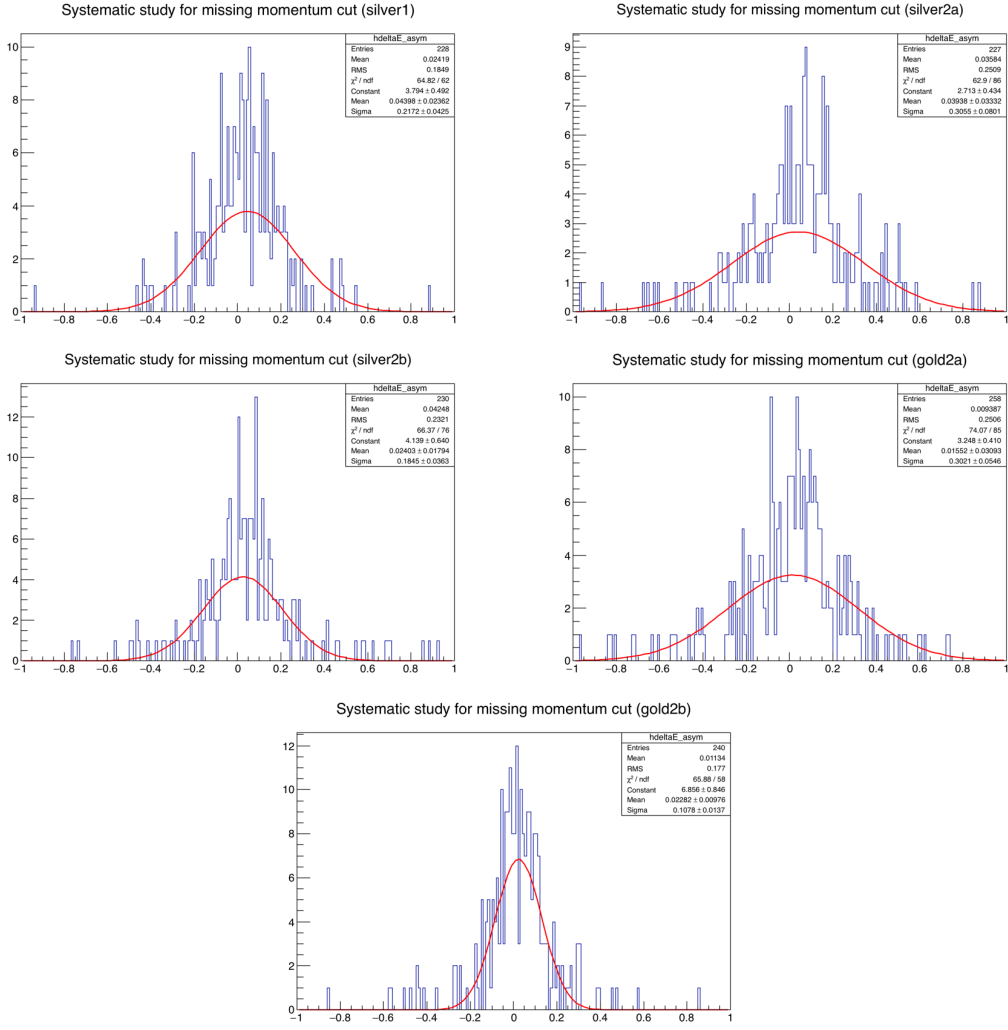


Figure 2.16: Difference between the E asymmetry calculated from missing momentum cut ($m_P < 0.2$ GeV) and standard missing momentum cut ($m_P < 0.1$ GeV).

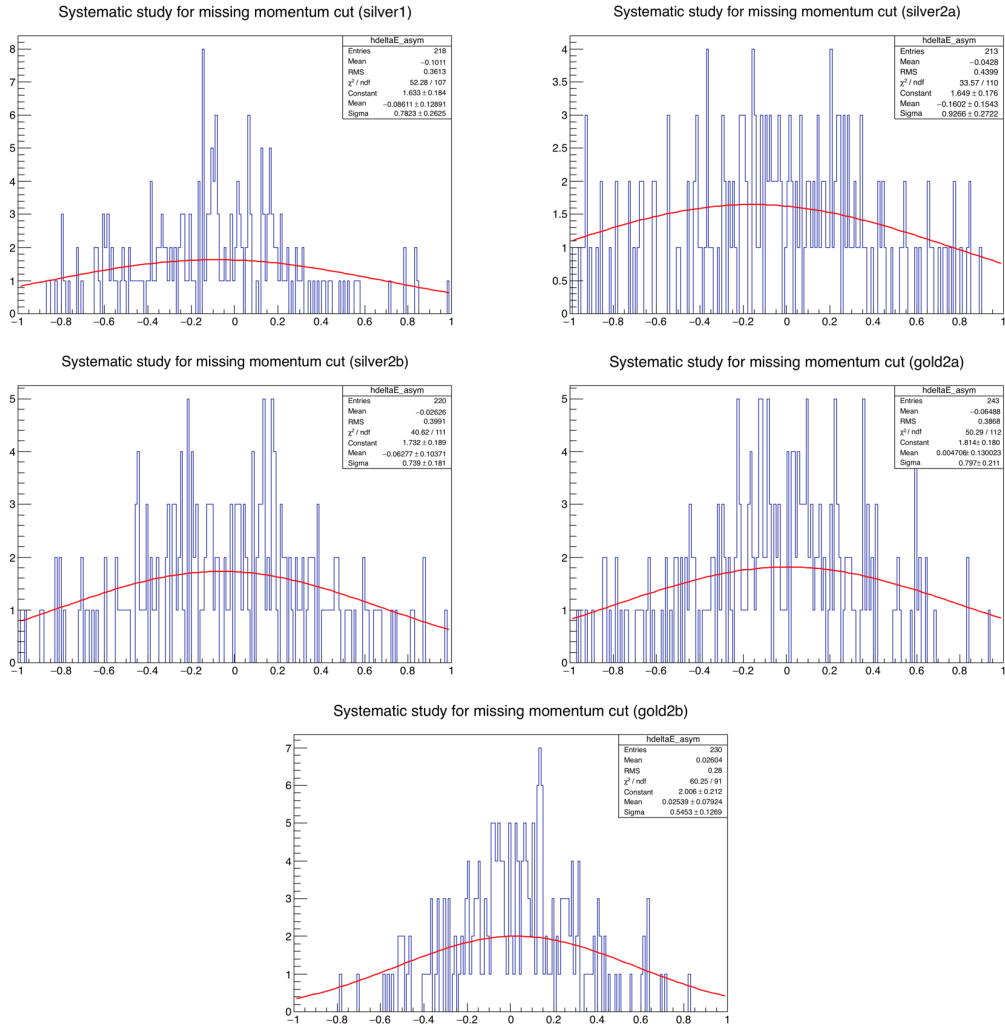


Figure 2.17: Difference between the E asymmetry calculated from missing momentum cut ($m_P < 0.05$ GeV) and standard missing momentum cut ($m_P < 0.1$ GeV).

2.3.4 Other Systematic Errors

Other than the systematic errors caused by the choice of different cut values, the systematic errors of the photon beam polarization and target polarization will also introduce uncertainty in the E asymmetry. Table 2.7 gives the photon beam polarization and its error from the Moller measurement. An estimation of the systematic error for the HD target polarization is shown in table 2.8.

Period	Beam polarization	Error
Silver1	-81.7%	1.4%
Silver2a	-81.7%	1.4%
Silver2b	-76.2%	1.4%
Gold2a	88.2%	1.4%
Gold2b	-83.4%	1.5%

Table 2.7: Photon beam polarization and its error for circular polarized beam run periods.

Uncertainties in reference Thermal Equilibrium (TE) measurement:

PD noise	0.3%	white noise in PD NMR while in HDice Lab
Temperature	0.2%	drift, thermal gradients in HD from radiant heat load
H background	0.4%	H bkg with no target.
Stoichiometry	0.1%	deviation of H:D of 1:1, due to H2 and D2 impurities
Bkg subtraction	0.6%	Err in signal integral from imperfect separation of bkg
Incomplete relaxation	0.5%	T1 for TE measurement can be comparable to sweep time

Uncertainties in measurement of frozen-spin(FS) signal:

IBC noise	0.6%	residual effect of white noise in IBC NMR and PD
Hall-B noise jumps	0.5%	Variations in signal area after correction for signal jumps
Circuit non-linearity	4.0%	From the quadratic dependence of the circuit transducer gain
RF inhomogeneity	1.4%	Field inhomogeneity
RF depolarization	0.1%	Residual uncorrected decrement from repeated rf sweeps

Uncertainties in relating FS signal to TE measurement:

Circuit drift	1.8%	Variation from connecting FS signal to TE reference
Lock-in gain error	2.9%	SRS 844 manufacturer's gain error
Differential ramp-rate	1.0%	Actual ramp rate differs from nominal
TC transfer losses	2.0%	Variation in polarization loss during a TC transfer
Total systematic error	6.0%	For both H and D polarization

Table 2.8: Systematic errors for HD polarization measurement.

From the formula of calculating E asymmetry: $E = \frac{1}{P_\gamma P_t} \frac{N_{1/2} - N_{3/2}}{N_{1/2} + N_{3/2}}$, the relative errors for photon beam polarization (P_γ) and target polarization (P_t) will be propagated to the final result of E asymmetry, which 1.4% from photon beam polarization, and 6.30% from target polarization.

2.3.5 Total Systematic Errors

We have considered two kinds of systematic errors, one is caused by the choice of different cuts in the event selection, another is from the systematic errors in the measurement of the photon beam polarization and HD target polarization. The total error for each kind is combined using quadratic sum, a summary for the systematic errors is shown in Table 2.9.

Sources	Systematic error for E asymmetry
Vertex z cut (± 0.2 cm)	0.012
Confidence level cut (+0.05, -0.03)	0.009
Missing momentum cut (+0.1 GeV)	0.027
$\sigma_{sys}(cuts)$	0.031
Photon beam polarization	1.4%
Target polarization	6.0%
$\sigma_{sys}(polarization)$	6.2%

Table 2.9: Combine the systematic error. The main source of systematic error from using different cuts is from the missing momentum cut. The main source of systematic error from polarization measurement is from target polarization.

2.4 Conclusion

The first measurement of E asymmetry for the reaction of $\gamma + n \rightarrow p + \pi^-$ is reported. The E asymmetry is plotted vs. the polar angle of the final state π^- in the center of momentum frame. The c.m. energy ($w_{c.m.}$) ranging from 1500 MeV to 2300 MeV has been divided into 21 bins with the bin size of 40 MeV. The results have been compared with two the predictions from two partial wave analysis group: Bonn-Gatchina and SAID. The agreement between the experiment results and the predictions from partial wave analysis is good for $w_{c.m.} < 1820$ MeV. For $w_{c.m.} > 1820$ MeV, the experiment results are different from the two predictions, and also the two partial wave analysis methods give different predictions. The result of the E asymmetry from this experiment will help the two partial wave analysis to improve their models, and give more accurate predictions for the energy $w_{c.m.} > 1820$ MeV, this energy range is also the place where most of the missing resonances are.

Appendices

Appendix A

The effective mass of nucleon inside deuteron

The technique of reaction channel selection used in this study is the 1-C kinematic fitting. One of the most important parameters used in this procedure is the effective mass nucleon inside deuteron. Such as in the channel $\gamma(n) \rightarrow p\pi^-$, there are four constrain equations from the conservation of energy and momentum, and three unknown values for the target neutron's initial 3 momentum. A key component for the kinematic fitting to work is an accurate estimate of the effective mass for the quasi free neutron.

An straightforward solution for this problem is to use Gaussian fit to find the central of the missing mass plot for this reaction, as in Figure A.1. However, as shown in the figure, the central values for the peaks from two different run periods are different. This difference is caused by an offset of the photon beam energy.

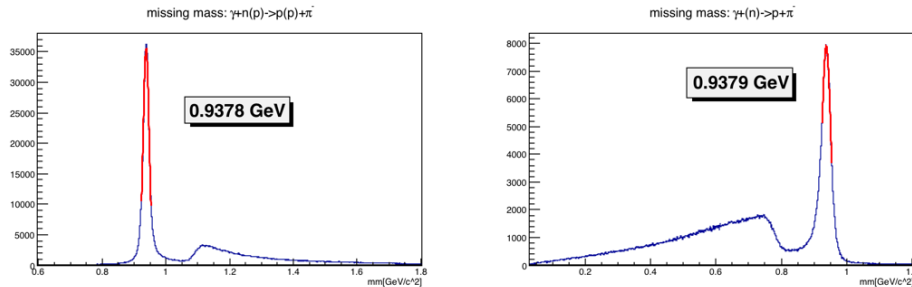


Figure A.1: Missing mass plot for the reaction of $\gamma(n) \rightarrow p\pi^-$, the left plot is for Silver1 period, the right plot is for Gold2a period.

In order to correct the photon beam energy, the missing mass is plotted for the same reaction, but in a different way. Using the spectator model, the same reaction can be written as $\gamma D \rightarrow p(p)\pi^-$, with p in parenthesis representing the spectator proton, which does not involved in the reaction. The spectator proton should have a on-shell mass of 0.9383 GeV. The missing mass plot for this reaction is shown in Figure ???. Both of the central values for the missing mass peaks are not at 0.9383 GeV. This indicate the photon beam energy is not very accurate. For Silver1 period, the photon beam energy should increase by 0.0030 GeV, and for Gold2a period, the photon beam energy should increase by 0.0082 GeV. The new missing mass plots for the reaction $\gamma D \rightarrow p(p)\pi^-$ after photon beam correction are shown in Figure ???.

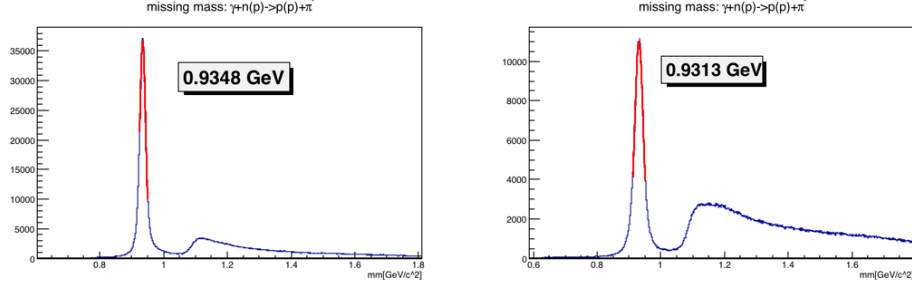


Figure A.2: Missing mass plot for the reaction of $\gamma D \rightarrow p(p)\pi^-$, the left plot is for Silver1 period, the right plot is for Gold2a period.

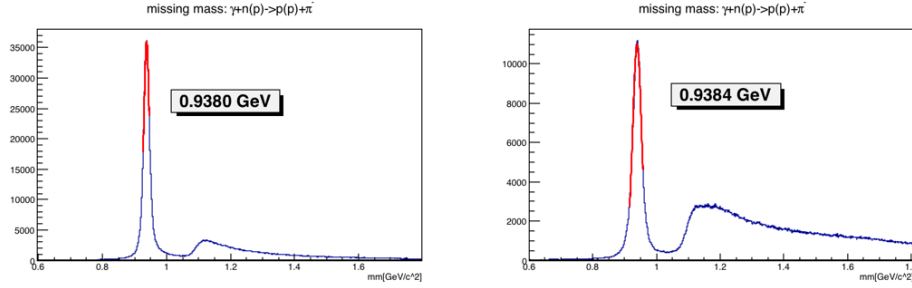


Figure A.3: Missing mass plot for the reaction of $\gamma D \rightarrow p(p)\pi^-$, the left plot is for Silver1 period, the right plot is for Gold2a period.

The missing mass plots for the reaction after the photon beam energy correction is:

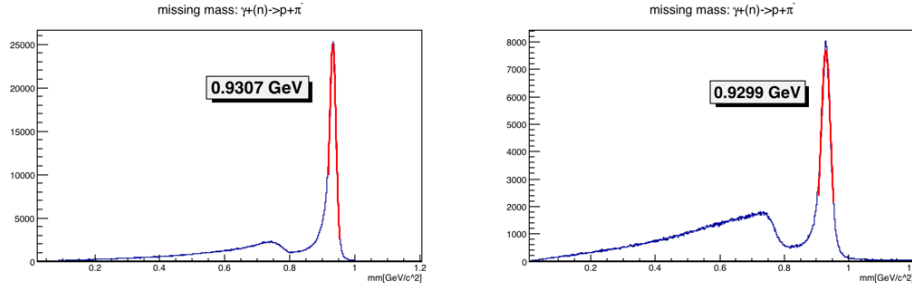


Figure A.4: Missing mass plot for the reaction of $\gamma(n) \rightarrow p\pi^-$, the left plot is for Silver1 period, the right plot is for Gold2a period.

The energy correction for photon beam and the calculated effective mass for quasi-free neutron for all circular run periods are shown in Table ???. The average and statistical error for the effective mass is: $m^* = 0.9303 \pm 0.0003$ GeV.

Period	ΔE (GeV)	m^* (neutron) (GeV)
Silver1	0.003	0.9307
Silver2a	0.0015	0.9305
Silver2b	0.0015	0.9303
Silver3	0.0015	0.9303
Silver4	0.0015	0.9300
Silver5	-0.0015	0.9305
Gold2a	0.0082	0.9299
Gold2b	0.0082	0.9302

Table A.1: The photon beam energy offset and the effective mass of quasi free neutron for all circular run periods.

Appendix B

Empty target subtraction

As shown in Figure 2.31 in Chapter 2, there are aluminum wires inside the HD target cell. The channel selection procedures, especially the Kinematic Fitting will remove most of the events from the target cell, but there are still some background events that will pass the cuts. During the experiment, an empty target run has been conducted for the study of empty target subtraction. Figure B.1 gives the z vertex distribution for gold2a period and emptya period, the blue line in the target region on right plot indicates a small amount of events from aluminum wires have passed the kinematic fitting cut.

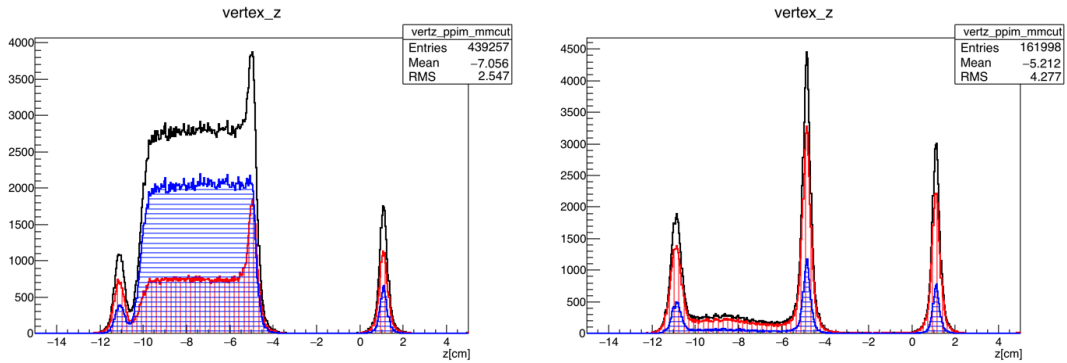


Figure B.1: Z vertex distribution for gold2a(left) and emptya(right). Black line is for all the events before the kinematic fitting cut, blue line is for events that pass the cut, and red line is for events fail the cut.

These background events will dilute the events from HD target, and makes the polarization observables smaller. And this effect can be corrected using the following equation:

$$E = \left(1 + \frac{N_{empty}}{N_{HD}}\right) E^{raw}, \quad (\text{B.1})$$

where N_{empty} is for the events normalized background events from empty target run, and N_{HD} is for the events from HD target.

A comparison of z vertex distribution between full target run and empty target run for different c.m. energy is shown in Figure B.2, it is noticed that the the ratios of events for the downstream Kelf peak are different for different c.m. energy. Thus, an energy dependent background correction for E asymmetry is needed.

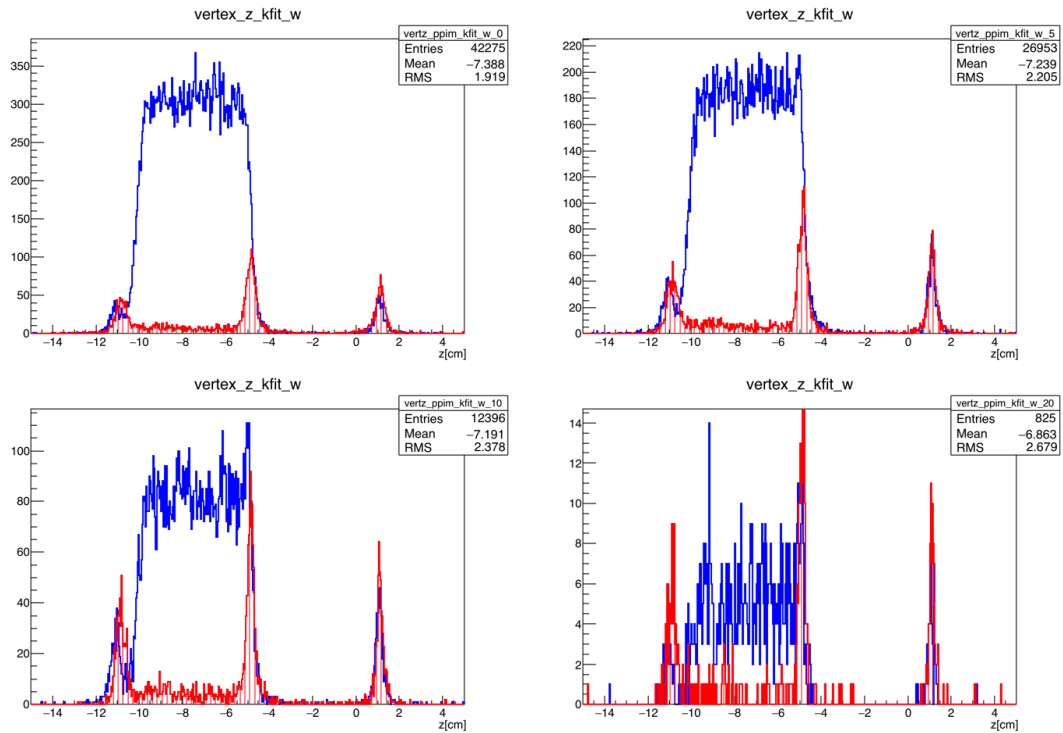


Figure B.2: Comparison of z vertex between Gold2a(blue line) and Empty-a(red line) periods for different c.m. energies.

Figure B.3 shows the ratios of events between the full target run periods and empty target run period for all circular runs.

The ratio of events between empty target runs and full target runs in the target region ($-10.5 \text{ cm} < z < -5.5 \text{ cm}$) can be obtained by using the scale constant from Figure B.3. For gold2a and gold2b periods, the fact that only 70% aluminum wires in use should be included in the calculation. The results are shown in Figure B.4.

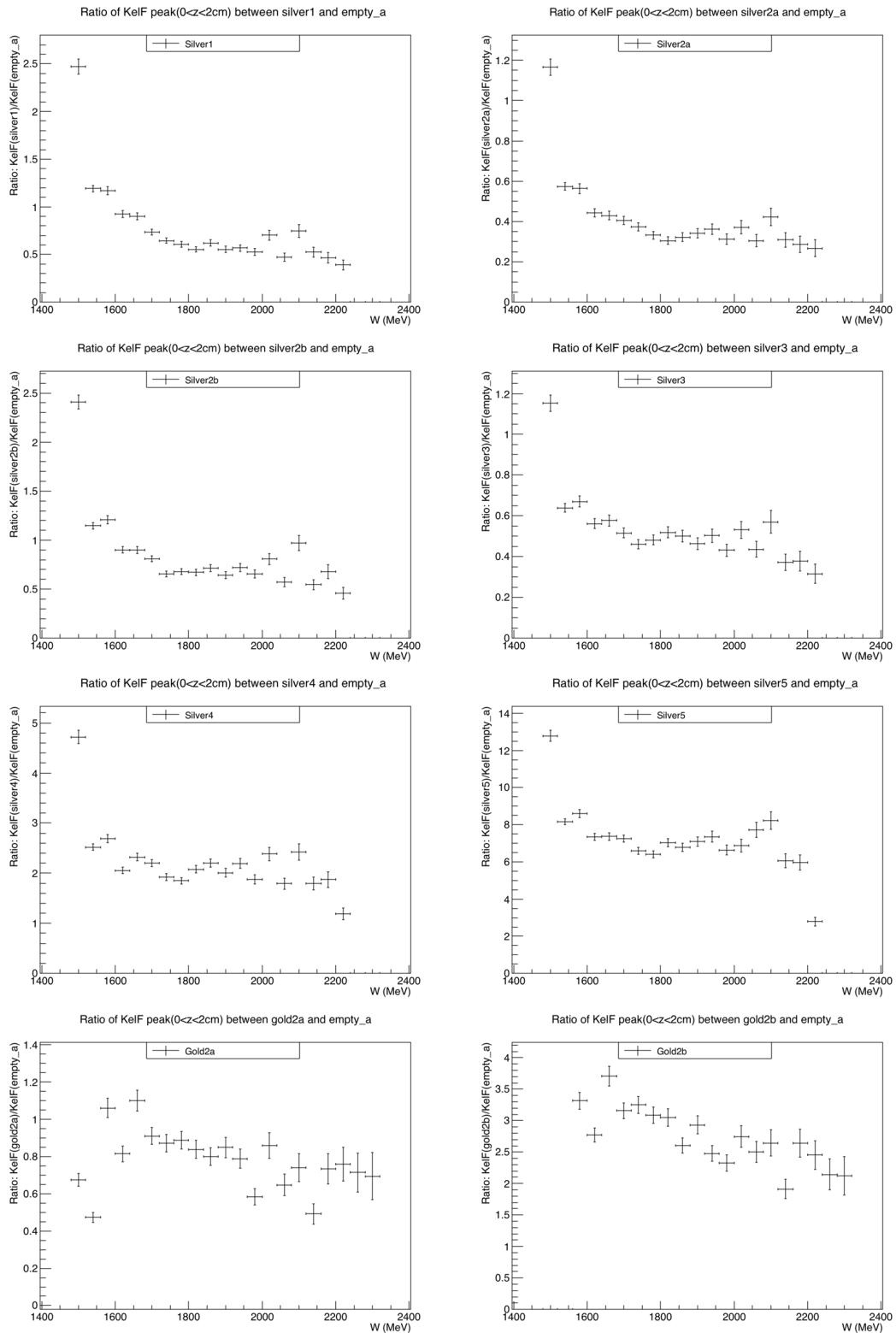


Figure B.3: Ratio vs. W (c.m.). Ratio = KelF(full target runs)/KelF(empty target runs)

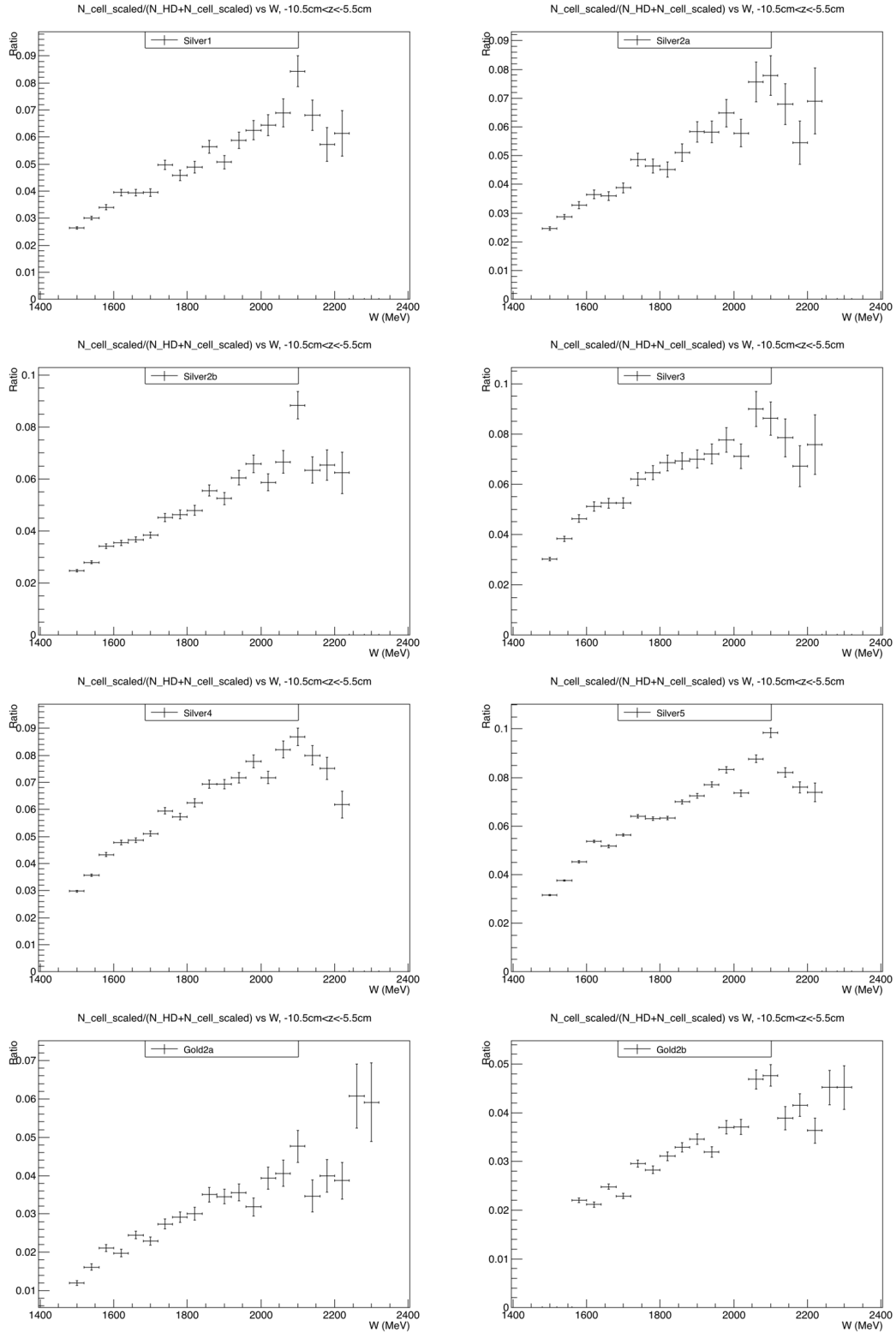


Figure B.4: Ratio vs. W (c.m.). Ratio = $N_cell_scaled/(N_HD+N_cell_scaled)$, where N -cell-scaled is the scaled number of events from empty target, N_HD is the number of events from HD.

Bibliography

- [1] K.A. Olive et al. (Particle Data Group), *Chin. Phys. C*, 38, 090001 (2014).
- [2] S. Capstick and W. Roberts, *Prog. Part. Nucl. Phys.* 45, 241 (2000).
- [3] C. Amsler, T. DeGrand, and B. Krusche, Review of quark model. *The Review of Particle Physics* (2014).
- [4] N. Isgur and G. Karl, *Phys. Lett.* 72B, 109 (1977); 74B 353 (1978); *Phys. Rev. D* 18, 4187 (1978); N. Isgur and G. Karl, *Phys. Rev. D* 19, 2653 (1979).
- [5] S. Capstick and N. Isgur, *Phys. Rev. D* 34,2809 (1986); S. Capstick and W. Roberts, *Phys. Rev. D* 47, 1994 (1993).
- [6] L. Ya. Glozman and D.O. Riska, *Phys. Rep.* C268, 263 (1996); L. Ya. Glozman, W. Plessas, K. Varga, R.F. Wagenbrunn, *Phys. Rev. D* 58, 094030 (1998)
- [7] U. Loring, K. Kretzschmar, B. Ch. Metsch, H. R. Petry, *Eur. Phys. J. A10*, 309 (2001); U. Loring, B.Ch. Metsch, H. R. Petry, *Eur. Phys. J. A10*, 395 (2001); U. Loring, B.Ch. Metsch, and H. R. Petry, *Eur. Phys. J. A10*, 447 (2001).
- [8] <https://www.flickr.com/photos/jeffersonlab>.
- [9] <https://www.jlab.org>.
- [10] B. A. Mecking et al. The CEBAF Large Acceptance Spectrometer (CLAS). *Nucl. Instrum. Meth. A* 503, 513 (2003).
- [11] M. Crofford et al. The RF System for the CEBAF Polarized Photoinjector. Technical Report, Thomas Jefferson National Accelerator Facility, 1993.
- [12] J. Grames et al. "Polarized Electron Sources @ JLAB" JLab Summer Science Series. July 7th, 2008.
- [13] Subashini De Silva, Superconducting Parallel-Bar Deflecting/Crabbing Cavity Development and its Applications. Technical Report, Old Dominion University, 2012.
- [14] D.I. Sober, et al. The bremsstrahlung tagged photon beam in Hall B at JLab. *Nucl. Instrum. Meth. A* 440, 263 (2000).
- [15] H. Olsen, L.C. Maximon. Photon and Electron Polarization in High-Energy Bremsstrahlung and Pair Production with Screening. *Phys. Rev.* 114, 887 (1959).

- [16] F.J. Klein, et al. The Coherent Bremsstrahlung Facility in Hall B at Jefferson Lab (2005).
- [17] F.A. Natter et al., Monte Carlo simulation and analytical calculation of coherent bremsstrahlung and its polarization. Nucl. Instr. and Meth. B 211 (2003) 465.
- [18] Y.G. Sharabian, et al. A new highly segmented start counter for the CLAS detector. Nucl. Instr. and Meth. A 556 (2006) 246.
- [19] E.S. Smith, et al. The time-of-flight system for CLAS. Nucl. Instr. and Meth. A 432 (1999) 265.
- [20] M. Amarian, et al. The CLAS forward electromagnetic calorimeter. Nucl. Instr. and Meth. A 460 (2001) 239.
- [21] Xiangdong Wei. HDice, the Polarized Solid HD Target in the Frozen Spin Mode for Experiments with CLAS. SPIN2012 (2012).
- [22] Isaac F. Silvera. The solid molecular hydrogens in the condensed phase: Fundamentals and static properties. Rev. of Mod. Phys. Vol. 52. 393 (1980).
- [23] Adalbert Farkas. Orthohydrogen, Parahydrogen and Heavy Hydrogen. (1935)
- [24] A. Honig and H. Mano. Enhanced nuclear polarization of D in solid HD. Phys. Rev. B 14 (5) 1858 (1976).
- [25] Christopher M. Bade. RF methods to increase deuteron polarization in HD targets and NMR spin-polarization analysis at LEGS. (2006)
- [26] C.D. Bass, et al. A portable cryostat for the cold transfer of polarized solid HD targets: HDice-I. Nucl. Instr. and Meth. A 737 (2014) 107.
- [27] Vivien Laine. Polarimetry of the polarized hydrogen deuteride HDice target under an electron beam.()
- [28] <http://clasweb.jlab.org/bos/browsebos.php>.
- [29] A.G. Frodesen, O. Skjeggstad, "Probability and Statistics in Particle Physics" (1979).
- [30] M. Williams, C.A. Meyer, "Kinematic Fitting in CLAS", CLAS-NOTE 2003-017 (2003).
- [31] Dustin Keller, "Techniques in Kinematic Fitting", CLAS-NOTE 2010-015 (2010).
- [32] E. Pasyuk, "The CLAS ELOSS package", CLAS-NOTE 2007-016, the package is available from CLAS CVS repository.
- [33] M. Williams, D. Applegate, C.A. Meyer, CLAS-NOTE 2004-017(2004).
- [34] Igor Strakovsky. Radiative Decay Width of Neutral non-Strange Baryons from PWA. DMHPFP, Messiah Italy, Sep. 2014.

- [35] K.M. Watson, Phys. rev. 85 (1952) 852
- [36] B. Krusche and S. Schadmand. Study of Non-Strange Baryon resonances with Meson Photoproduction. Progress in Particle and Nuclear Physics 51 (2003) 399-485.
- [37] M. Jacob and G.C. Wick. Ann. Phys. (N. Y.) 7, 404 (1959).
- [38] A. M. Sandorfi, S Hoblit, H Kamano, T-S H Lee. Determining pseudoscalar meson photoproduction amplitudes from complete experiments. J. Phys. G: Nucl Part. Phys. 38 (2011) 053001.
- [39] <http://pwa.hiskp.uni-bonn.de>
- [40] <http://gwdac.phys.gwu.edu>
- [41] S.Strauch, B.I Berman and the CLAS collaboration. Beam-Helicity Asymmetries in Double-Charged-Pion Photoproduction on the Proton. Phys. Rev. Lett 95 162003 (2005)
- [42] Sungkyun Park. Measurement of polarization observables in $\gamma p \rightarrow p\pi^+\pi^-$ using circular beam and longitudinal target polarization and the CLAS spectrometer at Jefferson Laboratory. PhD thesis (2013).
- [43] A. Fix and H. Arenhovel. Double pion photoproduction on nucleon and deuteron. Eur. Phys. J. A 25, 115 (2005)
- [44] W. Roberts and T. Oed. Polarization observables for two-pion production off the nucleon. Phys. Rev. C 71, 055201 (2005)